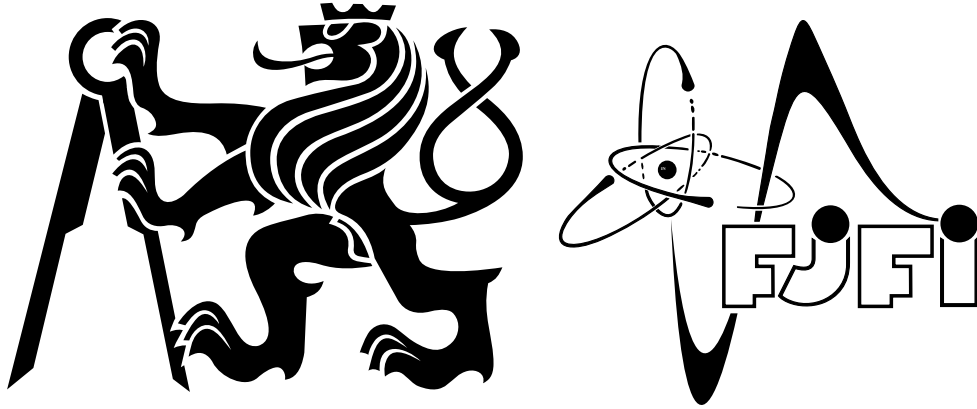


CZECH TECHNICAL UNIVERSITY IN PRAGUE
Faculty of Nuclear Sciences and Physical Engineering

Department of Physics
Branch: Physical Engineering
Specialization: Physics and Technology of Nuclear Fusion



**Diagnostic Systems for
Laser-Accelerated Ion Beams**

Master's thesis

Author: **Jan Prokúpek**
Supervisor: **Dr. Daniele Margarone, Ph.D.**
Year: **2012**

Prohlášení

Prohlašuji, že jsem svou diplomovou práci vypracoval samostatně a použil jsem pouze podklady (literaturu, projekty, SW atd.) uvedené v příloženém seznamu.

Nemám závažný důvod proti užití tohoto školního díla ve smyslu §60 Zákona č. 121/2000 Sb., o právu autorském, o právech souvisejících s právem autorským a o změně některých zákonů (autorský zákon).

V Praze, dne 6.1.2012

Jan Prokůpek

Acknowledgements

I owe my deepest gratitude to my parents for their physical and material support. Without them and their excellent support I would not be able to successfully go through many difficult years at school and to approach the participation in experiments and writing this thesis.

It is an honour for me to express my thanks to Dr. Daniele Margarone for his support, patience, encouragement, supervision and useful suggestions throughout this work. His moral support and guidance enabled me to join the particle acceleration team in the Institute of Physics and to complete my work successfully. I am indebted to all members of our team for supporting me, specially to Miroslav Krůs for his valuable help during the experiments and his suggestions during processing the experimental data and writing the thesis.

I would like to thank P. Paris and his team from the Institute of Plasma Physics and Laser Microfusion for their cooperation in development of the new ion collector system.

I would like to thank also Prof. Jiří Tolar for his consultation about the Telegrapher equations which inspired me to build a physical model of the developed Faraday cup. According to this I am grateful to Michal Stránský from the ELI team in the Institute of Physics for his help with issues of physics behind the model.

I would like to show my gratitude to my schoolmate Milan Frank for his help to deal with everything concerning lasers. I would like to express my thanks also to my schoolmate Michal Špaček for checking my steps in theoretical parts of the thesis.

I am grateful to all people enabling me to take part in experiments at PALS in Czech Republic, at APRI-GIST in Korean Republic and at GSI in Germany. I would like to express my deepest thanks to personnel present in these facilities.

Title: **Diagnostic Systems for Laser-Accelerated Ion Beams**
Author: Jan Prokůpek
Branch: Physical Engineering
Work: Master's thesis
Supervisor: Dr. Daniele Margarone, Ph.D.
Department of Ultraintense Lasers, Institute of Physics AS CR, v. v. i.

Abstract:

This thesis work aims at using real-time diagnostic systems for a full characterization of ion beams accelerated by high intensity laser-matter interactions. Various time-of-flight detectors and ion spectrometers has been mainly used at the domestic 25 TW, fs-laser system, and at the kJ-class, ps-laser system at the PALS Centre. Moreover, joint experiments performed in other international laboratories operating at higher laser intensities, such as the APRI-GIST and the PHELIX-GSI laboratories, are reported. The standard ion acceleration mechanism into forward direction, so-called TNSA (target normal sheath acceleration), has been used in these experiments. The main challenge of this work was to develop a new plasma ion and electron detector capable to work relatively close to the target (plasma source) and to record particle current signals in harsh conditions, where other real-time detectors fail. Data analyses and discussion of experimental results obtained from various types of diagnostics are reported in the work along with preliminary results obtained by the new developed detector.

Key words: laser, plasma, particle accelerators, particle diagnostics.

Název práce: **Diagnostický systém pro laserem urychlené iontové svazky**
Autor: Jan Prokůpek

Abstrakt:

Tato práce se zaměřuje na použití diagnostických systémů pracujících v reálném čase pro plnou charakterizaci iontových svazků urychlených pomocí vysokointenzivních interakcí laserového záření s látkou. Zejména se používalo několik spektrometrů a time-of-flight detektorů na místním 25 TW, fs laseru a na kJ, ps laseru v zařízení PALS. Jsou zde uvedené partnerské experimenty konané v mezinárodních laboratořích pracujících s ještě intenzivnějšími lasery, jako například laboratoře APRI-GIST a PHELIX-GSI. Ionty byly v experimentech urychlované směrem vpřed standardním mechanismem, tzv. TNSA (z angl. target normal sheath acceleration). Hlavním úkolem této práce byl vývoj nového detektoru elektronů a iontů proudících z plazmatu, jenž je schopný pracovat v relativně blízké vzdálenosti od terče (zdroje plazmatu) a zaznamenat proudový signál dopadajících částic v extrémních podmínkách, kde jiné detektory pracující v reálném čase selhávají. Analýza dat a diskuze experimentálních výsledků obdržných z různých diagnostik jsou uvedené v práci spolu s předběžnými výsledky z nově vyvíjeného detektoru.

Klíčová slova: laser, plazma, urychlovače částic, diagnostika částic

Contents

Contents	6
List of Figures	9
List of Tables	10
Introduction	11
1 Laser Driven Ion Acceleration Mechanism	12
1.1 Plasma parameters	13
1.2 Laser Absorption Mechanism	15
1.2.1 Inverse Bremsstrahlung	15
1.2.2 Resonance Absorption	16
1.2.3 Stimulated Raman Scattering	18
1.3 Laser Driven Ion Acceleration Mechanism	18
2 Laser Facilities	23
2.1 Iodine kJ Laser System at PALS	24
2.2 TW Class Ti:Sapphire Laser System at PALS	26
2.3 100 TW Ti:Sapphire Laser System at APRI-GIST in Korea	32
2.4 500 TW PHELIX Laser in GSI Darmstadt	34
3 Real-Time Diagnostics	37
3.1 Ion Energy Analyzer	38
3.2 Thomson Parabola Spectrometer	39
3.3 SiC Detector	42
3.4 Ion Collector	44
3.5 Design and Development of New Types of Faraday Cups	46
4 Results Obtained at Different Laser Facilities	51
4.1 Results from Iodine kJ Laser at PALS	51
4.2 Results from Ti:Sapphire fs Laser at PALS	53
4.3 Results from 100 TW Ti:Sapphire Laser at APRI-GIST in Korea	60
4.4 Results from PHELIX Laser in GSI Darmstadt	64
Conclusions and Perspectives	69
A Scheme of the Ti:Sapphire Laser System at PALS	70
B Derivation of Parabola Equation for Thomson Parabola Spectrometer	74

C Physical Model of Developed Faraday Cup	79
D Derivation of Energy Distribution Measured by Faraday Cup and SiC Diagnostics	87
Bibliography	91
Published Papers	95

List of Figures

1.1	1D sketch of the laser pulse interaction with plasma having a density gradient. Electrons are pushed out at the laser pulse front because of the ponderomotive force until the electrostatic potential of the charge separation equilibrate the ponderomotive potential of the laser field [7, 10].	15
1.2	Scheme of Resonance absorption for (a) p-polarized and (b) s-polarized laser beam impacting the target [11].	17
1.3	Fraction of resonance absorption as a function of the scaled angular variable $(kL)^{2/3} \sin^2 \alpha$. The curve has been calculated for p-polarized light [11, 13].	17
1.4	Images of the electron circulation inside the target for (I) a thick ($L > L_p/2$) target and (II) a thin ($L < L_p/2$) target [7].	20
2.1	The kJ iodine laser system and its components installed at PALS [21].	25
2.2	Schematic energy level diagram of Ti:Sapphire [23]	27
2.3	The complex scheme of the Titanium Sapphire laser system consisting of the Oscillator, Regenerative Amplifier, Multipass Power Amplifier and Compressor. The more detailed Figures are in Appendix A.	27
2.4	Experimental scheme with the laser beam coming from the top reflected by two flat mirrors (FM) onto the off-axis parabolic mirror (OAP) covered by a pellicle foil (PEL) and focused first into the focal point of the microscopic objective with camera (CAM) and after the laser focus optimization the beam was focused on the target creating plasma and fast particles detectable by an ion collector (IC), a ring ion collector (RIC) and a silicon-carbide detector (SiC). The diagnostic devices will be further described in Chapter 3.	29
2.5	Dependence of the beam spot size at FWHM and $1/e^2$ vs. the focus position.	30
2.6	Sharp focus of the laser beam at the best (zero) focal position corresponding to the plot in Figure 2.5.	31
2.7	Schematic diagram of 10 Hz, 100 TW CPA Ti:Sapphire laser system [26].	32
2.8	Sharp focus of the laser beam at the best (zero) focal position.	33
2.9	Schematic overview of the PHELIX laser system [29].	34
2.10	The beam profile in the sharp focal position inside the target chamber during our measurement.	36
3.1	Scheme of the IEA. Plasma is produced at the target T heading to the deflection system of the IEA and further to the detector WEM (windowless electron multiplier). The input and output slits b_{in} and b_{out} collimate the ion beam entering and leaving the IEA [30].	38
3.2	Typical IEA spectrum.	39

3.3	Schematic draw of the Thomson parabola analyzer. Particles propagate through the parallel \mathbf{B} and \mathbf{E} field initiated by permanent dipole magnet (or electromagnet) and capacitor plates. Ions are separated due to their charge states and mass in a presence of fields and then impact the imaging plane drawing the parabola lines.	40
3.4	Configuration of the TP imaging plane using the MCP to intensify the incoming ion signal, phosphor screen to convert the electron signal into the visible light registered by CCD camera.	42
3.5	SiC pad detectors. Each detector has a surrounding Schottky contact ring whose function is to act as a guard draining the leakage current coming from the chip surface and borders. The black dots on the central and guard electrodes are reinforced areas for wire bondings [35].	43
3.6	Ion collector design with two Faraday cups inside a copper Faraday cage with the hole for laser alignment.	47
3.7	The cross section of the Faraday cup consisting of the inner copper electrode where the charge is collected, a Teflon insulator between the inner and the outer electrode recessed inside the marital support with the collimator embedded at the entrance of the Faraday cage.	48
3.8	The scheme of the electronic circuit of the Faraday cup array.	49
4.1	Results obtained by the IC diagnostics with several filters cutting off a part of X-rays and enabling the detection of the fastest ions.	52
4.2	Current density signal from the ion collector for different aluminium target thicknesses.	52
4.3	The typical TOF spectra obtained from the diagnostics IC, RIC and SiC employed simultaneously during one single laser shot of 325 mJ. The time scale has been recalculated for 1 m detection distance for each device.	54
4.4	Comparison of two different ion collectors (IC and RIC) employed during a laser shot at 520 mJ.	55
4.5	Energy spectrum of the collected charge by IC and RIC recalculated by equation (4.3) corresponding to the measurement from Figure 4.4.	55
4.6	TOF spectra obtained with 423 mJ laser energy on target and measured by the SiC detector. The proton signal was fitted by the Boltzmann-like distribution reported in equation (4.4).	57
4.7	Energy spectrum of the particles impinging on the SiC detector recalculated by equation (4.6) corresponding to the TOF signal plotted in Figure 4.6.	58
4.8	Measured TOF spectrum obtained with 650 mJ laser energy on target and measured by the SiC detector.	59
4.9	Energy spectrum of the particles impinging the SiC detector recalculated by equation (4.6) corresponding to the TOF signal plotted in Figure 4.8.	59
4.10	TOF and TP diagnostics employed for simultaneous measurement at APRI-GIST [31].	60
4.11	Measured TP spectra with depicted energies on the proton parabola.	61
4.12	Comparison between the simultaneous measured TOF signal and TP signal both recalculated in TOF configuration at 1 m detection distance.	62
4.13	Maximum measured proton energy and total proton energy for different target geometries (175 nm, 266 nm and 535 nm sphere diameters) in the same experimental conditions in the “bad contrast” regime.	63

4.14	Maximum measured proton energy and total proton energy for different target geometries (175 nm, 266 nm and 535 nm sphere diameters and pure foil without any structure) in the same experimental conditions in the “good contrast” regime.	64
4.15	Experimental setup: right top is the collector placed behind the lead shielding, right down is the array of eight Faraday cups looking at the target, on the left is the outside where the circuit is attached to chamber coated by several layers of aluminium foil shielding also the cables inside the bellows coming into the Faraday cage with oscilloscopes inside.	65
4.16	TOF spectrum measured by the developed Faraday cup.	65
4.17	TOF spectrum from measurement of the collector placed behind the lead bricks inside the chamber, only the cable connected to the chamber’s flange and the oscilloscope placed inside a Faraday cage out of the chamber, and their averaged signals.	66
4.18	Fourier transform of the measured signal from Figure 4.17.	67
A.1	Oscillator: DM - dichroic mirror; TiS - titanium sapphire laser crystal; DP - dispersive prism; HR - high reflective (100%) mirror; OC - output coupler; BS - beam splitter; PD - photo diode.	70
A.2	Regenerative amplifier of the Ti:Sapphire laser: Pol. - Polarizer; DG - dispersive grid; PM - parabolic mirror; FM - flat mirror; Per. - periscope; TiS - titanium sapphire laser crystal; PC# - pockels cell; QWP - quarter-wave plate; CM - cavity mirror; PD - Photo diode; LD - laser diode.	71
A.3	Multipass power amplifier: TiS - titanium sapphire laser crystal; LD - laser diode.	71
A.4	Compressor: DG - dispersive grid; Per. - periscope.	72
A.5	Temporal profile of the laser beam pulse and comparison with the theoretical limit behind a small compressor measured by the SPIDER diagnostics.	72
A.6	Wavelength spectrum with a central wavelength at 808 nm and spectral width of 20 nm at FWHM.	73
A.7	Beam wavefront profile after the compressor.	73
B.1	Deviation of the charged particle in presence of the magnetic field and its further detection on imaging plane.	75
B.2	Deviation of the charged particle by the electric field and its consequent detection on an imaging plane.	77
C.1	Voltage and current definitions and lumped-element for an incremental length of transmission line [44, 45].	79
C.2	Field lines on an arbitrary TEM transmission line [45].	82
C.3	Cross-section of a coaxial line and system of two-wires coming from the Faraday cup into a coaxial BNC cable.	82
D.1	Scheme of grid in front of the ion collector.	87

List of Tables

2.1	The output parameters from the kJ-class laser at PALS [22].	26
2.2	Ti:Sapphire laser specifications.	31
2.3	Properties of the 100 TW beamline at the Ultrashort Quantum Beam Facility at APRI.	33
2.4	Beam parameters of the PHELIX laser system [29].	35
C.1	Table of the weighted transmission.	84
C.2	Table of physical constants, Faraday cup and Two-wire properties and their numerical expressions (dependent on the signal frequency valid from 10 MHz up to the cutoff frequency except the interval $< 9.5 \text{ GHz}, 10.2 \text{ GHz} >$ where a non-negligible behavior of Teflon's relative permittivity and permeability is present, and in which these values are not constant [41]) for the Telegrapher equations [45]. The group velocity formula is very complicated to be presented here, it was processed and calculated by mathematical software and its general expression covers full 23 pages of A4 format.	86

Introduction

High energy charged particles, such as protons and ions, can be accelerated by means of high intensity laser beams interacting with a solid target creating plasmatic state of matter. The interaction of a strong laser pulse with a target can generate plasma waves capable to accelerate electrons to high energies via non-linear forces. Fast electrons are generated as first due to their lowest mass. Their fast displacement from the laser-target interaction point creates a spatial charge separation leading to a high intensity electric field causing the acceleration of protons and heavier ions. Recent progress in laser technology enables production of laser pulses with intensities high enough to accelerate protons/ions to energies of several MeV from thin solid targets.

Chapter 1 describes the absorption mechanism relevant for the particle acceleration by ultra-intense lasers. The specific acceleration mechanism investigated in this thesis work is called Target Normal Sheet Acceleration (TNSA) where the fast ions are generated at the rear side of a thin solid target and accelerated in the direction of laser beam propagation, mainly along the target normal.

The facilities over which the experiments for this thesis were done are reported in Chapter 2. These facilities are described here in detail in order to get some knowledge of basic principles of generation of intense laser pulses. The facilities described here are domestic ones, such as the kJ and fs laser systems at PALS, and foreign ones which in their best conditions exceed intensities greater than 10^{20} W/cm². These facilities are the 100 TW fs laser system at APRI-GIST in Korean Republic and the PHELIX laser system at GSI Darmstadt, which is today one of the most intensive laser in the world.

Products of the interaction of intense laser beams with solid targets have to be detected in order to optimize the particle beam characteristics. Thus, the design, development and optimization of diagnostic systems to be tested and used during different experimental campaigns in various laser facilities are crucial issues. One of the possible diagnostic techniques is the time-of-flight (TOF) one where various detectors can be employed, which can offer some advantages with respect to standard position sensitive ion energy spectrometers. The special aim of this thesis work is the development of a TOF detector capable to work as a real-time diagnostic in extreme conditions, this study is reported in Section 3.5 and its physical model is described in Appendix C.

The results from various experiments of laser-driven ion acceleration are reported in Chapter 4. The experiments have been performed at the laser facilities described in Chapter 2 with the diagnostic system described in Chapter 3. Various types of targets, as well as different laser pulse durations and wavelengths, have been used during the different experimental campaigns. All the results shown here have been obtained in the TNSA acceleration scheme described in Chapter 1 where proton and/or ion beams are generated from thin solid targets and accelerated up to multi-MeV energies.

The results from the developed TOF detector are reported in Section 4.4. The mathematical approach for the data treatment from Thomson parabola spectrometer is performed in the Appendix B, and from TOF diagnostics in Appendix D.

Chapter 1

Laser Driven Ion Acceleration Mechanism

The first idea of using laser-plasma interactions to accelerate particles dates back to 1979, when Tajima and Dawson published a paper about the laser electron acceleration [1]. They proposed a simple mechanism in which the laser beam is injected into the underdense plasma and excites an electrostatic wake behind the laser beam. Electrons can be trapped in this wake and then accelerated to high energies, as confirmed by numerical simulations. The specific processes occurring during the laser-plasma interactions have been better understood later on by means of advanced numerical simulations aimed to identify crucial parameters such as the plasma density, laser intensity, laser pulse width, etc.

In order to achieve better particle acceleration performances (i.e. accelerating them to high kinetic energies) the laser intensity has to be increased. It is more costly to achieve very high laser intensities when a long laser pulse is used (a high laser energy must be delivered), thus shorter laser pulse systems (picoseconds or subpicosecond regime) needed to be developed. A new laser technologies based on the chirped pulse amplification (CPA) was discovered and developed [2, 3], where ultra-short, ultra-high intensity pulses with typical duration from few tens to hundreds femtoseconds can be obtained. Furthermore, when a short pulse is used a high intensity gradient is produced, which means stronger accelerating forces.

This chapter is supposed to give a brief theoretical introduction into this innovative field of a laser-matter interaction, since experimental studies on high-intensity laser driven acceleration from solid targets, typically several micrometers thick, are reported in this thesis. In a simplified picture the incoming laser beam is focused onto the target front surface, then it is mainly absorbed by the available electron population and creates a plasmatic state of matter and setup a “quasi-electrostatic” field which accelerates the plasma ions at very high energies. A general overview of the plasma parameters useful for understanding the acceleration mechanisms is shown in Section 1.1. The laser beam interacting with the solid target and consecutively creating a plasma is absorbed via several possible mechanisms described in Section 1.2. The absorption of the laser energy can lead to the generation of fast particles, especially electrons, which are spewed out from plasma creating electrostatic fields over which the positively charged particles (ions) can gain energies up to few MeV or tens of MeV. Since in the most of cases the ions are produced at the target rear side and accelerated into the forward direction (the direction of the laser beam propagation), the specific acceleration mechanism is described in Section 1.3.

Other acceleration mechanisms at ultra-high laser intensities also exist. One of the most studied mechanism to be investigated with ultra-intense laser systems is the Radiation Pressure Acceleration (RPA) [4]. However, the laser intensities necessary for such

mechanism do not refer to the ones used in this thesis.

1.1 Plasma parameters

Plasma is a quasi-neutral system mainly made of charged particles which respond to electromagnetic fields with a collective behavior. Quasi-neutrality means an approximated equilibrium between the positively charged ions and negatively charged electrons in plasma over a distance much larger than a specific size called Debye length. The presence of charged particles in the plasma creates electric space charge and, as a consequence electrostatic fields, which influence the other charged particles. This results in a compensation of the fluctuation in charge density and plasma appears as electrically neutral on large scales.

A basic characteristic of the plasma behavior is the capability to shield external electric fields applied in the plasma. For instance, when a charged particle is placed in the plasma, it starts to attract the surrounding particles with the opposite charge and to repulse particles with the same charge. Finally, the inserted particle will be surrounded by particles with opposite total charge and the electrostatic potential will be shielded. In case of an ideally cold plasma the shielding effect would be perfect and no potential would be observed at scales larger than the Debye length. In real plasmas, with a finite temperature, an edge of the cloud surrounding the inserted particle exists. In such region the electric field is weak and the particles on the edge have a sufficient thermal energy to escape from the electrostatic potential well. Hence the edge of the cloud is the radius on which the potential energy is in equilibrium with the thermal energy $k_B T_e$ and the shielding effect is not perfect (where k_B is the Boltzmann constant and T_e is the electron plasma temperature). $k_B T_e / e^1$ sized potential can penetrate into the plasma and causes a finite electric field. In the simplified plasma model where the shielding effect is carried out by plasma electrons the Debye length is then:

$$\lambda_D = \sqrt{\frac{\epsilon_0 k_B T_e}{n_e e^2}} \quad (1.1)$$

where ϵ_0 is vacuum permittivity, n_e is electron density and e is elementary charge. When plasma electrons are displaced from the positively charged ions by means of external fields, the electrostatic forces between electrons and ions causes the oscillation of electrons around the position of the charge equilibrium with a characteristic frequency, called electron plasma frequency ω_p . If the electric field of the external source is so strong that the electron quivering motion approaches the speed of light c during the oscillations, the electron mass m_e will increase by a relativistic factor:

$$\gamma = \sqrt{1 - \frac{v^2}{c^2}} \quad (1.2)$$

where v is particle's velocity. During the electron oscillation cycle its mass is changing resulting in an unharmonious motion. The electron plasma frequency is then:

$$\omega_p = \sqrt{\frac{n_e e^2}{\epsilon_0 \langle \gamma \rangle m_e}} \quad (1.3)$$

where $\langle \gamma \rangle$ is averaged over the oscillation of the applied field (usually such fields are created by electromagnetic waves, especially lasers) and also over a large number of electrons.

¹e in denominator denotes Euler's number.

When the frequency of the external field exceeds a lot the electron plasma frequency, the electrons are not able to follow the field oscillations and the external electromagnetic wave can propagate inside the plasma. On the other hand when the external field frequency propagates into a plasma density gradient, it can be stopped at the so called plasma critical density n_c where the electron plasma frequency is equal to the field frequency ω_L . The critical density is analytically defined as:

$$\omega_p = \frac{\langle \gamma \rangle \epsilon_0 m_e \omega_L^2}{e^2} \quad (1.4)$$

By using high intensity lasers which cause relativistic electrons oscillations, the averaged electron mass increases locally during the oscillation in the laser field. Such a condition leads to a reduction of the refractive index along the laser axis compared to the edges of the beam envelope. When this effect actuates the ionization defocusing, the plasma starts to act as a positive lens leading to the consequent increasing of the intensity. This is not accessible in vacuum only because there is no medium having any refractive properties. This effect is known as a relativistic self-focusing. A further mechanism occurs, when electrons are stroked by the laser ponderomotive force out of the high intensity region resulting in a decrease of the local electron density and consequently in a better focusing of the laser beam. This is known as a ponderomotive self-focusing. The power threshold P_c above which the relativistic self-focusing is present is given by [5]:

$$P_c [\text{W}] = 1.78 \times 10^{10} \left(\frac{\omega_L}{\omega_p} \right)^2 \quad (1.5)$$

Using the relativistic formalism the electric field intensity \mathbf{E} can be expressed as:

$$\mathbf{E} = -\nabla\phi - \frac{\partial\mathbf{A}}{\partial t} \quad (1.6)$$

where $\phi = \phi(t, \mathbf{x})$ is an electric potential and $\mathbf{A} = \mathbf{A}(t, \mathbf{x})$ is a magnetic potential vector. The magnetic induction \mathbf{B} is then given by:

$$\mathbf{B} = \nabla \times \mathbf{A} \quad (1.7)$$

Solving the equation of motion for moving particles in the laser fields:

$$\frac{d\mathbf{P}}{dt} = -\frac{\partial H}{\partial \mathbf{x}}, \quad \frac{d\mathbf{x}}{dt} = -\frac{\partial H}{\partial \mathbf{P}} \quad (1.8)$$

where H is Hamilton function for relativistic motion of particle [6]:

$$H = c\sqrt{m_0^2 c^2 + (\mathbf{P} - Q\mathbf{A})^2} + Q\phi \quad (1.9)$$

and \mathbf{P} is the particle's canonical momentum:

$$\mathbf{P} = \gamma m_0 \mathbf{v} + Q\mathbf{A} \quad (1.10)$$

where m_0 is the rest mass of particle and Q is its charge. Solving equation (1.8) by using (1.9) we can derive Lorentz force, and further assuming the charged particle is an electron, calculations shows that a ponderomotive potential $\phi_p = e\phi$ can be derived as [7]:

$$\phi_p = m_e c^2 (\gamma - 1) \quad (1.11)$$

where the relativistic factor of oscillating electrons is expressed in equation (1.1.200) and can be also written as [7]:

$$\gamma = \sqrt{1 + \langle a_0^2 \rangle} \quad (1.12)$$

where a_0 is a laser strength parameter [8, 9]:

$$a_0 = \frac{eE}{m_e c \omega_L} = \sqrt{\frac{I [\text{W}/\text{cm}^2] \lambda^2 [\mu\text{m}]}{1.37 \times 10^{18}}} \quad (1.13)$$

which tells us that the electron motion in a laser field with an intensity I and wavelength λ has a relativistic motion for $a_0 \gg 1$.

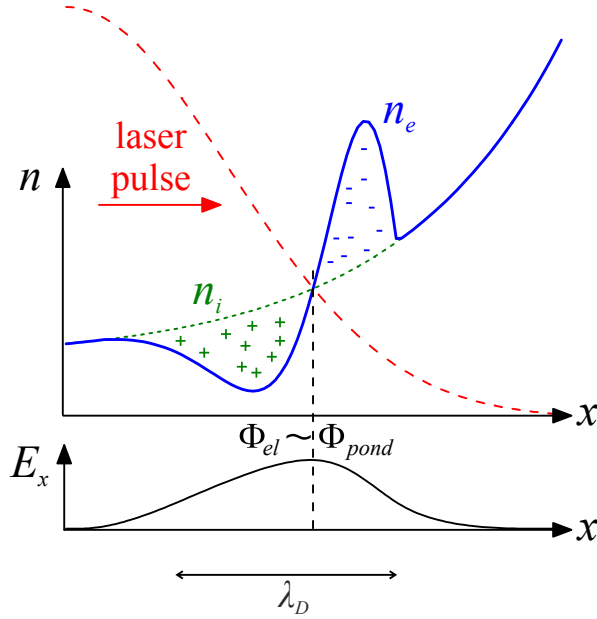


Figure 1.1: 1D sketch of the laser pulse interaction with plasma having a density gradient. Electrons are pushed out at the laser pulse front because of the ponderomotive force until the electrostatic potential of the charge separation equilibrate the ponderomotive potential of the laser field [7, 10].

1.2 Laser Absorption Mechanism

When a high intensity laser is focused onto a solid target a fast energy exchange from the laser to the target material occurs through a rapid increase of the target temperature. This kind of interaction takes place in a non-degenerate ideal plasma and the beam energy is transferred predominantly to free electrons or electron plasma waves. Finally a target thermalization occurs by Coulomb collisions between electrons and ions.

1.2.1 Inverse Bremsstrahlung

The term bremsstrahlung usually refers to the processes where electrons, or generally all charged particles, emit radiation due to their acceleration (or deceleration). The bremsstrahlung radiation is characterized by a continuous spectrum which becomes more intense and is shifted toward higher frequencies when the energy of the accelerated particle increases. The bremsstrahlung mechanism also includes the synchrotron radiation

emission occurring when the charged particles are deviated from their trajectory. The bremsstrahlung mechanism is frequently used in the limited definition of radiation coming out from electrons stopping in matter due to their acceleration in a presence of the static field of the material's nuclei. When the target thermalization leads to plasma creation, the free electrons constantly produce bremsstrahlung in collisions with the ions. If the plasma is optically thin, the bremsstrahlung radiation leaves the plasma carrying part of the internal plasma energy (this effect is known as the bremsstrahlung cooling).

The inverse bremsstrahlung is the reversed process in which an electron absorbs a photon while colliding with ion or another electron. This absorption gives an additional energy to the electron which is consequently spread by collisions to other particles present in plasma. When using lasers with a narrow spectral width the electron cannot absorb continues spectrum of radiation but only the one carried by laser photons.

The model for inverse bremsstrahlung mechanism predicts the total fraction of the collisional absorption of the laser light on its way toward the critical surface and the way back after reflection achieving the absorption coefficient [11]:

$$A_L = \frac{I_{in} - I_{out}}{I_{in}} = 1 - \exp\left(-\frac{8}{3} \frac{\nu_{ec}}{c} L\right) \quad (1.14)$$

where L is the length of a slab of plasma, ν_{ec} is the collision frequency of electrons which depends on the critical density n_c , charge state z_i and temperature of plasma electrons T_e as:

$$\nu_{ec} = \frac{4\sqrt{2\pi}}{3} \frac{n_c z_i e^4 \ln \Lambda_e}{k_B T_e \sqrt{m_e k_B T_e}} \quad (1.15)$$

where $\ln \Lambda_e$ is the Coulomb logarithm.

1.2.2 Resonance Absorption

The laser light approaching to the plasma region might have an oblique incidence to a plasma layer with a given density gradient. The geometrical configuration is sketched in Figure 1.2. Generally the laser field can be written as an addition of the so called p-polarization and s-polarization. For p-polarization (Figure 1.2 (a)), the electric field vector lies in the Figure plane indicated by lines transverse to the beam propagation and the E_z component lies in the direction of the density gradient. It can therefore separate negative and positive charges. In the critical layer, where $\omega_L = \omega_p$, this charge separation leads to a resonant excitation of a Langmuir wave. It is seen as a resonance peak in the plot of $|E_z|^2$ down in Figure 1.2 (a). When propagating downhill, this wave acquires very high amplitudes [12]. Eventually it breaks and generates hot electrons. Plasma behavior is different for s-polarized electromagnetic waves. In this case the electric vector is parallel to the surface of the plane target and has no E_z component. The corresponding plot of $|E_x|^2$ is shown in Figure 1.2 (b). It shows no resonant behavior and no energy absorption due to wave excitation.

The resonance absorption can occur only when the light is incident obliquely under an angle α . Light rays are then refracted in the low-density part of the plasma. This is illustrated in Figure 1.2, where the density profile is modeled by a linear ramp with scale length L . The beam trajectory cannot penetrate up to the resonance layer at $z = 0$, but reaches the turning point at $z = -L \sin^2 \alpha$. Due to its wave nature, however, the electromagnetic field can tunnel through the residual distance in a form of exponentially decaying amplitude.

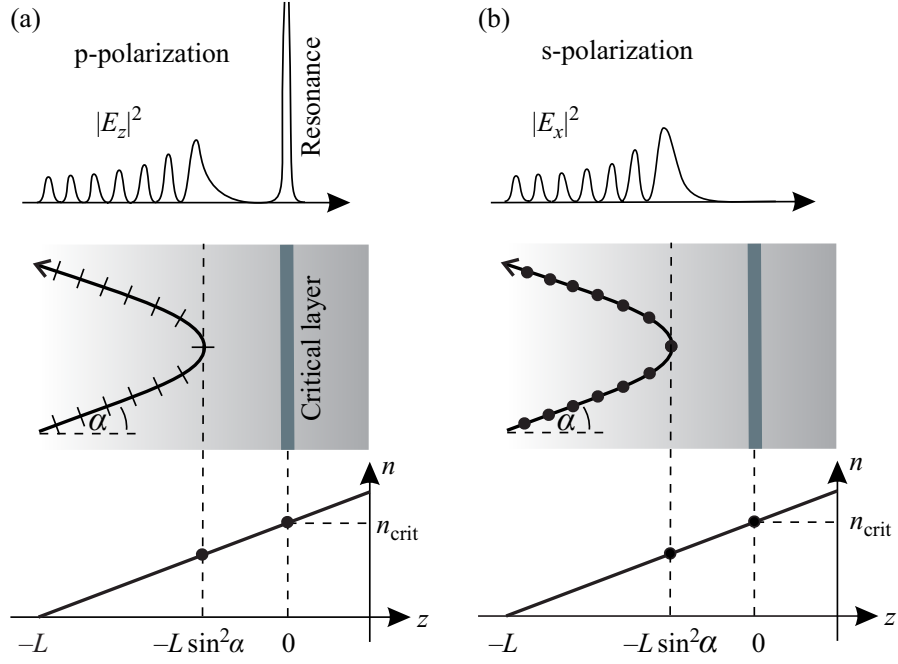


Figure 1.2: Scheme of Resonance absorption for (a) p-polarized and (b) s-polarized laser beam impacting the target [11].

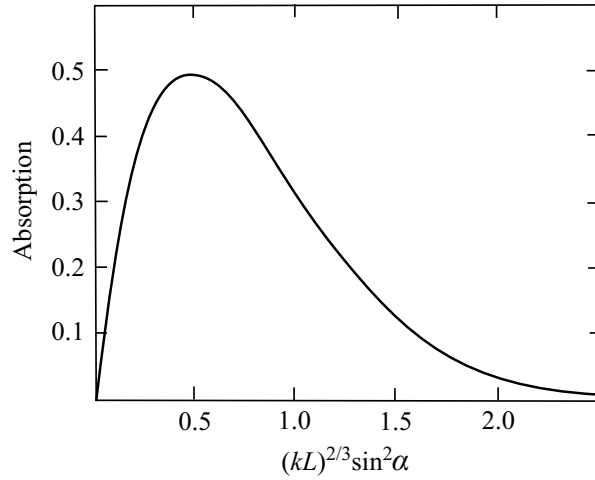


Figure 1.3: Fraction of resonance absorption as a function of the scaled angular variable $(kL)^{2/3} \sin^2 \alpha$. The curve has been calculated for p-polarized light [11, 13].

For a cold plasma it can be shown [11] that the absorption rate depends only on the single parameter $q = (kL)^{2/3} \sin^2 \alpha$, where k is the wavenumber of the laser beam. The numerical result is shown in Figure 1.3. The absorption curve can be readily understood in physical terms. For normal incidence ($q = 0$), the electric field of the light wave is parallel to the plasma surface and no coupling can occur. For very oblique incidence and/or large scale length ($q \gg 1$), on the other hand, the turning point stays far away

from the resonance layer, and tunneling is weak. Between these two limits a maximum absorption can be found (and is equal to 0.49 at $q = 0.5$ according to Figure 1.3). Resonance absorption can absorb as much as 50% of the light reaching the critical density, whereas the fraction of absorption does not depend on the intensity [11].

1.2.3 Stimulated Raman Scattering

Stimulated Raman Scattering is one of the so called parametric three-waves processes and it involves an inelastic scattering of the laser photon by an electron plasma wave which may occur in a subcritical plasma having density lower than $n_c/4$. It is not restricted to backscattering only but may also scatter the photon into forward and sideways directions.

The basic mechanism refers to an electron quivering in the incident laser wave and emitting scattered light in proportion to the local electron density n_e and therefore sensitive to density fluctuations δn_e . The scattered light beats with the incident light and couples back to δn_e through the ponderomotive force. A coherent feed-back occurs for δn_e modes corresponding to an electron plasma wave and satisfying the matching conditions:

$$\omega_L = \omega_1 + \omega_2, \mathbf{k}_L = \mathbf{k}_1 + \mathbf{k}_2 \quad (1.16)$$

where an initial laser frequency ω_L having a wave vector \mathbf{k}_L is split into the scattered light ω_1 , \mathbf{k}_1 and electron plasma wave ω_2 , \mathbf{k}_2 .

The conversion of laser energy into energy carried by electron plasma waves by means of the resonance absorption or the stimulated Raman scattering may lead to hot electron populations in the laser plasma corona having temperatures much higher than the bulk electron temperature. Hot electron populations are generated by plasma waves due to interaction with electrons moving with the wave at its phase velocity. The mechanism is related to that of Landau damping. The concomitant electrons may be trapped in the high-amplitude plasma waves excited by resonance absorption or stimulated Raman scattering and can be then accelerated to high energies, which is also one of the basic principles of laser-plasma based accelerator [11].

1.3 Laser Driven Ion Acceleration Mechanism

The mechanism of laser-driven acceleration of ions in forward direction is experimentally investigated in this thesis and for this reason the Target Normal Sheath Acceleration (TNSA) model is taken into account. When an ultra-intense laser is focused onto a solid target placed in vacuum, multi-MeV electrons are typically generated and then propagate through the target escaping from its rear side. Thus, a strong electrostatic potential is built up due to space charge separation in the vicinity of the target rear side at the boundary with vacuum.

When those hot electrons overcome this boundary, they are attracted back by the positive charge left inside the target (mainly protons generated from the ionization of surface hydrogen enriched contaminants) and forced to return into the target. Because of this mechanism an electron sheath is formed at the rear surface of the target. The associated electric field strength is strong enough to accelerate ions from the target rear side. The electric field is mainly parallel to the target normal and also the ion acceleration is aligned very well along this direction. For this reason it is called TNSA, first described by Wilks [14]. The highest energy of accelerated protons by TNSA (60 MeV) was observed in experiments using the short pulse of the NOVA laser at Lawrence Livermore National Laboratory by Snavely et al. [15].

The preferably accelerated charged particles are protons (highest energy gain) since they have the highest speed (lowest mass) among the other types of ions and, as a consequence, act as an electric field screening layer for the heavier particles. Finally the accelerated protons leave the target rear side and propagate forward together with the co-moving electrons forming a quasi-neutral plasma cloud. Since the electron plasma density in such cloud quickly drops down by leaving the target surface, and since the plasma temperature remains sufficiently high, recombination effects are negligible for propagation lengths in the range of several meters [10, 16].

In the experiments using long pulses (from picosecond to nanosecond scale) the plasma at the target rear surface slowly expands. The expansion of the positive ion distribution causes the electric field at the ion front to be reduced during the expansion. For this reason the acceleration becomes less effective already during the laser pulse duration. For the short-pulse experiments however, the life-time of the acceleration field is dominated by the laser pulse duration and not by the ion expansion itself. It means that the acceleration process is terminated when the laser pulse passes through and thermal effects are avoided.

However, usually at the target front side the high intensity part of the laser pulse interacts with a pre-plasma created by the ASE (amplified spontaneous emission) pre-pulse which is typical of the femtosecond laser systems. For this reason the TNSA mechanism is rarely due to a genuine laser-solid interaction and often occurs at the target front surface because the energetic electrons initially accelerated in the laser propagation direction are reflected at both target surfaces due to the space charge fields [7]. Electrons can travel through and circulate several times between surfaces. They lose their energy and quickly spread out on sideways heating up the target volume. According to a revised TNSA model the pre-pulse generates a blow-off plasma at the target front side with long scale lengths and therefore the electric fields here are much lower. The difference in potential is approximately equal for both target surfaces but the electric fields, which are proportional to the potential gradient, are inversely proportional to the Debye length in the plasma sheaths at both target surfaces. The potential difference and the electric fields are kept in the region where the electron temperature is high, thus particles accelerated by TNSA in a backward direction from the front side of the target gain much lower energies than particles in forward direction.

The commonly recognized effect responsible for the ion acceleration is charge separation due to high-energy electrons, driven by the laser on the target surface. There is a question related to the maximum ion energy \mathcal{E}_p . It has been mentioned that the maximum ion energy is proportional to the hot electron temperature T_h [7]:

$$\mathcal{E}_p = \alpha T_h \quad (1.17)$$

It was reported that the coefficient α depends on different experimental conditions. The electron recirculation can enhance the sheath acceleration. The basic idea is illustrated in Figure 1.4. The hot electron bunch length is approximately the same as the laser pulse length L_p , because the velocity of these hot electrons is approximately the same as the speed of light. The bunched electrons travel through the highly conductive target, like metal or plasma, without energy loss. They are then reflected at the target surface by a self-induced sheath field. When the target thickness L is greater than half of the pulse length, as seen in Figure 1.4, the electrons overlap only locally at the target edge and there is no significant increase of hot electron density. On the other hand, when the target is thinner, the electron recirculating process increases the effective electron density depending on the target thickness [7].

It was verified that the recirculation increases the number of hot electrons, but it does not increase the temperature. The peak proton energy from the rear side sheath

acceleration is much higher than this hot electron temperature. In order to find the scaling of the peak proton energy, a simplified model can be considered which treats a few protons motions in the sheath field. The sheath field is not perturbed because the total number of accelerated proton is very small. Also the hot electrons do not lose energy inside the target, they circulate continuously until they give their energy to the protons. First we want to know the base peak proton energy from the sheath acceleration. Since we know that recirculation enhances the peak proton energy when $L < L_p/2$, the pulse length is carefully chosen to be close to 2 times the target thickness to exclude the enhancement [7].

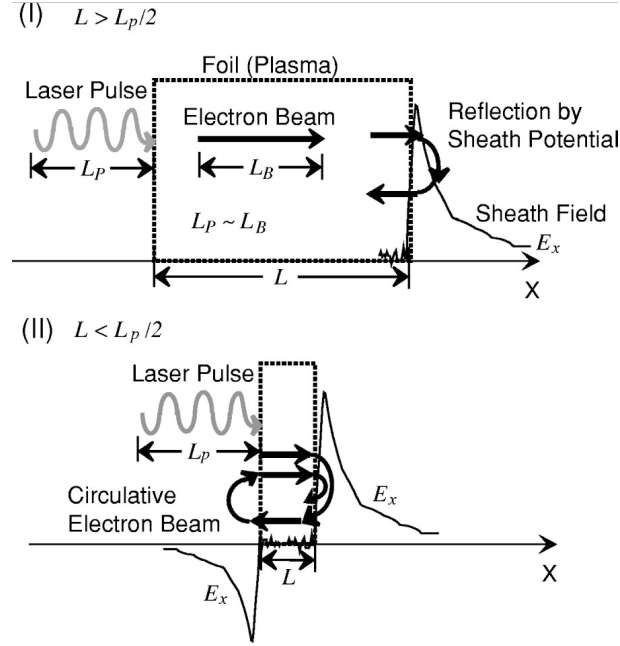


Figure 1.4: Images of the electron circulation inside the target for (I) a thick ($L > L_p/2$) target and (II) a thin ($L < L_p/2$) target [7].

The acceleration of a proton in the sheath field will continue until it passes through the turning point of the most energetic electron. At that point, the electrostatic potential equals the maximum energy of the electrons. After the proton has passed through this potential, it is expected to gain the same energy as the maximum electron energy $\mathcal{E}_{e_{MAX}}$.

The empirical scaling when the target thickness is smaller than the critical thickness $L_c = 2L_p$.

$$\mathcal{E}_{ion} = \left(\frac{L_c}{L}\right) \cdot \mathcal{E}_c \approx \left(\frac{L_c}{L}\right) \cdot \mathcal{E}_{e_{MAX}} \quad (1.18)$$

When the target thickness is larger than L_c , the circulation time is longer and the acceleration occurs intermittently. However, if the electron energy loss is small enough, the acceleration will continue until the same situation as in the case $L = L_c$, thus the final energy is close to \mathcal{E}_c . These situations are highly idealized because in reality the electrons are losing their energy through recirculation, especially at the edge of the target where the target ions are accelerated. The angular spread of the hot electrons reduces the recirculation effect. This scaling can be useful to estimate the proton energy as a function of pulse length and target thickness [7].

Only the fastest electrons can escape while the target is charging up. Most of the electrons are held back by the arising electric field and form a sheath at the rear side with a Debye length (equation (1.1)). This field ionizes atoms at the rear surface and accelerates them in the target normal direction. It was shown [17] that using an iterative procedure for solving the equation of motion and the continuity equation for protons, their new density profile in the next time step leads to a new potential and electric field. As the field is always peaked at the proton front, the fastest protons are also located there. An analytical expression describing the evolution of the maximum proton energy \mathcal{E}_p as a function of the interaction time t_i depending only on the electron temperature T_e and the initial electron density n_{e0} was also found [18]:²

$$\mathcal{E}_p \approx 2k_B T_e \cdot \left[\ln \left(\frac{\omega_p \tau_L}{\sqrt{2}e} + \sqrt{1 + \frac{\omega_p^2 \tau_L^2}{2e}} \right) \right] \quad (1.19)$$

To obtain the equation (1.19) it was assumed [17] that there is the same electron number and temperature on both target surfaces and the divergence of the electron beam propagating through the target is constant. The correct description of the rear side proton acceleration has to take into account the real evolution of the electric field including shielding effects by the expanding proton distribution itself. The proton energy spectrum predicted by the self-similar solution is [17]:

$$\frac{dN_p}{d\mathcal{E}_p} = \frac{n_{i0} c_s t}{\sqrt{2Z\mathcal{E}_p k_B T_e}} \cdot \exp \left(-\sqrt{\frac{2\mathcal{E}_p}{Zk_B T_e}} \right) \quad (1.20)$$

where c_s is the sound velocity and t is the time from which the plasma expands. This energy spectrum would extend to infinite proton energies in the pure self-similar model and it would only increase in number for longer interaction times. However, the protons show a sharp energy cutoff due to the formation of a proton front during the acceleration process. Therefore the energy spectrum only extends up to the peak energy of the protons situated at the front.

Several series of measurements have been performed varying the ASE pedestal duration τ_{ASE} , the laser intensity I_L , and the target thickness [18]. It was found that by increasing the target thickness from tens of nanometers up to hundreds of micrometers the energy first increases and then drops again. Thus it is evident that the highest proton energies are achieved at an optimal target thickness. Moreover it was shown that when the pre-pulse duration is changed, the other optimal values change correspondingly [18]. For thicker targets, the pre-pulse duration has no effect on the proton energies, whereas for thinner targets and longer τ_{ASE} the energies are reduced.

The significant changes in proton spectra and beam profiles described above can be interpreted as a transition between two regimes delimited by the optimal thickness. The first one where the front side acceleration is active for targets thinner than the optimal thickness and the second one where protons are accelerated from both target surfaces for target thickness above the optimal value. The rear side acceleration leads to higher energies in the second case. This mechanism is suppressed in the first case due to the formation of an ASE-induced density gradient at the rear side of the target.

The TNSA mechanism is responsible for proton acceleration from the target rear side [14]. Only a fraction η of about one quarter of the laser energy \mathcal{E}_L is converted into fast electrons having a mean energy of:

²e in equation (1.19) denotes Euler's number.

$$k_B T_e \approx m_e c^2 (\gamma_{os} - 1) \quad (1.21)$$

at the target front side [9]. This results in a total number of hot electrons that propagate through the target and arriving at the rear side:

$$N_B \approx \frac{\eta \mathcal{E}_L}{k_B T_e} \quad (1.22)$$

The energies for thinner targets cannot be explained by the TNSA mechanism assuming a step-like density gradient at the rear side. Plasma is formed at the target rear surface because of the ASE pre-pulse reducing the acceleration fields [9, 19].

Chapter 2

Laser Facilities

This chapter is focused on describing the laser systems where the experiments on ion acceleration were performed. The domestic experiments presented in this thesis work were performed at the Ti:Sapphire femtosecond laser laboratory recently installed at PALS (Prague Asterix Laser System) Centre. This was the pilot experiment on ion acceleration by the PALS' fs-laser where our developed diagnostics were employed, as mentioned in Chapter 3. The experimental results are summarized in Chapter 4. Few experiments tests were also performed at the iodine kilojoule laser at PALS as well. Such two lasers are nowadays the most powerful available in the Czech Republic.

Experiments on ion acceleration driven by ultra-intense lasers (intensities exceeding 10^{20} W/cm²) were carried out in foreign international laser facilities with our new diagnostic system and/or special structured targets. One of the experiments was performed in the Advanced Photonic Research Institute (APRI) at the Ultrashort Quantum Beam Facility in Gwangju, Korean Republic. This experiment was mainly focused on using advanced targets in order to increase the laser absorption.

Another experimental campaign was performed at the PHELIX laser system at GSI Helmholtz Centre for Heavy Ion Research in Darmstadt. This experiment was aimed to test our newly developed real-time diagnostics for measurements of plasma electron and ion temperature, as well as plasma quasi-neutrality close to the target. The development of the diagnostics used at PHELIX is a crucial part of this thesis and it is further described in Chapter 3.

In order to compare the results from several experiments done in different facilities the following parameters are widely used for the description of the laser beam: pulse duration τ , energy \mathcal{E}_L , peak power P and peak intensity I in the focal spot. One of the parameters widely used is the $I\lambda^2$ [W/cm² · μm^2] giving the information about the laser in the focus. The laser energy for a given pulse duration (at FWHM) is:

$$\mathcal{E}_L = P \cdot \tau \quad (2.1)$$

For example a 15 TW laser beam with pulse length 40 fs has pulse energy of 600 mJ. For a given laser power P with Gaussian profile and laser beam diameter of Gaussian profile d in the focus (beam diameter measured at $1/e^2$), the on axis peak intensity of such laser beam is defined as [20]:

$$I = \frac{8P}{\pi d^2} \quad (2.2)$$

also called laser power density. One of the parameter widely used is the laser contrast:

$$L [\text{dB}] = 10 \cdot \log \left(\frac{I_{\text{MAX}}}{I_t} \right) \quad (2.3)$$

where I_{MAX} is the maximum intensity and I_t is the intensity of the pulse pedestal in a given time t . Other parameter which is mostly mentioned is the f-number ($f/\#$) which is given strictly geometrically by a ratio of focal length F and the diameter D of the beam before focusing:

$$f/\# = \frac{F}{D} \quad (2.4)$$

For the focal spot characterization we assume that the measured spot on the camera has a normal distribution in both vertical and horizontal direction:

$$f(x) = \frac{1}{\sigma\sqrt{2\pi}} e^{-\frac{(x-\mu)^2}{2\sigma^2}} \quad (2.5)$$

where μ is the location of the peak and σ^2 is the variance, the measure of the width of the distribution. The full width half maximum (FWHM) of the distribution comes from:

$$f(x) = \frac{1}{2}f_{\text{MAX}}(x) = \frac{1}{2}f(\mu) \quad (2.6)$$

and the FWHM is then:

$$\Delta_{\text{FWHM}} = 2 \cdot \sqrt{\ln 4} \cdot \sigma \approx 2.35 \cdot \sigma \quad (2.7)$$

whereas the width value at $1/e^2$ comes from the equation:

$$f(x) = \frac{1}{e^2} \quad (2.8)$$

where e is the Euler number and the value of the width at $1/e^2$ is then:

$$\Delta_{1/e^2} = 4\sigma \quad (2.9)$$

2.1 Iodine kJ Laser System at PALS

The core of the PALS facility is a giant iodine laser system, one of the biggest laser in Europe. In the present configuration the fundamental wavelength is 1315 nm (by using DKDP crystal it is possible to convert the beam into the third harmonics at a wavelength of 438 nm). This system is capable to deliver infrared pulses with a 1 kJ nominal energy, which can be split and guided into another beam to be used as a pre-pulse and send to a secondary interaction chamber. The usual maximum energy delivered to the primary interaction chamber at the fundamental wavelength is about 600 J. As can be seen from the Table 2.1 the pulse length of the laser beam is about 350 ps which means the peak power of 1 kJ beam is almost 3 TW (the peak power of 600 J beam delivered into the target chamber is almost 2 TW) and the beam is focused by aspherical lens to about 100 μm focal spot diameter. The output laser beam of the PALS laser is stable and has high quality, i.e. it is shot-to-shot reproducible and spatially homogenous.

The laser beam originates in the oscillator and then travels through the amplifier chain. The oscillator part consists of a main master oscillator and a pre-amplifier. The master oscillator generates a sequence of several identical light pulses from which one of them is chosen for later amplification by the help of Pockels cells.

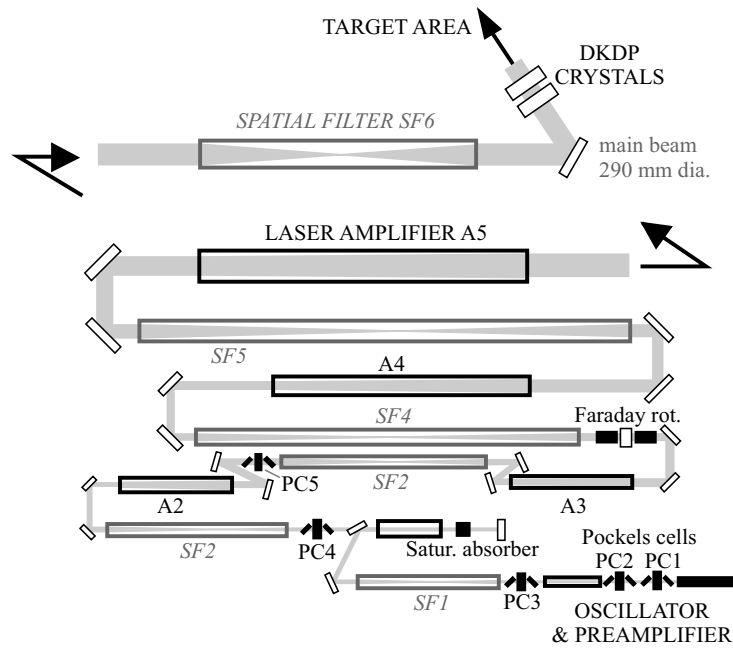


Figure 2.1: The kJ iodine laser system and its components installed at PALS [21].

The choice of the main pulse is triggered with the previous pulse coming through the spark gap switching on the Pockels cells PC1-3 (in Figure 2.1). This pulse also opens the cells PC4 and PC5 later on the laser path. The main pulse is then released into the pre-amplifier and leaving it with an energy of 10 mJ. The next step is the chain of the power laser amplifiers.

The Asterix IV laser chain consists of the five power amplifiers amplifying the pulses from the oscillator part up to 1 kJ energy. The power amplifiers are cuvettes filled by C_3F_7I gas. This gas laser uses iodine atoms for generation of a narrow infrared line at 1315 nm. The mentioned wavelength is generated from the Iodine atoms in the gas medium obtained from the alkyl iodide molecule C_3F_7I by a photochemical process called photolysis. The atom is released from the chemical bond by using UV pulse from a flash lamp. The electron envelope coming from the photolysis reaction is excited and the inversion population is made automatically and the beam can be further amplified to high power.

The amplifier cuvettes are surrounded by these flash lamps charged from capacitors right before the shot. An intensive flash of the non-coherent UV radiation produced by the lamps will create a high number of excited Iodine atoms and their de-excitation will increase the energy of the laser going through the cuvette. The beam size is increasing going from one to the following amplifier starting from the original 8 mm up to the output size of 290 mm. The increment of the laser beam size is made by optical telescopes - spatial filters made by two convex lenses. By this technique the power density of the laser beam is kept below the threshold value at which the surface damage of the optics can occur.

One of the most important devices in the beam path is the Faraday rotator (placed after the third laser amplifier as shown in Figure 2.1) avoiding the amplification of the back-reflected beams which could lead to the damage of the first amplification stage system.

General	Fundamental wavelength	1.315 μm
	Pulse duration	200 ps to 350 ps
	Pulse contrast (pre-pulses & ASE)	~ 70 dB
	Repetition shot rate	25 min
	Output energy stability (over 10 shots)	$< \pm 1.5$ %
Auxiliary beam	Pulse energy at 350 ps	100 J
	Diameter	148 mm
	Conversion efficiency to 3ω	30 %
Main beam	Nominal pulse energy at 350 ps	1 kJ
	Nominal pulse power at 350 ps	3 TW
	Diameter	290 mm
	Conversion efficiency to 3ω	55 %
	Laser energy on target	~ 600 J
	Focal spot size at $1/e^2$	~ 100 μm
	Peak intensity in focus	4.37×10^{16} W/cm ²
	$I\lambda^2$ in focus	7.55×10^{16} W/cm ² · μm^2

Table 2.1: The output parameters from the kJ-class laser at PALS [22].

2.2 TW Class Ti:Sapphire Laser System at PALS

The domestic experiment on ion acceleration by femtosecond lasers was made at the PALS laboratory at the recently installed 25 TW laser system. This system is based on CPA of a Titanium doped Sapphire ($\text{Ti}^{3+}:\text{Al}_2\text{O}_3$) crystal [2, 3].

The titanium sapphire crystal has a broad vibronic fluorescence band which allows a tunable laser output between 670 nm and 1070 nm. In this material, a Ti^{3+} ions is substituted by an Al^{3+} ion in Al_2O_3 . Usually the laser crystal, consists of a sapphire doped with 0.1% Ti^{3+} by weight. Crystals of $\text{Ti}:\text{Al}_2\text{O}_3$ exhibits a broad absorption band, located in the blue-green region of the visible spectrum with a peak around 500 nm. A relatively weak absorption band is observed in the IR region, which has been shown to be due $\text{Ti}^{3+}-\text{Ti}^{4+}$ pairs. The presence of Ti^{4+} ions causes detrimental absorption that interferes with efficient laser operation. Optimized crystal growth techniques and additional annealing processes have drastically reduced this absorption band compared to earlier crystals [23].

The fluorescence peaks at 780 nm, presents a 180 nm bandwidth (FWHM). Therefore, the tunable output from commercial Ti:Sapphire lasers has a higher yield between 700 nm and 900 nm. The laser transition is between vibronic levels - the ${}^2\text{E}$ excited state and the ${}^2\text{T}_2$ ground state in the fluorescent time of 3.2 μs . Optical pumping excites Ti^{3+} to the upper laser level, which then relaxes to the bottom of the vibronic band before making the laser transition. Vibrational relaxation then drops ions to the bottom of the ground-level vibronic band [23]. A strong interaction between the Ti atoms and host crystal, combined

with a large difference in electron distribution between the two energy levels, makes the transition linewidth broad.

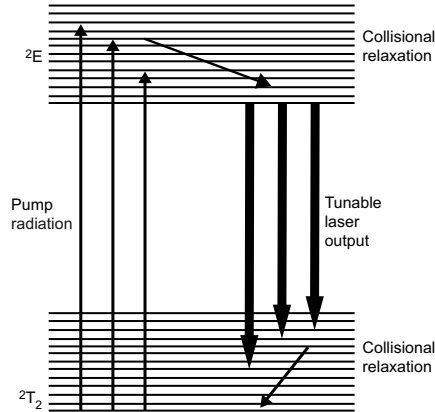


Figure 2.2: Schematic energy level diagram of Ti:Sapphire [23]

The energy level structure of the Ti^{3+} ion is unique among transition-metal laser ions in that there are no d-state energy levels above the upper laser level. The simple energy-level structure ($3d^1$ configuration) eliminates the possibility of excited-state absorption of the laser radiation, an effect which has limited the tuning range and reduced the efficiency of other transition-metal-doped lasers. The outstanding features of Ti:Sapphire are the broad fluorescence line width and the high stimulated emission cross-section [23].

Besides having favorable spectroscopic and lasing properties, another advantage of $Ti:Al_2O_3$ are the material properties of the sapphire host itself, namely a very high thermal conductivity, exceptional chemical inertness, and mechanical rigidity [23].

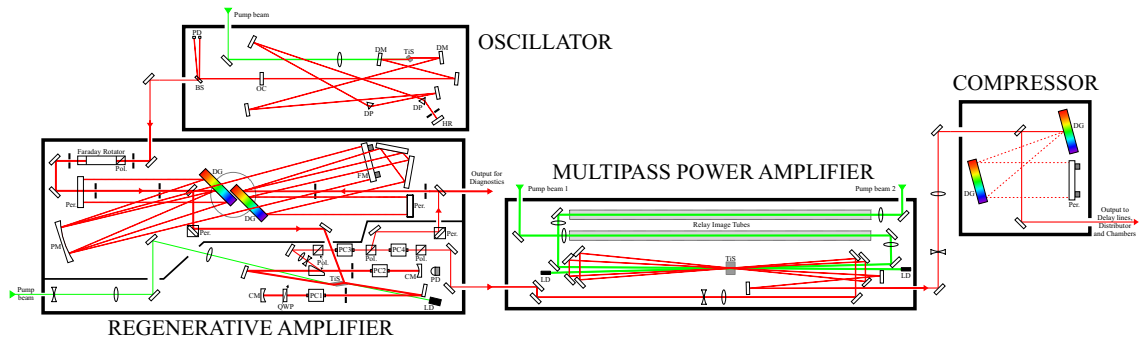


Figure 2.3: The complex scheme of the Titanium Sapphire laser system consisting of the Oscillator, Regenerative Amplifier, Multipass Power Amplifier and Compressor. The more detailed Figures are in Appendix A.

The scheme of the Ti:Sapphire laser system is reported in Figure 2.3. The first source of the laser system beam is a mode-locked¹ oscillator where the beam passes through two

¹Mode locking is a unique technique for generating pulses with femtosecond durations. The laser pulse in mode locked oscillator is circulating for several times in the laser resonator. Each time the laser approach the output coupler mirror a part of its energy is emitted and the laser output is a regular pulse train.

prisms for compensating the dispersion in a laser cavity. The core of the oscillator is a crystal pumped with 4.95 W cw laser at 532 nm. The maximum output spectral width is 120 nm.

Pulses coming from the oscillator are injected into the regenerative amplifier. The incoming beam goes onto the dispersive grid of the pulse stretcher, reflects itself on the parabolic mirror and goes again on the dispersive grid and then in the periscope-like device and again the same trajectory in the stretcher. The original width of 120 nm coming from the oscillator is reduced to 38 nm in the stretcher. It is better to reduce the spectral width as much as possible in order to reduce also the duration of the pulse itself. This spectral width is convenient for the injection into the regenerative amplifier. The beam is totally reflected from a titanium-sapphire (Ti:Al₂O₃) crystal and locked in the cavity by means of co-operation of the seed Pockels cells² and polarizers. This crystal is pumped by 15 W pulsed laser at 532 nm wavelength. The first cell selects an input pulse and sends it into the cavity through the output polariser and then into the dumping cavity Pockels cell. This configuration of Pockels cells will make a pulse train which can be monitored through an oscilloscope. The right timing of the cells is necessary to release the highest amplitude pulse to a pulse-picker or a pulse-slicer which is used for increasing the nanosecond-scale contrast.

In order to increase the contrast the pulse has to come to another set of Pockels cells and polarisers. The first Pockels cell eliminates pre-pulses and leaves the highest pulse and everything behind. The beam comes through the polariser into the second Pockels cell behaving as an active component and eliminates the post-pulses. Through this technique we are able to get contrast of 70 dB of the main pulse with its pedestal. The beam diameter at the output of the regenerative amplifier is about 7 mm.

The laser beam then continues to the multipass at a frequency of 10 Hz. The remaining 990 Hz train is guided to a small compressor and can be used as a diagnostic beam. Its output pulse energy is 1 mJ and the pulse length, measured by a SPIDER³ diagnostic device, is 45 fs whereas the theoretical limit⁴ is 39 fs (see Figure A.5). Such beam can be used in various experimental setups.

The beam continues its path from the regenerative amplifier into the multipass power amplifier. The 10 Hz laser beam is optically guided through the Ti:Sapph crystal four times. The crystal itself can be pumped by a 3 J laser beam at 532 nm (second harmonics of two Nd:YAG lasers). Moreover it is possible to image the second harmonics of the crystal directly on its surface. This second harmonics can serve us as a further diagnostic tool.

On the output of the multipass section a telescope (concave and convex lenses) spreads

²The Pockels cell is the basic component of an electro-optic modulator. It consists of an electro-optic crystal through which a light beam can propagate. The phase delay in the crystal - the so called Pockels effect - can be modulated by applying a variable electric voltage. The Pockels cell then acts as a voltage-controlled wave plate [24].

³Spectral Phase Interferometry for Direct Electric-field Reconstruction (SPIDER) is a method of spectral shearing interferometry for a complete characterization of ultra-short pulses. The signal pulse is split into two identical copies with a significant temporal distance. Another pulse, derived from the same input pulse, is strongly temporally broadened by sending it through a highly dispersive optical element, such as a long block of glass or a pair of diffraction gratings. The long chirped pulse and the two copies of the signal pulse are then combined in a nonlinear crystal where a sum frequency generation is located. The two signal pulses overlap with different temporal portions of the chirped pulse having different optical frequencies. There is also a spectral shear between the two unconverted pulses. Therefore, the optical spectrum of the sum frequency signal reveals the temporally resolved group delay. From the group delay we can acquire the frequency-dependent spectral phase and then the complete pulse characterization is achieved [25].

⁴The theoretical limit is given by a recalculation of the wavelength spectrum to the frequency and its Fourier transform to the time spectrum with a non-constant phase.

the laser diameter from 11 mm up to 40 mm. If the beam coming out from the multipass has an energy of 1.25 J, the fluence will decrease from 1.3 J/cm^2 to less than 100 mJ/cm^2 . This is the condition which has to be fulfilled not to damage the grid in the compressor chamber.

The beam is guided into the compressor onto two dispersive gratings where its width is compressed in time. The zero order position of the beam reflected from the grid can be used for other purposes. This beam has about 50 mJ energy and is guided into a secondary compressor. The remnant part of the beam from the second compressor can be used uncompressed, for instance as a pre-pulse to create a pre-plasma required in specific experiments.

The beam then continues from the grids to the delay line with periscope reflectors in order to set the specific delay between individual laser pulses. In two lines we are able to get about four meters delay. This means that a delay of about eight meters (26.7 ns) between the main femtosecond beam and the non-compressed beam can be set. On the second delay line we are able to set up two meters delay. The vacuum inside the compressor chamber is below 10–5 mBar because this chamber is connected directly with the distribution and interaction chamber. The pressure gradient should be minimal along the whole laser beam path in order to avoid any air flow which can damage or destroy thin foils present in chambers. The same vacuum conditions in all chambers are reached by turbomolecular pumps attached to each chamber.

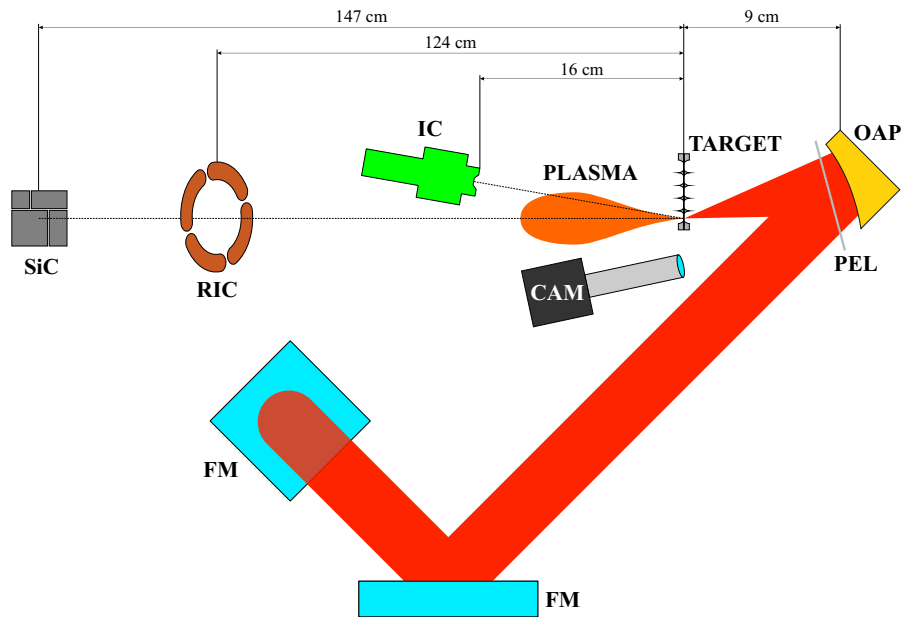


Figure 2.4: Experimental scheme with the laser beam coming from the top reflected by two flat mirrors (FM) onto the off-axis parabolic mirror (OAP) covered by a pellicle foil (PEL) and focused first into the focal point of the microscopic objective with camera (CAM) and after the laser focus optimization the beam was focused on the target creating plasma and fast particles detectable by an ion collector (IC), a ring ion collector (RIC) and a silicon-carbide detector (SiC). The diagnostic devices will be further described in Chapter 3.

The laser beams are then guided from the delay lines into the beam distributor by a set of flat mirrors and directed to the interaction chambers. The beams can be combined and

it is possible to send all three beams from the compressor into the interaction chambers.

In our experimental campaign (first stage of the laser installation) the system was not fully operational with the three output beams. We used only the main femtosecond beam which was guided into the interaction chamber from the top onto a first flat mirror (vertical adjustment), then onto a second flat mirror (horizontal adjustment) and finally focused by a parabolic mirror onto the target, as sketched in Figure 2.4.

The 45 degrees OAP is an aluminum mirror with a gold protective coating. The focusing length is 89.28 mm ($f/\# = 2.2$ according to equation (2.4)). The mirror was set to focus the beam on the target at an incidence angle of 12.1 degrees with respect to the target normal in order to avoid the reflection of the laser beam back to the amplification chain and its consecutive damage. The flat PEL was set in front of the parabolic mirror in order to protect the mirror coating from the target blowout (debris) during the shot. The laser beam propagated through the PEL twice, first going onto the OAP and second focused from the OAP.

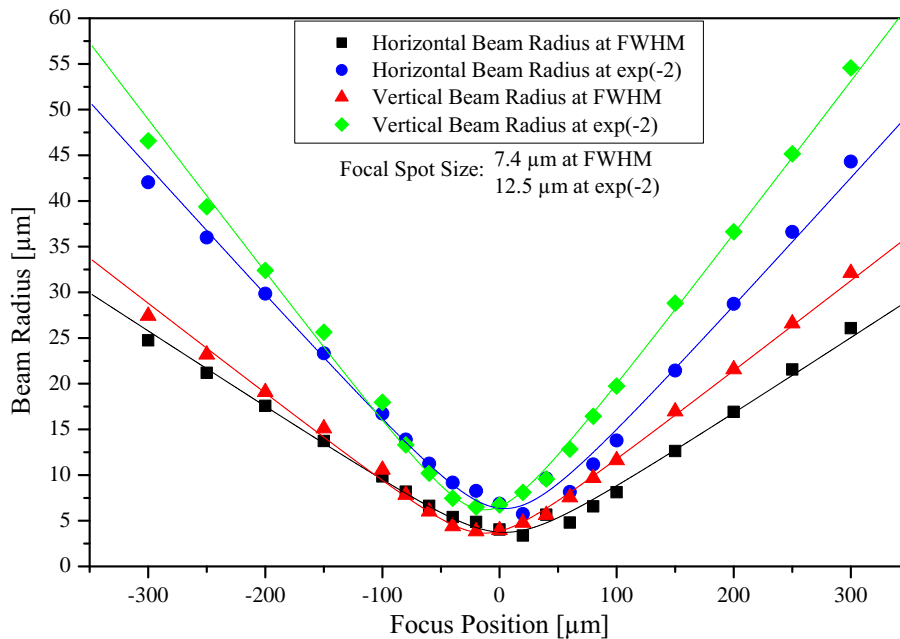


Figure 2.5: Dependence of the beam spot size at FWHM and $1/e^2$ vs. the focus position.

The focusing profile of the OAP was measured under vacuum conditions by a CCD camera with a microscopic objective (magnification 10 - CAM in Figure 2.4). This camera was one body with the structure of the target holder. The dependencies of the beam size vs. the focus position can be seen in Figure 2.5. The beam spot size was measured by means of the horizontal and vertical intensity profile from the camera output. The results from the horizontal and vertical beam spot measurements are then fitted by a Gaussian function and the FWHM and $1/e^2$ values are calculated from the sigma parameter.

From Figures 2.5 and 2.2 reported above, one can see that the measured beam profile was slightly astigmatic, however this was enough for our goals. The minimum measured beam diameter is $12.5 \mu\text{m}^5$ and the corresponding laser intensity in such focus is (assuming

⁵The $1/e^2$ value is widely used in the laser community. The reason to use this value of the beam diameter is that 95.5% of the laser beam energy is in this diameter (taking into account the 4σ of the ideal normal distribution), whereas using FWHM (where 2.35σ is taken into account) covers 76.1% of the laser beam energy.

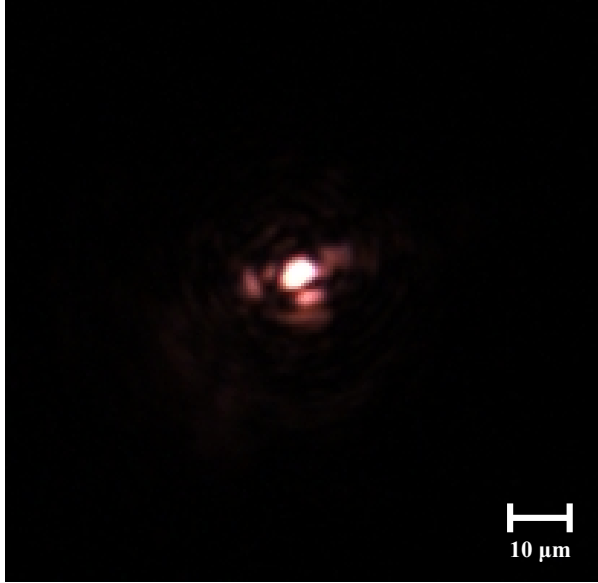


Figure 2.6: Sharp focus of the laser beam at the best (zero) focal position corresponding to the plot in Figure 2.5.

a pulse duration of 45 fs and a laser energy of 520 mJ on the target) $1.88 \times 10^{19} \text{ W/cm}^2$ according to equation (2.2). The overview of the laser system characteristics is reported in Table 2.2.

Maximum laser energy (before compressor)	800 mJ
Central wavelength	808 nm
Laser pulse length	45 fs
Laser energy on target	$\sim 520 \text{ mJ}$
Focal spot size at $1/e^2$	$12.5 \mu\text{m}$
Peak intensity in focus	$1.88 \times 10^{19} \text{ W/cm}^2$
$I\lambda^2$ in focus	$1.23 \times 10^{19} \text{ W/cm}^2 \cdot \mu\text{m}^2$
Laser contrast	70 dB
Polarization	Linear
Repetition rate	10 Hz

Table 2.2: Ti:Sapphire laser specifications.

The optimal focal position was preliminary roughly calibrated by a series of shots performed onto a kapton target (it was used because the material reduces thermal heat destruction). After these procedures the system was ready for inserting the genuine target and aligning it with respect to the experimental axis in vacuum conditions.

2.3 100 TW Ti:Sapphire Laser System at APRI-GIST in Korea

The experiment at the Advanced Photonics Research Institute (APRI - GIST) in Korean Republic was performed using their 100 TW Ti:Sapphire laser system. The principle of working of this CPA system was previously described in Section 2.2.

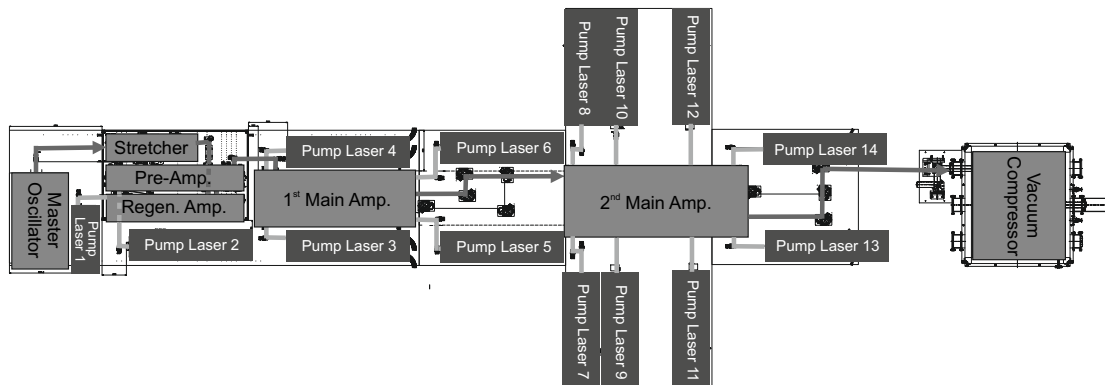


Figure 2.7: Schematic diagram of 10 Hz, 100 TW CPA Ti:Sapphire laser system [26].

The 10 Hz, 100 TW Ti:Sapphire laser system has two main amplification stages. The beam itself is generated at the Master Oscillator and stretched for the amplification in the regenerative amplifier. Schematic draw of the laser system is sketched in Figure 2.7, the principle of CPA laser is the same as in Figure 2.3 for the part of the Oscillator and Regenerative Amplifier (more detailed in Figures A.1 and A.2). The beam power is increased in two stages of the Multipass Amplifiers noted as 1st Main Amp. and 2nd Main Amp. in Figure 2.7. The main scheme of the amplification stage is similar to the one reported in Figure A.3.

The first main amplifier has an output diameter of 30 mm with an output energy of about 2 J. The second amplifier has an output diameter of 50 mm and an energy of 5.6 J. The laser beam is then guided into the pulse compressor chamber with the input beam diameter of 70 mm. Two gratings are set in the compressor with a similar scheme as the one in Figure A.4. Before the beam output a deformable mirror can be placed in order to correct the wave-front profile. The minimum pulse width coming from the compressor is about 30 fs.

From the compressor the beam is guided through the wall of the laser hall into the chamber with plasma mirrors⁶. The main pulse is accompanied by both a pre-pulse and a pedestal that originate from ASE and imperfect compression. For a main laser pulse with intensity above 10^{18} W/cm², the pedestal and pre-pulse can be intense enough to generate a pre-plasma on the target surface prior to the arrival of the main pulse. In this case, the main pulse has a no longer genuine interaction with the target which presents a density gradient. It is extremely important to keep the intensity of the pre-pulse and pedestal as low as possible for relativistic laser-plasma interactions.

During the experiment a double plasma mirror was used in order to increase the

⁶The plasma creation threshold in a dielectric material (usually of about 10^{13} W/cm²) can be reached many picoseconds before the main pulse arrives. The high intensity pre-pulse creates a pre-plasma on the substrate surface and it reflects the main pulse for a further use. This process relies on the ability to form a highly reflecting plasma with a nearly perfect phase front [27].

Maximum laser power (before compressor)	100 TW
Laser energy (after compressor)	4 J
Central wavelength	800 nm
Laser pulse length	~ 30 fs
Laser energy on target	1.92 J
Focal spot size at $1/e^2$	$8.7 \mu\text{m}$
Peak intensity in focus	$2.15 \times 10^{20} \text{ W/cm}^2$
$I\lambda^2$ in focus	$1.38 \times 10^{20} \text{ W/cm}^2 \cdot \mu\text{m}^2$
Laser contrast	110 dB
Polarization	Linear
Repetition rate	10 Hz

Table 2.3: Properties of the 100 TW beamline at the Ultrashort Quantum Beam Facility at APRI.

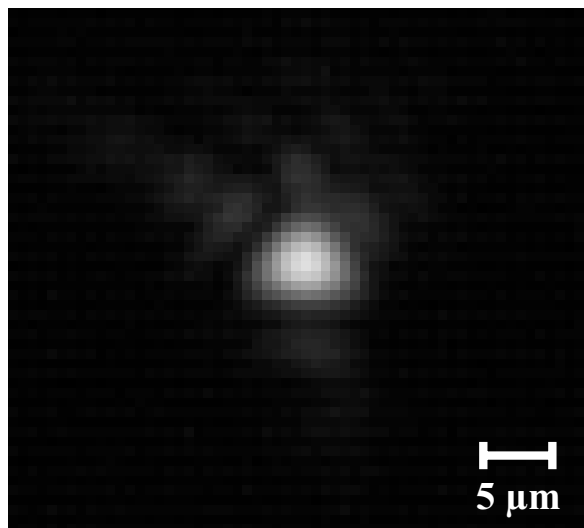


Figure 2.8: Sharp focus of the laser beam at the best (zero) focal position.

contrast up to the value of 110 dB at 6 ps before the main pulse with the overall reflectivity of 59% (with all the optical elements the final reflectivity on the target is 48%) [28]. After passing through the double plasma mirror chamber the laser beam was then focused by an OAP onto the target at an angle of 45 degrees with respect to the target normal. The measured focal spot diameter was $8.7 \mu\text{m}$ at $1/e^2$.

2.4 500 TW PHELIX Laser in GSI Darmstadt

The Petawatt High-Energy Laser for Heavy Ion EXperiments (PHELIX) is a versatile laser facility delivering intense laser beams with energies up to 1 kJ (powers greater than 500 TW). PHELIX is a flash lamp pumped Nd:glass system employing two frontends, a pre-amplifier and a main amplifier.

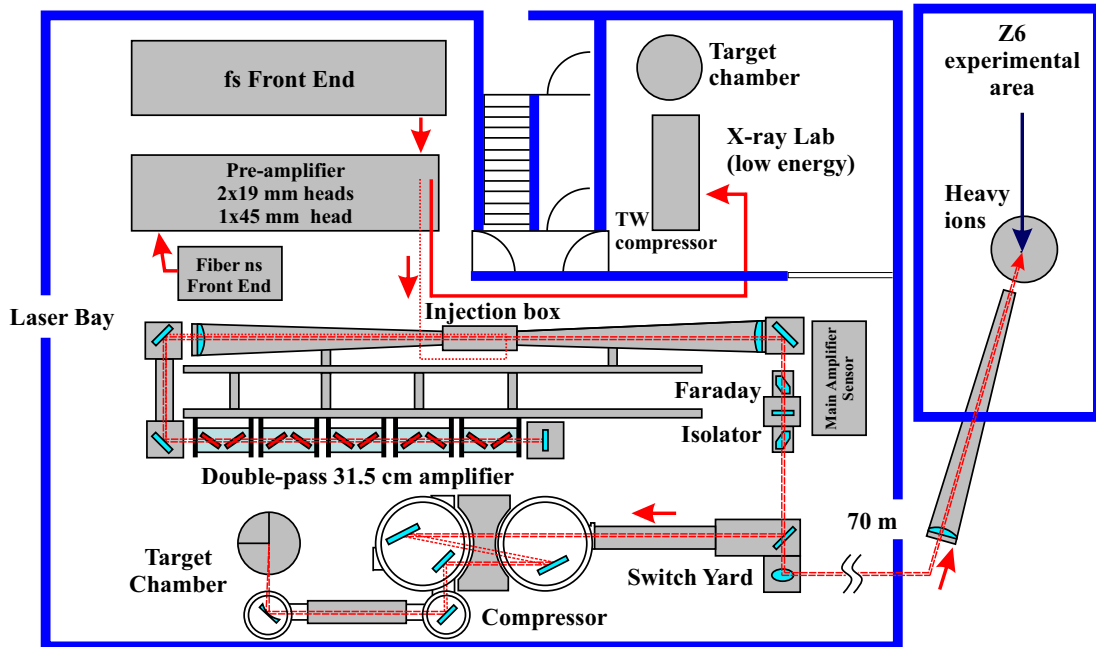


Figure 2.9: Schematic overview of the PHELIX laser system [29].

For the generation of extreme laser intensities greater than 10^{20} W/cm² the chirped pulse amplification scheme (CPA) is used where a sub-picosecond laser pulse is stretched in time, amplified and recompressed afterwards. High energy beams are generated by the nanosecond frontend, which delivers arbitrary pulse shapes and pulse durations between 1 ns and 15 ns.

The first pulse generation is done at the femtosecond-frontend. They are acquired with a commercial laser oscillator which generates pulses with a repetition rate of 76 MHz, a length of about 100 fs and energy of about 4 nJ. The first step of the CPA technique is implemented with the help of an adjustable pulse stretcher. An aspect ratio of 190 ps/nm is sufficient to limit the peak power to levels below the damage threshold of all optical components in the amplifier chain. The stretched pulse is then sent inside two regenerative titanium-sapphire amplifiers where it is amplified with a repetition rate of 10 Hz. The output energy is typically 30 mJ. By using ultra-fast Pockels cells the intensity contrast of more than 60 dB can be reached. In order to generate double pulses a Mach-Zehnder interferometer with an adjustable spacing is used in the beam to obtain different energies and aspect ratios.

The other part of the laser system is the so called nanosecond frontend. The laser pulses can be generated with pulse lengths between 700 fs up to 20 ns and arbitrary pulse shapes. The biggest part of the frontend is made of fibers where a commercially achievable continuous wave laser source is used. The pulses here are generated with duration of 100 ns using an acousto-optic modulator. With this fiber system the pulses with a total energy

up to 10 nJ can be generated. These pulses are amplified up to energies of 20 mJ in the flash lamp pumped regenerative Nd:glass ring-coupled amplifier with the repetition rate 0.5 Hz.

The pulses from the fs and ns frontend are then guided into the preamplifier consisting of three flash lamp pumped Nd:glass. Either the pulses from the fs or ns frontend are gradually injected into Kepler telescopes where the beams are expanded to a diameter of 70 mm in order to keep the intensity below the damage threshold of optical components. Wave-front distortion can be corrected by a deformable mirror. This mirror is actively driven in a closed-loop control cycle with a Shack-Hartmann sensor. Since this sensor is positioned at the end of the amplifier chain, the mirror can also correct errors caused by the main amplifier.

The main amplifier is designed in the way that the light pulse is amplified by means of a double pass through the five Nd:glass flash lamp pumped amplifier heads. The Brewster angle windows are installed in each head of the two amplifiers. With a beam diameter of 31.5 cm, the output energy could reach 1 kJ (at a laser pulse length of 10 ns), but it must be limited because of the damage threshold of the Faraday isolator in the laser path to the switchyard (the set limit is 1 kJ of energy). The Faraday isolator is necessary in order to suppress as much as possible the back reflections from the experimental chamber.

The laser pulse comes from the switchyard into the compressor chamber. The stretched pulse coming from the fs-frontend can be recompressed inside the pulse compressor after passing through the amplifier chain. An output power of 500 TW can be achieved. Inside the compressor there are two optical gratings, which are 48 cm wide and operates in a single pass regime. After basic adjustment of the configuration of these large compressor's gratings, the pulse duration of the compressed pulse can be also adjusted with the help of the pulse stretcher at the fs-frontend.

An acentric copper parabolic mirror which is operated at an incident angle of 45 degrees and a focal distance of 1.5 m is used. Behind the pulse compressor the parabolic mirror focuses the laser beam into the target chamber and intensities exceeding 10^{20} W/cm² can be achieved in ideal conditions. In our experimental campaign a zero degrees incidence angle was applied on a 10 μm gold target. Unfortunately the parabolic mirror was damaged and our standard focal spot is the one reported in Figure 2.10, showing a very astigmatic beam.

Maximum compressor output energy	140 J
Central wavelength	1053 nm
Laser pulse length	~ 500 fs
Focal spot size at $1/e^2$	Horizontal 130.3 μm, Vertical 38.6 μm
Peak intensity in focus	1.42×10^{19} W/cm ²
$I\lambda^2$ in focus	1.57×10^{19} W/cm ² · μm ²
Laser contrast	60 dB
Polarization	Linear
Repetition rate	1 shot per 1.5 hours

Table 2.4: Beam parameters of the PHELIX laser system [29].

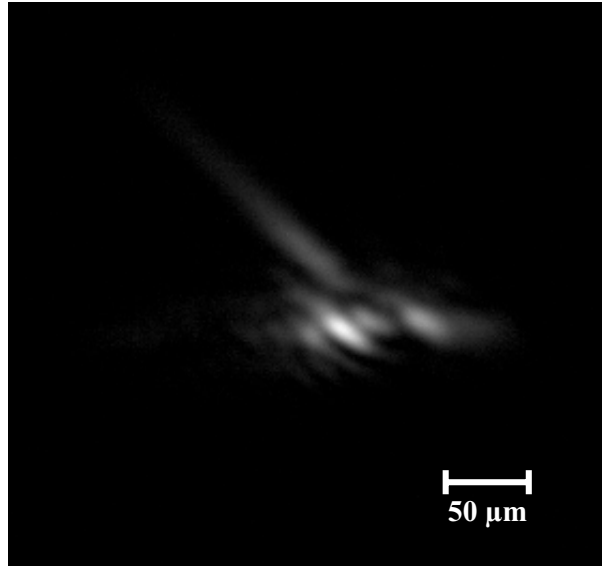


Figure 2.10: The beam profile in the sharp focal position inside the target chamber during our measurement.

The PHELIX laser facility consists of three experimental areas. The Z6 experimental area which is a worldwide unique combination of intense laser radiation with heavy ion beams generated at GSI's accelerator facility (UNILAC). This combination opens the door for interesting experiments in the field of plasma physics, nuclear physics and atomic physics. In addition, stand-alone experiments with intense laser beams can be carried out for studies such as proton acceleration or X-ray laser generation. For moderate beam intensities up to 10 TW an additional pulse compressor and target chamber is available.

Chapter 3

Real-Time Diagnostics

The choice to develop and use real-time diagnostic systems in various experiments was motivated by several advantages with respect to the so-called ex-situ diagnostics. In fact in a typical laser-plasma based experiment, which is set up under vacuum conditions ($10^{-6} - 10^{-5}$ mbar), the ex-situ diagnostic systems allow the experimentalist to evaluate the data only at the end of it, i.e. after ventilating the vacuum chamber, whereas the real time diagnostic devices can store the experimental data shot by shot and in vacuum conditions. This is a big advantage since it gives the possibility to adjust the experimental parameters in real-time and optimize them for the following shot. Furthermore, since the high intensity laser available nowadays and the ultra-high intensity laser systems recently under construction (e.g. at ELI Beamlines¹) potentially offer the possibility to work at high repetition rate (typically 10 Hz), real-time diagnostic systems are mandatory.

This chapter is aimed to give a general overview of the real-time diagnostic systems used in various experimental campaigns performed at different laser facilities. These diagnostics are classified into two categories: energy spectrometers and time-of-flight (TOF) detectors.

The main characteristics of an energy spectrometer is that the signal recorded is capable to provide the plasma ion energy distribution. One of the spectrometers used in this thesis work is the ion energy analyzer (described in Section 3.1) which gives a current signal proportional to a certain ratio of the ion kinetic energy and its charge state depending on the applied voltage on the spectrometer deflecting plates. On the other hand the used Thomson parabola spectrometer (see Section 3.2) gives an optical signal position-dependent recorded as parabolas drawn on a phosphor screen (this signal is time-integrated).

The second class of detectors, widely used in laser-plasma experiments, are the ones placed in TOF configuration, where the ion voltage (i.e. current) signal response at a certain time gives information correlated with the velocity (the detector is placed at a given distance from the source) and the intensity (i.e. number) of the impinging particles. Thus the time dependent ion current distribution is measured, allowing to recalculate indirectly the ion energy distribution. As TOF detectors it is possible to use various devices, such as semiconductor detectors, e.g. silicon, silicon carbide, diamond ones (see Section 3.3), or simple Faraday cups (widely called ion collectors) with suitable time response (described in Section 3.4), which present the main advantage to be absolutely calibrated and to give an ambipolar current response allowing to distinguish the contribution coming from plasma ions or electrons.

In order to distinguish the plasma charged particles from the UV/X-rays the TOF detectors should be placed in a far distance from the target where the time gap between

¹<http://www.eli-beams.eu/>

these two different plasma products is significant. On the other hand, placing the detector at further distances is reflected in a reduction of its solid angle and subsequently in a decrease of the signal amplitude (because of the lower number of impinging particles). In extreme cases this can lead to a decrease of the signal below the detector noise. Thus, in order not to move the detector into further distances from the target (particle source) we developed an array of Faraday cups (see Section 3.5) which can be placed close to the target (few tens of centimeters) inside the interaction chamber.

3.1 Ion Energy Analyzer

The ion energy analyzer (IEA) is a device aimed to determine the ion energy distributions and abundances of the ion species in the plasma [30]. The main part of the IEA is a detection system consisting of two coaxial metallic cylinders (R_1 inner radius and R_2 outer radius) charged at a proper potential (V_1 and V_2). The schematic drawing of the IEA is reported in Figure 3.1.

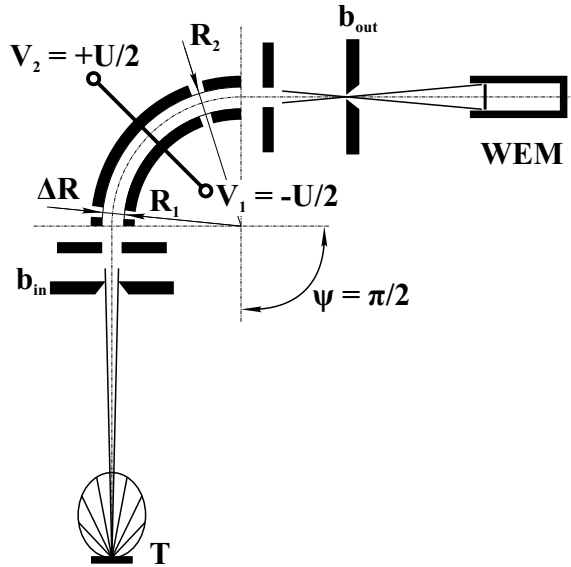


Figure 3.1: Scheme of the IEA. Plasma is produced at the target T heading to the deflection system of the IEA and further to the detector WEM (windowless electron multiplier). The input and output slits b_{in} and b_{out} collimate the ion beam entering and leaving the IEA [30].

The ion trajectory is detected by a radial electric field inside the detection system. When the equilibrium between the centripetal force acting on an ion with charge state z and the force affecting the ion in the radial electric field of the detection system occurs, the energy-to-charge state ratio is:

$$\frac{\mathcal{E}}{z} = \frac{e(V_2 - V_1)}{2 \ln(R_2/R_1)} \quad (3.1)$$

where e is the elementary charge, the inner radius is $R_1 = 10.25$ cm and the outer radius is $R_2 = 10.5$ cm. If the cylinders are charged at potential $V_2 = -V_1 = 3$ kV and one wants to measure the carbon ion C^{5+} , its kinetic energy is $\mathcal{E} = 622$ keV. Considering:

$$\mathcal{E} = \frac{1}{2}mv^2 \quad (3.2)$$

where m is the mass of the ion and v is the velocity given by the ratio between the distance L of the detector and the time-of-flight (TOF), i.e. the time needed for the ion to reach the distance L . From equations (3.1) and (3.2) the TOF is:

$$\tau = L\sqrt{\frac{m \ln(R_2/R_1)}{Z e (V_2 - V_1)}} \quad (3.3)$$

For the same values of R_1 , R_2 , V_2 , V_1 and the distance $L = 2$ m the time of flight of the C^{5+} will be $\tau = 630$ ns. The typical spectrum of the IEA is reported in Figure 3.2. It can be seen from equation (3.3) that only ions with certain charge-to-mass ratio can pass through the IEA and reach the detector. The detector WEM registers the voltage caused by the impact of the ions depending on their time of flight. For known IEA parameters and TOF the charge-to-mass ratio is determined from equation (3.3).

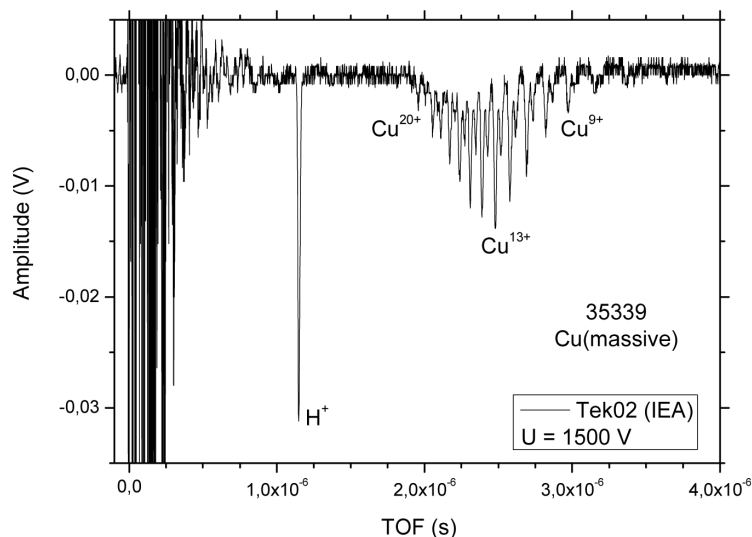


Figure 3.2: Typical IEA spectrum.

The main disadvantage of the IEA is the requirement of a large number of laser shots in order to obtain the ion energy distribution [30]. Moreover, the maximum voltage which is possible to bring on the coaxial metallic cylinders gives the limitation to detection in the maximum proton energy at a value of 0.6 MeV.

3.2 Thomson Parabola Spectrometer

The Thomson parabola (TP) can be considered a mass spectrograph. Charged particles propagate through the TP and are deflected by static electric and magnetic fields parallel to each other and perpendicular to the motion of the charge particle stream. The stream is recorded on an imaging plane which can be based on a radio-chromic film (RCF) detector or a micro channel plate (MCP).

Ions are influenced by the electric and magnetic fields and their trajectory is a consequence of the laws of motion, i.e. when charged particles enter the direction perpendicular

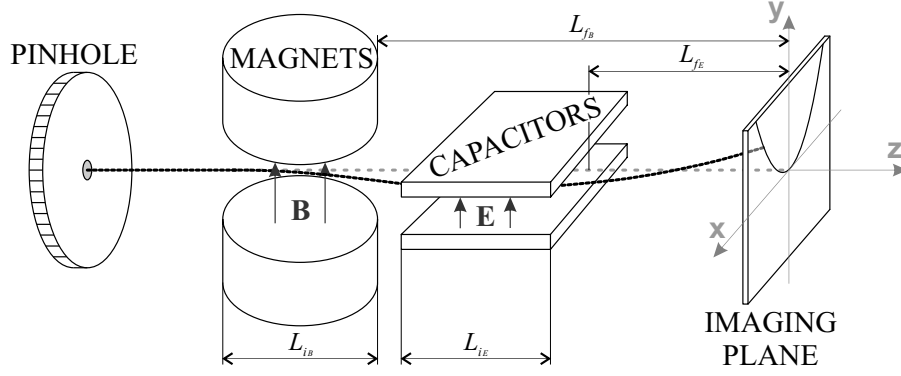


Figure 3.3: Schematic draw of the Thomson parabola analyzer. Particles propagate through the parallel \mathbf{B} and \mathbf{E} field initiated by permanent dipole magnet (or electro-magnet) and capacitor plates. Ions are separated due to their charge states and mass in a presence of fields and then impact the imaging plane drawing the parabola lines.

to the parallel fields, the particles will draw the parabola on the imaging plane. The position of x and y coordinates can be determined from the Lorentz force equation (equation (B.1) in Appendix B). When the ion motion is non-relativistic and the Larmor radius is much larger than the magnet length, ion experiences parabolic deflection depending on its velocity. The deflection position x after the magnetic field action and the deflection position y after the electric field action satisfy the following equation:

$$x = \frac{qBL_{iB}}{mv} \left(\frac{L_{iB}}{2} + L_{fB} \right), y = \frac{qEL_{iE}}{mv^2} \left(\frac{L_{iE}}{2} + L_{fE} \right) \quad (3.4)$$

where B and E are parallel magnetic and electric fields, L_{iB} and L_{iE} is the length of the magnetic and electric field, L_{fB} and L_{fE} is the distance from the magnet and capacitors to the imaging plane. The derivation of these two equations is shown in Appendix B. In the standard experimental setup (e.g. [31]) the lengths of the applied electric and magnetic field are the same (i.e. $L_{iB} = L_{iE} = L_i$) and the magnets and capacitors are concentrated in the same distance, thus the field-free region is the same (i.e. $L_{fB} = L_{fE} = L_f$). The equation of parabola can be estimated from equation (3.4) by eliminating v and assuming usual setup condition [31]:

$$y = \frac{m}{q} \frac{2E}{B^2 L_i (L_i + 2L_f)} x^2 \quad (3.5)$$

Full parabola equation is derived in Appendix B and the general parabola equation is reported in (B.27). The interesting thing in this kind of Thomson parabola setup is that the velocity can be calculated only from the (x, y) position and known the electric and magnetic fields no scaling of the distances or the real dimensions of imaging plane is needed:

$$v = \frac{E}{B} \cdot \frac{x}{y} \quad (3.6)$$

The origin of our system (position $(0, 0)$) corresponds to zero-deflection point where usually the plasma x-rays coming through the pinhole make the mark of this position on the imaging plane. The kinetic energy can be then calculated by substituting the velocity obtained in equation (3.6) into equation (3.2), where the particle mass is obtained from equation (3.5) by analyzing the experimental results.

Looking at the Thomson parabola spectra (and equations (3.4)) we can observe that every vertical line with fixed x position has a constant momentum per charge (mv/q), and every horizontal line with fixed y position has a constant energy per charge ($mv^2/2q$). Every straight line coming through the zero-deflection point has the same velocity not dependent on the particle specie or its charge state (equation (3.6)). Ions with different charge-to-mass ratios (q/m) are separated in different parabolas (equation (3.5)).

When several ion species are present, ions with a certain mass but different charge states can be sorted and lined up for serial ionization stages by checking equal distances between adjacent parabolas along the constant velocity line. Specie, mass and charge-to-mass ratio of an unknown ion may be found from that of known ions [32].

The recording system of a TP can be constituted by two different types of detectors, track detectors or image converter with or without a microchannel plate of high diameter used as an amplifier (usually coupled with a phosphor screen and a CCD camera) [30]. The widths of the parabolas are influenced by the quantity and charge state of impinging ions, the time of flight and the geometry of the measurements. It can also be seen from the experiments that ions of certain charge-to-mass ratio with lower energy are more affected by the space charge than ions with higher energy, thus the parabolas are wider for ions with lower energies.

Track Detectors

The nuclear track detectors are usually plastic polymer foils. When a particle crosses this foil it produces damages at the level of polymeric bonds within a cylindrical region extending to a few tens of nm around the particle trajectory [33, 34]. The result of the bond destruction is a visible track made by the particle trajectory. The TP coupled with the track detector is not a real time diagnostic device because after each series of shots it has to be disassembled and after that the irradiated foil can be evaluated precisely.

Phosphor Screen

The phosphor screen is an imaging plane containing impurities. When the incoming particle hits the screen it can excite electrons leaving the hole in the valence band. The phosphor screen impurities are typically chosen in order to emit photons in the visible range during the electron de-excitation process. Properly chosen impurities in the phosphor screen are convenient for recording this luminescence by a CCD camera.

Microchannel Plate (MCP)

A MCP is a panel made from a high resistive material which thickness is typically about 2 mm. This panel has a regular array of tiny tubes (microchannels) leading through the panel from one side to the other one with a dense distribution over the whole surface. The microchannels are approximately 10 μm in diameter (or less for the high resolution MCP detector) and the space separation between one channel and the following is approximately 15 micrometers.

The TP configuration with the phosphor screen and the camera looking at it can be used as a real-time diagnostics. This configuration can be used at a proper distance from the target where the particle stream is intense enough to be converted in a useful signal. When the particle flux is not high or the TP is placed far from the target (small solid angle) it is needed to use the MCP in order to increase the ion signal impinging onto the phosphor screen and enabling its further recording on camera.

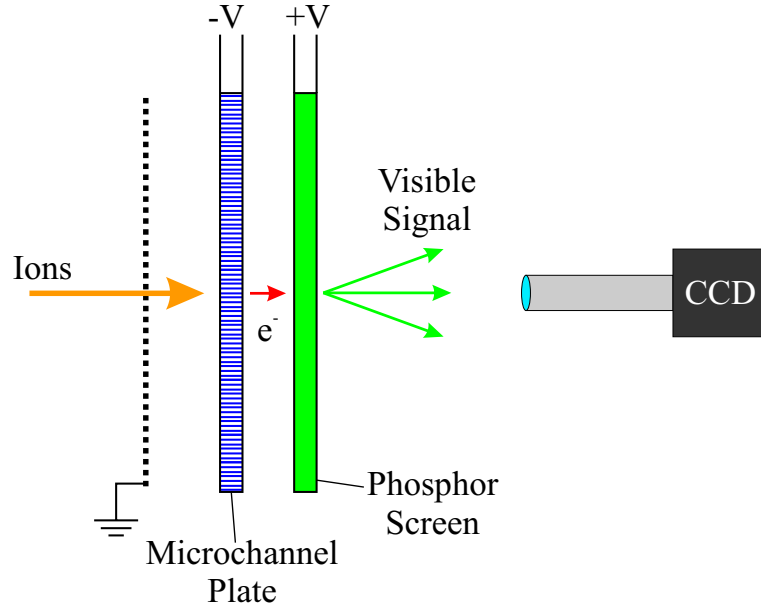


Figure 3.4: Configuration of the TP imaging plane using the MCP to intensify the incoming ion signal, phosphor screen to convert the electron signal into the visible light registered by CCD camera.

The use of the TP coupled with track detector offers an advantage against the other TP real-time configuration reported above: it does not imply any additional electric field in the direction of the particle propagation and thus the use of equation (3.5) is more accurate than in case of applied voltage on the MCP or Phosphor screen. However, equation (3.5) is not absolutely precise even for track detectors since it has other limiting conditions, as reported in Appendix B. A precise evaluation of the results obtained from the TP device should even take into account the non-uniformities distribution and edge effects of all fields present in the TP system.

3.3 SiC Detector

A semiconductor detector is constituted by one or more rectifying junctions above the active region constituted by a low doped or intrinsic semiconductor. The junctions operate under reverse bias with typically applied voltage from several tens to few thousands volts. The reverse bias generates a high electric field region in the semiconductor, depleted by the charge carriers. Photons or particles impinging such detector are interacting with the semiconductor lattice generating a number of electron-hole pairs proportional to their energy.

The charge carriers, generated inside the high field region, drift toward the detector's anode (in case of electrons) and cathode (in case of holes), respectively, producing a current pulse at the electrodes. A charge amplifier connected to the anode or cathode is used to integrate the current pulse. The amplitude of the step-like output voltage is proportional to the collected charge and also to the radiation energy. For this reason the energy spectroscopy is feasible for photon/particle counting.

Semiconductor detectors can provide excellent performances for their high speed of response and high efficiency. They are able to reach a high energy resolution at room temperature and thus, usually, there is no need for their cryogenic cooling. These detec-

tors can be manufactured with a large active volume and there is also the possibility to build semiconductor imaging detector with high position resolution [35]. Those detectors are able to work also in harsh radiations conditions where other types of detectors stop responding.

The physical and electrical properties of the material as the specific growing and device manufacturing technology can play a fundamental role in determining the final performance of the detector. For example, the high energy resolution and the room temperature operation is possible if the device have a low current under reverse bias and this strongly depends on the band gap energy, on the purity and the defect concentration of the semiconductor, and on the quality of the junctions [35].

High speed of the detector response depends on the carrier mobility or on the possibility to operate in velocity saturation regime which requires high electric fields. The detector efficiency, defined as the ratio between the detected photons over the photon hitting the detector, increases with the atomic number Z and the depth of the detector active region, which increases with the possibility to grow high thickness of high purity undoped semiconductor and with the possibility to operate the junction at high reverse voltages.

One of the limits of the detectors made with most of the semiconductors is their relatively high dark current under reverse bias at room temperature. The noise associated to the high leakage current degrades significantly the energy and position resolution of the detectors.

Silicon Carbide (SiC) is a special case of semiconductor with a wide band gap and high saturation velocities of the charge carriers, a high breakdown field and a high thermal conductivity. The energy band gap of SiC is from two to three times wider than pure Silicon, thus the thermally generated dark currents are expected to be almost negligible [35]. The SiC detectors has also the lowest dark currents noise among various semiconductor detectors not only at room temperature but also at high temperature where other semiconductor detectors are not able to operate properly due to their significant noise.

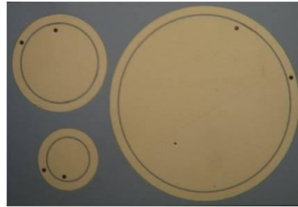


Figure 3.5: SiC pad detectors. Each detector has a surrounding Schottky contact ring whose function is to act as a guard draining the leakage current coming from the chip surface and borders. The black dots on the central and guard electrodes are reinforced areas for wire bondings [35].

There are several factors influencing the SiC detector response by creating a noise in the signal output. One of the factors is the statistic fluctuation of the number of electron-hole pairs generated by a monoenergetic photons, and also the fluctuation of the signal charge amplitude due to trapping and recombination phenomena in the detector. Another additional factor contributing to the noise is the dark current of the detector together with the noise added by the front-end electronics.

As previously mentioned the number of electron-hole pairs is proportional to the energy of the impinging particles/photons, then the current response of such devices is also proportional to the incident energy released into the detector active layer and therefore

the first peak generated by photons (plasma UV or X-rays) is decreased in comparison with the ion peak signal. The current density signal from the SiC is [36]:

$$J = en_e u_{eff} \frac{U_d}{d} \quad (3.7)$$

where e is the elementary charge, n_e is the electron density, u_{eff} is the semiconductor electron mobility, U_d is the bias applied to the semiconductor detector and d is the thickness of the semiconductor active layer. Equation (3.7) can be divided into two parts [36]:

$$J = J_{ion} + J_{phot} = \frac{en_i m_i u_{eff} U_d v_i^2}{2\mathcal{E}_G d} + e\eta \frac{n_\gamma \mathcal{E}_\gamma}{\epsilon} u_{eff} \frac{U_d}{d} \quad (3.8)$$

where J_{ion} and J_{phot} corresponds to the detector response for particles and photons, respectively, \mathcal{E}_G is the energy necessary for electron-hole pair creation, n_i and n_γ are ion and photon density, $m_i v_i^2/2$ is the non-relativistic ion energy, η is the quantum efficiency of the semiconductor and \mathcal{E}_γ is the photon energy.

When using a SiC detector, as well as a Faraday cup, in TOF configuration the photo-peak current signal is used as a trigger for the time resolved measurements. This means that the first point of the photo-peak (usually first point above the noise) is assumed to be the “zero” on the time axis. This relative zero time ensures that the following signals, due to plasma products impinging onto the detector with a certain time delay, are measured with a good accuracy.

Assuming the laser pulse length is much shorter than the sampling rate of the scope (or the rise time of the detector), we can consider all the laser-plasma products as created in the same moment. In order to calculate the particle energy from the TOF measurements it is necessary to take into account also the distance L of the detector from the target. The measured time t_{TOF} has to be corrected onto this distance as:

$$t = t_{TOF} + \frac{L}{c} \quad (3.9)$$

where c is the speed of light (triggering via X-rays). This means that the particle velocity is:

$$v = \frac{L}{t} = \frac{L}{t_{TOF} + \frac{L}{c}} \quad (3.10)$$

and using v from equation (3.10) the kinetic energy is then:

$$\mathcal{E} = \left(\frac{1}{\sqrt{1 - \frac{v^2}{c^2}}} - 1 \right) m_0 c^2 \quad (3.11)$$

The kinetic energy in equation (3.11) is expressed in the relativistic form for the case of measuring high energy particles. For the non-relativistic cases it is possible to use equation (3.2) together with the velocity expression in equation (3.10).

3.4 Ion Collector

The ion collector (IC) is a plane Faraday cup aimed to measure the ion component produced in a plasma during the laser-target interaction. The IC allows a plasma ion and electron separation, usually done by means of a static electric field between the grounded entrance grid and the negatively biased collector. The collector records an ion current by means of a fast storage oscilloscope. However, when the plasma ions reach the collector a

secondary electron-ion emission can occur [30] and may be suppressed by using a further metal grid. If the secondary electron-ion emission is neglected the current density is:

$$I_i = en_e v = ev \sum_{j=0}^{z_{\text{MAX}}} z_j n_{i,j} \quad (3.12)$$

where e is elementary charge, n_e is an electron density and v is the plasma velocity, j is the number of ion species, $n_{i,j}$ is the density of the j^{th} ion specie and z_j is the charge state of the j^{th} ion specie. Using the biased collector, a space charge layer might be formed and shield the collector itself from the plasma. The threshold ion density for this effect is approximately given by [30]:

$$n_{i,z} [\text{cm}^{-3}] \leq 2.5 \times 10^8 \frac{\mathcal{E} [\text{keV}]}{z \cdot d_2 [\text{cm}]} \quad (3.13)$$

where \mathcal{E} is the kinetic energy of the ions with charge state z , d_2 is the distance between the grid and the collector, $n_{i,z}$ is the density of ions with charge state z . It can be seen from equation (3.13) that ions with the lower energy and charge state are more severely limited by the space charge. For a grid-collector distance of 2 cm, an ion energy of 1 keV, and a charge state of 5+, the threshold limitation for the ion density is $2.5 \times 10^6 \text{ cm}^{-3}$.

In reality, the output current I_c in the collector circuit is a combination of ion current I_i and secondary electron current I_e :

$$I_c = I_i + I_e = evTS \left\{ \sum_{j=0}^{z_{\text{MAX}}} [z_j(t) + \gamma_j(t)] n_{i,j}(t) \right\} \quad (3.14)$$

where T is the transparency of the entrance grid, S is the area of the collector, γ_j is the secondary electron-ion emission coefficient, z_j is the charge state, $n_{i,j}$ is the density of the j^{th} ion species where $j = 0$ corresponds to neutral particles. Taking into account that $n_i = \sum n_{i,j}$ in equation (3.14) we can write:

$$I_c(t) = evTS \bar{z}(t) n_i(t) \left[1 + \frac{\bar{\gamma}(t)}{\bar{z}(t)} \right] = T \left[1 + \frac{\bar{\gamma}(t)}{\bar{z}(t)} \right] I_{\text{coll}}(t) \quad (3.15)$$

where $\bar{\gamma} = \sum_j \gamma_j n_{i,j} / \sum_j n_{i,j}$ is the average secondary ion-electron emission coefficient, $\bar{z} = \sum_j z_j n_{i,j} / \sum_j n_{i,j}$ is the average charge state of ions and I_{coll} is the ion current in the entrance grid for a given moment t . Then from equation (3.15) the ion current on the entrance grid is:

$$I_{\text{coll}}(t) = \frac{U_c(t)}{TR_{\text{load}} \left[1 + \frac{\bar{\gamma}(t)}{\bar{z}(t)} \right]} \quad (3.16)$$

where $U_c(t)$ is the voltage amplitude of the collector signal and R_{load} is the load resistance. From equation (3.16) it is also possible to obtain the velocity and energy distribution.

The advantage of using ion collectors instead of semiconductor detector is that Faraday cup is able to give us the total absolute charge of the particle beam. The current density will then be:

$$J_{\text{ions}} = e \sum_i z_i n_i v_i \quad (3.17)$$

As already mentioned above, when the laser hits the target, plasma and accelerated ions are generated together with XUV radiation from the plasma. The radiation spreads through the chamber and reaches the IC as first causing a secondary electron emission from the grid and, as a consequence, the voltage amplitude (called photo-peak) at the output signals. When some plasma radiation reaches the collectors cathode it starts to generate a current signal [36]:

$$J_{phot} = e\eta n_{\gamma} v_e \quad (3.18)$$

where η is the quantum efficiency of the photoelectric mechanism (electron number per incident photon with a given energy) and n_{γ} is the photon density.

Standard ion collectors in TOF configuration widely used to measure laser-plasma characteristics are failing when placed too close to the target. In fact there might be several problems: the broad photo-peak overlaps with the most important signal coming from the fastest particles (usually protons); the electromagnetic pulse is very high; and the time (i.e. energy) resolution of the recorded spectra is low. For this reason we have developed a Faraday cup array in order to set it up close to the target directly inside the chamber in distances smaller than 50 cm at the highest laser intensities available nowadays.

3.5 Design and Development of New Types of Faraday Cups

Usually Faraday cups described in Section 3.4 are used at far distances from the target and placed at the end of a long pipe attached to the vacuum chamber, aiming onto the target. Standard Faraday cups were tested during our experimental campaigns, as reported in Section 4.2, showing a disadvantage linked to the presence of an electromagnetic pulse (EMP) coming from the laser-matter interaction which causes a huge noise at the beginning of the TOF signal. Moreover, if one wants to characterize the accelerated plasma particle beams at the beginning of their expansion in vacuum (few tens of centimeters) it is necessary to use a very fast detection system (the time resolution is low at short distances) as well as a compact setup in order to be placed inside the vacuum chamber. For those reasons a completely new diagnostic system based on the use of a Faraday cup array was designed, fabricated and tested in a preliminary experiment.

The first step before the manufacturing of the Faraday cups was the issue of suppressing the EMP coming from the target and reflected from the chamber walls. In such conditions (especially when one wants to use this detectors at high intensity laser facilities as described in Section 2.4) the whole chamber and every metallic component inside the chamber or attached to it acts as an antenna spreading the electro-magnetic noise around. For this reason we put the electrodes of the Faraday cups inside a Faraday cage². The Faraday cage is capable to shield the interior from external electromagnetic radiation if the cage conductive material is thick enough and its holes are significantly smaller than the radiation's wavelength. A drawing of the Ion collector with two Faraday cups inside, surrounded by the Faraday cage, is reported in Figure 3.6.

The Faraday cage consists of 1 mm thick copper plates and 1 cm thick pedestal. It is 6 cm high, 2 cm wide and 7 cm long. The height, width and length were chosen in order to set the Faraday cups along with the BNC sockets for the signal cables all inside the cage.

²Faraday cage is an enclosure formed by conducting material or by a mesh of such material. Such an enclosure blocks out external static and non-static electric fields. These fields cause the electrical charges within the cage's conducting material to redistribute themselves so as to cancel the field's effects in the cage's interior. What Faraday cages cannot block is static and slowly varying magnetic fields, such as Earth's magnetic field

The copper material was chosen as the most suitable for its high electric conductivity. In Figure 3.6 there are holes in the Faraday cage, two holes on the front are the openings for Faraday cups and one hole for laser alignment in order to aim the collector directly in the right height where the laser hits the target. The other visible holes in the cage are for screws holding the whole structure together. In this Ion collector design there is also one big hole at the rear side of the Faraday cage allowing the signal cables to go out from it and also used to let the alignment laser pass through.

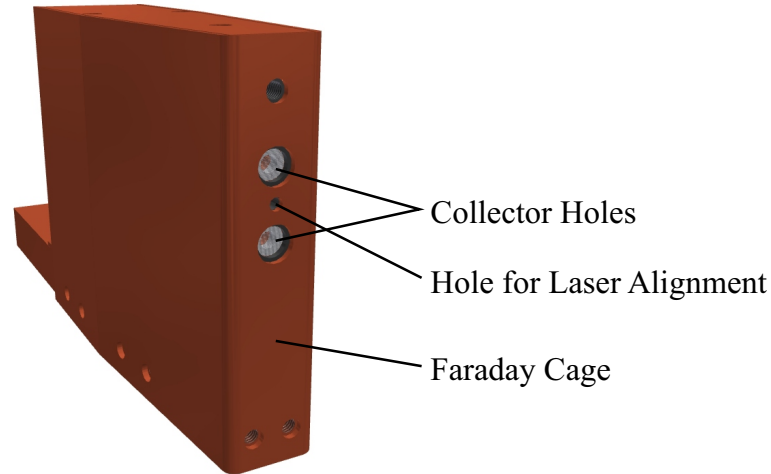


Figure 3.6: Ion collector design with two Faraday cups inside a copper Faraday cage with the hole for laser alignment.

It was mentioned before that the cage is capable to shield the interior if the openings in the cage are smaller than the radiation wavelength. For this reason we have to put small copper pieces in order to blind the holes when the collector is aligned. It is also suitable to wrap a conductive tape around the signal cables coming out from the cage and put also conductive material to blind the hole for the alignment laser.

The Faraday cup itself consists of two concentric copper electrodes shaped as cylinders and settled in the murital³ support inside the Faraday cage, a cross section of one settled Faraday cup is shown in Figure 3.7. The outer cylinder is a shielding electrode which is grounded. Its length is 16 mm with the inner diameter $D = 4.5$ mm. The inner electrode has a diameter of $d = 3.5$ mm and its length is $h = 14$ mm. An aluminium grid is attached in the entrance of the collector for its suppressing effect of the secondary electron-ion emission. The inner electrode is not a standard solid cylinder but a hole with a diameter of 2.5 mm and the hollow part length is 12 mm is made inside the cylinder. Since the diameter of the inner electrode is lower than its corresponding hole in the Faraday cage, a collimator with a hole diameter from 0.5 mm up to 2 mm, according to our expectations from the experiment, is placed in front of the collector.

The configuration of the Faraday cup with the hole in the inner electrode is called emission-less Faraday cup. The main reason of this hole is to suppress the effect of the secondary electron-ion emission described in Section 3.4. In fact, electrons and ions are propagating through the aligned cup impinging onto the rear part of the hole producing secondary emission of particles which are then collected inside the electrode hole side walls

³Murital is a plastic insulator suitable for its applications in high vacuum conditions. Vacuum flanges for feedthroughs, used for various types of signal or power supplying cables for motors, are usually made from murital material.

and thus do not contribute to the main signal since the emission-recollecting process lasts much shorter time than the sampling rate of the oscilloscope. Since the main products of the emission are electrons it is suitable to apply a positive voltage on the electrode in order to increase the emission suppression.

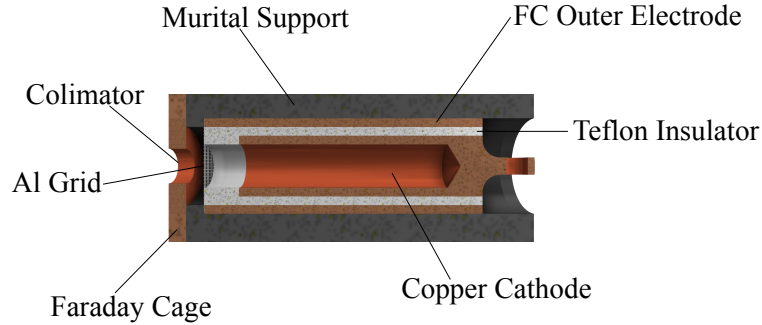


Figure 3.7: The cross section of the Faraday cup consisting of the inner copper electrode where the charge is collected, a Teflon insulator between the inner and the outer electrode recessed inside the marital support with the collimator embedded at the entrance of the Faraday cage.

If the inner electrode has a hole along all its length, the particles would go through without being collected. Such a device is called dynamic Faraday cup. The dynamic response of it would then be determined by the magnitude of the induced charge and the shape of the particle beam. The theory of such device is described in detail in [37]. The dynamic Faraday cup can serve at the same time as an integrating current transformer (ICT⁴).

Our detector is blinded at one side in order to collect the charge carried by the plasma particles. In order to characterize the properties one can assume that the Faraday cup is a coaxial line transferring the current given by the impinging charged particles. Such detector would have the impedance of the coaxial line with fixed ratio of the inner to outer diameter given by equation [39]:

$$Z_0 = \frac{1}{2\pi} \cdot \sqrt{\frac{\mu_0 \mu_r}{\epsilon_0 \epsilon_r}} \cdot \ln\left(\frac{D}{d}\right) \quad (3.19)$$

where $\mu_0 = 4\pi \times 10^{-7}$ H/m is the vacuum permeability, μ_r is the relative permeability of the material between electrodes, $\epsilon_0 = 1/(\mu_0 c^2) = 8.85 \times 10^{-12}$ F/m is the vacuum permittivity, ϵ_r is the relative permittivity of the material between the inner and outer electrodes, D is the inner diameter of the outer electrode and d is the outer diameter of the inner electrode. The capacity is given by equation [40]:

$$C = \frac{2\pi\epsilon_0\epsilon_r}{\ln\left(\frac{D}{d}\right)} \cdot h \quad (3.20)$$

where h is the length of the inner electrode. When applying the bias voltage of $U = +100$ V on the inner electrode, the electric field between the inner and outer electrode is then:

⁴The ICT is a capacitively shorted transformer and a fast read out transformer in a common magnetic circuit designed to measure the charge in a very short pulse with high accuracy [38]. This device is a linear integrator for high frequency spectrum typical for a bunched beam signal

$$E = \frac{U}{\frac{D}{2} - \frac{d}{2}} \quad (3.21)$$

which gives us the electric field of 0.2 MV/m, which is enough in principle for using this configuration in vacuum condition without any material between electrodes. Since the inner electrode has to stand on some support separating it from the outer electrode and since we expect a large amount of charged particle arriving from target, we decided to put the Teflon insulator between electrodes. The dielectric strength of Teflon is 60 MV/m, the relative permittivity and permeability are $\epsilon_r = 2.04$ and $\mu_r = 1$, respectively, keeping constant up to the 9.5 GHz field frequency and further from 10.2 GHz [41]. Substituting the material constants of the Teflon into equations (3.19) and (3.20) we find out the impedance $Z_0 = 10.55 \Omega$ and the capacity $C = 6.32 \text{ pF}$.

In experiments we use 50 Ω BNC cables for signal transmission with the 50 Ω termination resistor. There are also other important elements playing a role in a signal transmission. One of them is related to what is happening to a signal coming from the coaxial Faraday cup into the BNC socket through thin cables. The signal transmission is a more complex problem and it is described at the end of Appendix C.

Once the Faraday cup signal gets over the interfaces into the BNC socket, it continues out from the Faraday cage via 50 Ω triaxial cable. The triaxial cable is used in order to prevent the useful signal from the EMP which would generate an additional noise. The signal is guided through the inner cable into the scope, the outer electrode of the Faraday cup is connected onto the second line of the triaxial cable going to the ground of the scope and the third line is attached on the Faraday cage on one side, and on the target chamber on the other side. It is also better to conductively connect the third line with the second one at some point in order to have the same ground in the chamber and in the oscilloscope, otherwise one can have two grounds which can influence each other.

Finally it is better to attach a metal plate on the chamber wall in front of the feedthrough flange in order to prevent the generation of additional EMP noise. Moreover, behind the flange, a small metallic chamber (in air) containing the collector circuit is placed. The so-called common part for all Faraday cups, reported in Figure 3.8, is the electronic filter preventing transmission of noise signal from the power supply. The applied voltage is the same for all the Faraday cups.

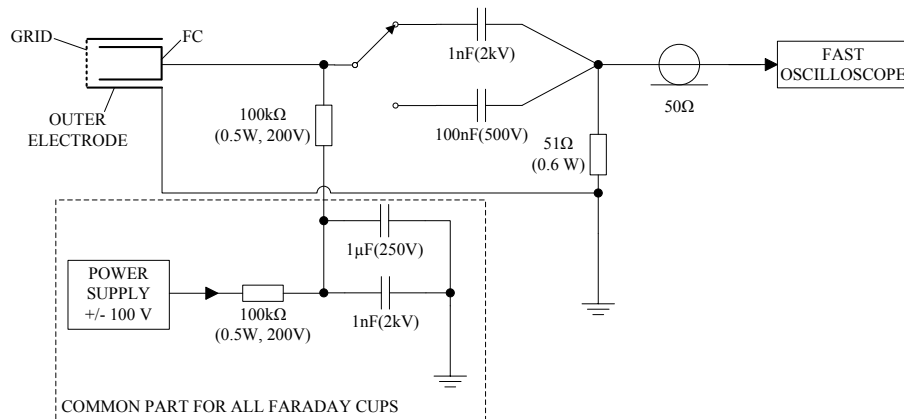


Figure 3.8: The scheme of the electronic circuit of the Faraday cup array.

The other electronic components in Figure 3.8 is the standard collector circuit. The input voltage of each collector is coming through the 100 k Ω resistor. This resistor is

keeping the voltage on the collector plate and in case of a puncture between the grid and the collector it extinguishes the discharge. The voltage is applied on the collector and then the signal is coming through the same cable until it reaches the capacitor which can be switched by jumpers from 1 nF to 100 nF depending on the expected signal length. The capacitors are placed here in order to switch each Faraday cup to be able to detect fast signals (in case of 1 nF) or slower signals (in case of 100 nF). This is correlated to the RC constant of the circuit which gives us the time constant:

$$\tau = RC \tag{3.22}$$

where C is the capacity mentioned above and R is the resistivity of the terminator⁵ applied at the end of the BNC cable. Since we use 50 Ω cables the terminator resistivity has the same value. The calculated time constant in equation (3.22) is the time required to charge a capacitor to 63% of the initial voltage signal. When the capacitor is fully charged then no current will pass through (at the time constant of about $5RC$). For 1 nF capacitor and 50 Ω resistor we get the time constant of 50 ns, this limits our measurement of longer signals (high pass filter).

The last component, before the signal leaves into the coaxial cable and on the input of the oscilloscope, is a 51 Ω resistor connected onto the grounding of the oscilloscope. It helps to prevent from the reflections and it reduces the current output signal to one half, the voltage remains the same. Thus the real current can be calculated from the measured voltage but with a resistance of about 25 Ω .

When working with this array of Faraday cups at big laser facilities (with high laser intensities and huge EMP) it is suitable to shield also the external cables coming from the circuit box into the oscilloscope. It is better to put them in some shielded pipe or bellows and then wrap it into some metallic foil. It is also suitable to put the oscilloscope inside a Faraday cage leaving open only the holes for the input signals. Otherwise the EMP transferred outside the chamber can highly influence the signal recorded on the oscilloscope or it can cause its freeze or even a serious damage.

⁵Terminator is a resistor connecting the inner signal line with the outer ground line of the coaxial cable. The terminator resistance is chosen to be the same as the impedance of the coaxial cables in order to avoid any reflections.

Chapter 4

Results Obtained at Different Laser Facilities

Various experiments of laser-driven ion acceleration have been performed at the laser facilities described in Chapter 2 with the diagnostic systems described in Chapter 3. Various types of targets, as well as different laser pulse durations and wavelengths, have been used during the different experimental campaigns. All the presented results have been obtained in the TNSA acceleration scheme described in Chapter 1 where proton/ion beams are produced from thin solid targets and accelerated forward from the target rear-side, mainly in the direction of the target normal at multi-MeV energies.

The ion diagnostics used along the experimental campaigns can be classified into two categories: time-resolution sensitive detectors (Faraday cups and SiC detectors) and energy sensitive detectors (IEA and TP spectrometers).

As already mentioned the main goal of this work is the development of the Faraday cup array which have been used close to the target where the environment conditions were not convenient for most of other real-time detectors. This system was developed in cooperation with Dr. P. Paris from the Institute of Plasma Physics and Laser Microfusion, and the physical model is presented in Appendix C. The detector has been tested at PHELIX laser system and the experimental results obtained in the different setups allowed to identify advantages and disadvantages of the developed diagnostic system.

4.1 Results from Iodine kJ Laser at PALS

An ion acceleration experimental campaign in the TNSA regime has been performed at PALS using several types of targets and different diagnostic devices: SiC detector, Ion collector and Thomson parabola spectrometer. The SiC detector is applied in this experimental campaign in TOF configuration for its fast response in order to get the fastest proton/ion signal. The application of metallic filters in front of the detector allowed us to minimize the photo-peak and thus separate the beginning of the fast proton signal. The ion collectors are not fast as the SiC detector but they allowed us to determine directly the current from measured ion/electron signal. They work in TOF configuration and the signal can be filtered by the same means and reasons as for SiC detectors. The Thomson parabola spectrometer was employed in this experimental campaign in order to distinguish the contribution of different ions and their charge states, and also as a cross-check diagnostics for the TOF measurement, especially for the fastest proton signals.

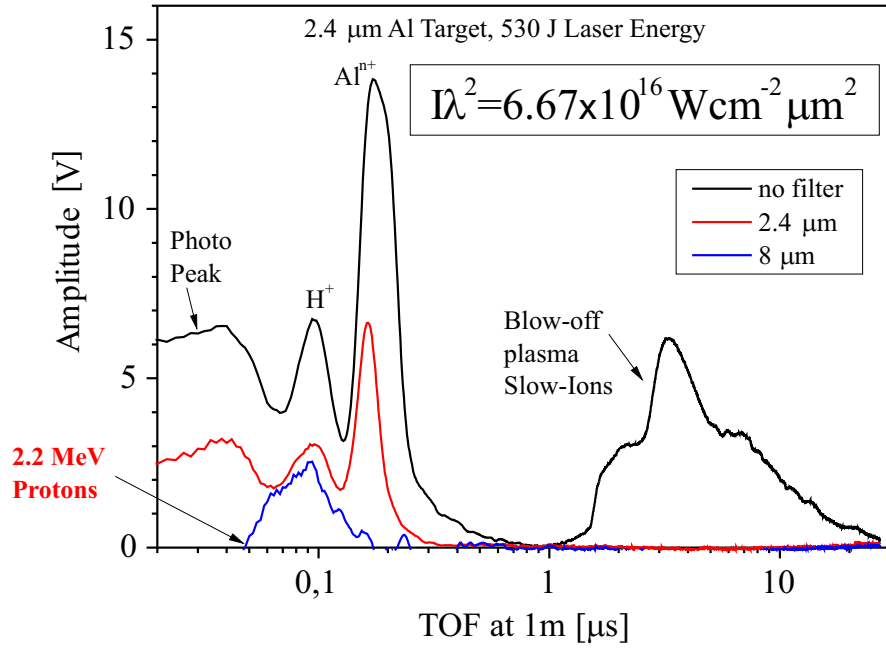


Figure 4.1: Results obtained by the IC diagnostics with several filters cutting off a part of X-rays and enabling the detection of the fastest ions.

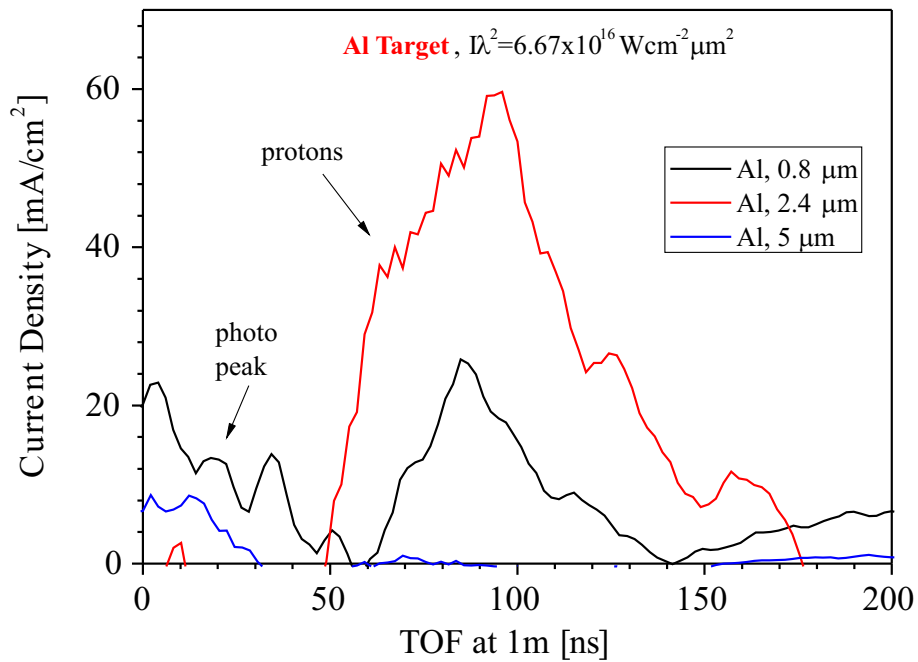


Figure 4.2: Current density signal from the ion collector for different aluminium target thicknesses.

Simultaneous IC experimental measurements obtained, when a filtering technique was used (metallic filters are put in front of the detectors in order to cut off the X-rays and slow ions), are reported in Figure 4.1. The iodine laser pulse at PALS (at fundamental

wavelength) operated with an energy of 530 J was focused into a circular spot of about 100 μm diameter, thus it reached the intensity of $3.86 \times 10^{16} \text{ W/cm}^2$ on target. Aluminium foils of different thicknesses have been used as filters. It is clearly shown in Figure 4.1 that the thickest foil allows to observe the fastest proton/ion signal whereas with the lower thicknesses filters the fastest particles' signal overlaps with the plasma photo-peak. The measured fastest proton signal has a kinetic energy of about 2.2 MeV. The proton signal is followed by a group of heavier ions, they are slower because of lower velocity due to higher mass. Since we used aluminium foil as a target, we can expect that this slower group is composed of aluminium or carbon ions, since carbon may be deposited on the target as surface contaminant. These two main groups of accelerated ions are followed by a blow-off plasma, which is present here due to the target destruction and atomisation. The TOF signal of slow ions coming at μs scales vanishes when the Al filter is placed in front of the ion collector because of the low ion energy.

Results obtained by irradiating different thickness aluminium thin targets are depicted in Figure 4.2. The experimental conditions remained the same as for the results shown in Figure 4.1, while the Al filter was 4.8 μm thick.

From Figure 4.1, the proton kinetic energy is exceeding 2 MeV which should not be reached in this low-intensity regime. Such a high proton energy and long laser pulse duration indicates that some non-linear effects occurred. The laser beam self-focusing already described, where the plasma acts as a convex lens and starts to guide and further focus the beam, can be considered the main responsible of such results, since the real laser intensity on the target surface can be much higher than the nominal one. For 350 ps pulse length, there should be also the possibility that a multiple self-focusing can occur depending on the plasma evolution during the interaction. This phenomenon can be further studied as soon as the Ti:Sapphire fs laser will be available and synchronized with the kJ beamline. In fact the high intensity 25 TW, fs-laser beam might be injected in a pre-formed plasma (generated by the ps-laser) and further focused at very high intensity by the self-focusing mechanism.

4.2 Results from Ti:Sapphire fs Laser at PALS

A pilot experiment on proton acceleration at the new Ti:Sapphire femtosecond laser system recently installed at PALS has been performed. The whole apparatus described in Figure 2.4 was set up in a vacuum chamber (typically at a pressure of about 10^{-6} mbar). The laser beam was roughly aligned at the atmospheric pressure and then precisely adjusted under vacuum conditions by a remote control system able to tune the shape of the laser spot on the target front side which was imaged with the magnification of 10 on a micrometric objective camera.

A target holder with 25 holes allowed to fire 25 consecutive times with the laser onto the same target. The target holder has a sandwich structure with polished surfaces capable to hold tightly thin targets (1–10 μm during the experiment) and preventing them from destruction after each shot.

The angular beam divergence was measured by a radiochromic film (RCF). The distance from the target to the RCF was set to 30 mm. The radiochromic film exposed to a proton/ion beam changes its optical density. The background signal caused mainly by plasma X-rays emission was measured separately and subtracted from the proton signal. The proton beam divergence (a cone presenting the particles' transverse spatial dispersion) calculated from the RCF analysis was about 25 degrees and this is valid for all results presented here.

Three types of diagnostics have been employed during the experiment: a silicon carbide

detector (SiC), an emission-less ion collector¹ (IC) and a ring ion collector (RIC), as depicted in Figure 2.4. These three diagnostics have been employed for the same reason mentioned above. The SiC detector for the fast proton signal measurements, the IC, predecessor of Faraday cup in order to test its properties, and the RIC as a complementary diagnostics. The typical TOF spectra obtained simultaneously from SiC, IC and RIC are depicted in Figure 4.3. The target was a 2.4 μm thick Al foil and the laser energy was 325 mJ (giving the intensity of 1.18×10^{19} W/cm²). The detectors were placed at different distances but the output results are recalculated at 1 m detection distance for mutual comparison.

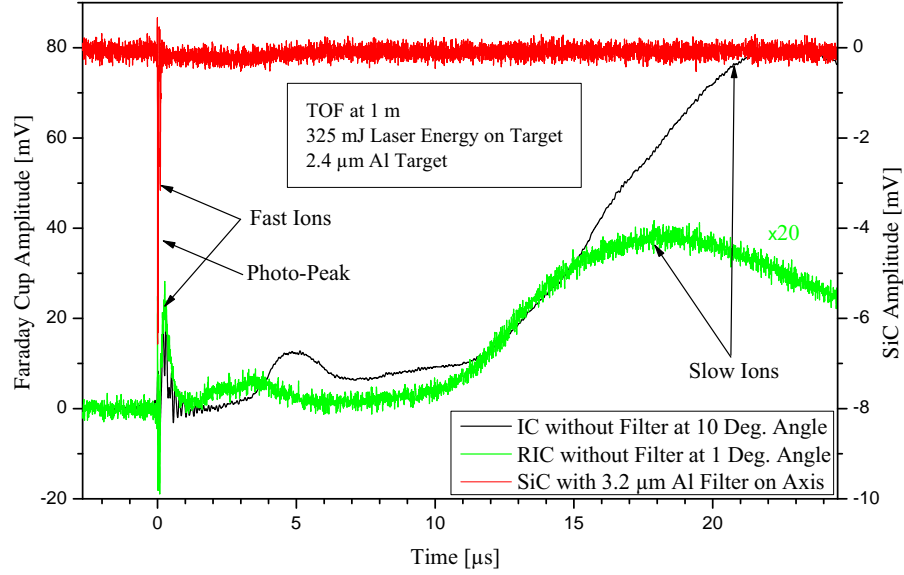


Figure 4.3: The typical TOF spectra obtained from the diagnostics IC, RIC and SiC employed simultaneously during one single laser shot of 325 mJ. The time scale has been recalculated for 1 m detection distance for each device.

The IC was placed at the distance of 16 cm from the target and at the detection angle of 10 degrees (angle between the IC axis and the target normal), the IC sensitive area is $S_{IC} = 12.3$ mm². The transmission of the grid in front of the IC is $T_{IC} = 55.3\%$. The RIC was placed inside a long tube at the 124 cm detection distance and the detection angle of 1 degree. The RIC is divided into four sectors capable to detect four different simultaneous signals. The area of each sector is $S_{RIC} = 211.8$ mm² and its grid transmission is $T_{RIC} = 62.7\%$.

From the TOF spectra reported in Figure 4.4 recorded during a laser shot at 520 mJ (corresponding to intensity of 1.88×10^{19} W/cm²) it is possible to see that particles are faster on axis than at bigger angles. For a better comparison the signals have been recalculated at 1 m detection distance. It is evident that the ion current response of the RIC has a much lower absolute value than the IC one due to the much smaller solid angle.

¹This ion collector is not the one developed in Section 3.5. It is its predecessor. Unfortunately this one is not convenient for the fast ion signal.

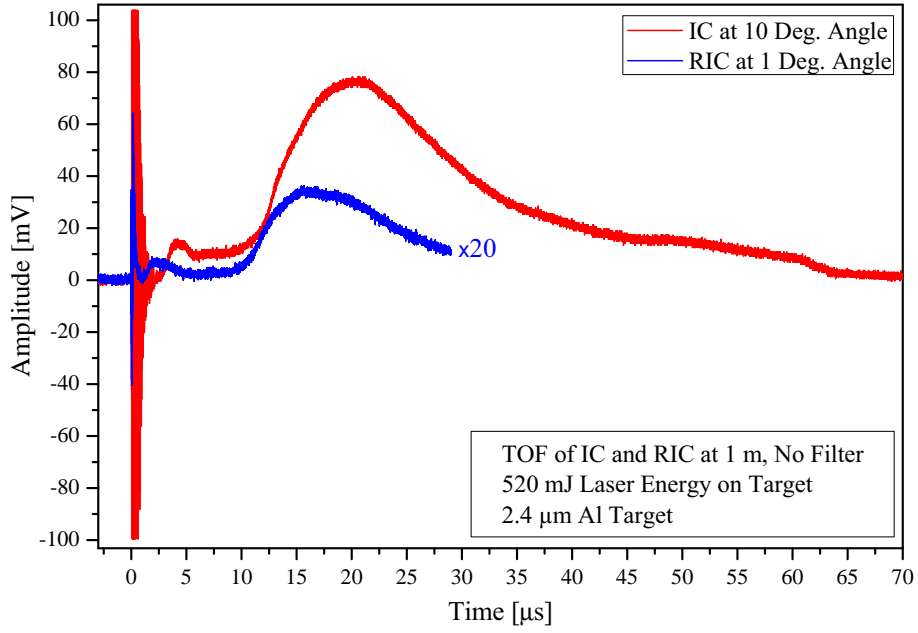


Figure 4.4: Comparison of two different ion collectors (IC and RIC) employed during a laser shot at 520 mJ.

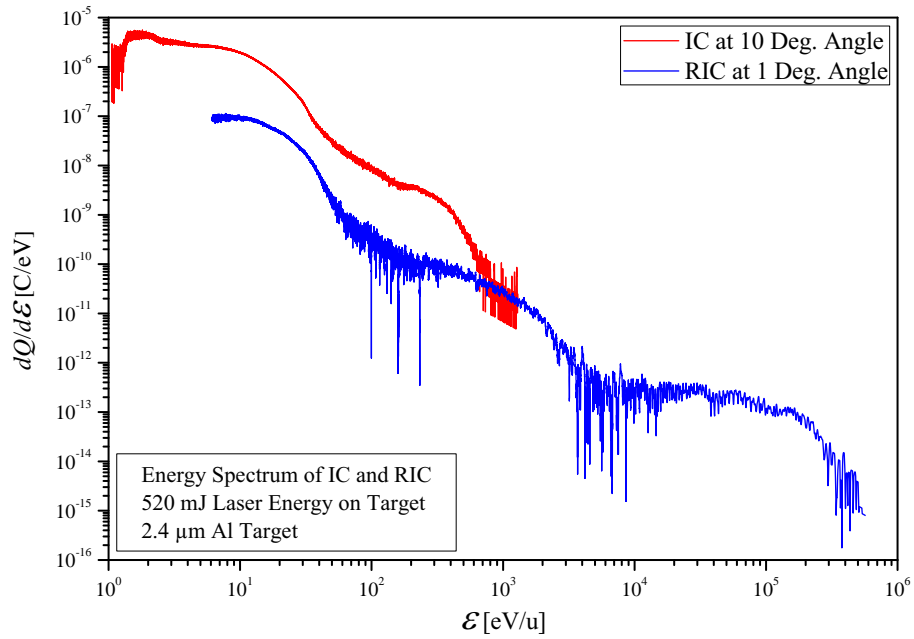


Figure 4.5: Energy spectrum of the collected charge by IC and RIC recalculated by equation (4.3) corresponding to the measurement from Figure 4.4.

The charge \tilde{Q} collected by the IC/RIC at a certain time corresponds to the number of charged particles with given charge states which are collected by the detector (if we neglect the secondary electron emission at the metallic collector surface):

$$\tilde{Q} = \sum_i q_i N_i \quad (4.1)$$

where N_i is the number of particles having charge q_i . The voltage amplitude U caused by this charge impact is measured by a fast oscilloscope and the current I coming from the collector depends on the resistors used in the electronic circuits and their total resistivity R (including termination on the oscilloscope):

$$U = \frac{I}{R} \quad (4.2)$$

Since the current is the time derivative of the collected charge we can obtain the following formula for the charge energy spectrum (see the derivation in Appendix D):

$$\frac{dQ}{d\mathcal{E} [\text{eV}]} = \frac{1}{T} \cdot \frac{U [\text{V}]}{2R [\Omega]} \cdot t [\text{s}] \cdot \frac{\Omega_{\text{BEAM}} [\text{sr}]}{\Omega_{\text{DETECTOR}} [\text{sr}]} \quad (4.3)$$

where \mathcal{E} is the energy of impinging particles at certain time t , T is the transmission of the grid applied in front of the collector (see Figure 3.7 or 3.8). Equation (4.3) is not taken only to the real solid angle of the detector Ω_{DETECTOR} but it is scaled to the solid angle of the ion beam Ω_{BEAM} measured by a RCF film. Such recalculated result neglecting the photo-peak signal can be seen in Figure 4.5.

Figure 4.5 shows a good agreement of both curves for lower energies. Unfortunately, since the IC was placed close to the target it is not possible to say if there are faster particles than depicted in the recalculated plot because of the overlapping between the fast ion peak and the photo-peak in the TOF spectrum. Moreover, there is a disagreement in the detected charge for low energy ions which can be caused by the different observation angle of the detectors.

It is not easy to detect ions with energies higher than few hundreds keV/u by using the Faraday cups since the number of fast ions is relatively low. For this reason the SiC detector has been used. The specific properties and advantages of such a type of detector are described in Section 3.3. Since the SiC detector was placed along the target normal axis at a longer distance than other used diagnostics and thanks to its fast response there is a significant separation of the fast protons/ions from the plasma photo-peak. The distance of the SiC detector from the target was 147 cm and the detection area 5 mm². It was covered by an aluminium foil of 3.2 μm thickness in order to cut part of the photo-peak and stop the slow ions.

The typical spectrum obtained by the SiC diagnostics is depicted in Figure 4.6. During our measurement, we varied the laser energy to see a difference in the maximum proton energies. The energy of the Ti:Sapphire laser beam was changed by varying the energy of the pump lasers. We were able to measure the total energy before the compressor and we calculated all losses due to the compressor gratings and all mirrors in the laser beam path. The delivered energy on-target corresponds to about 65% of the energy measured before the pulse compression.

Figures 4.6 and 4.8 show measured spectra for the lowest laser energy (423 mJ) and highest laser energy (650 mJ) on target used in the experiment, respectively. The spectra consist of a photo-peak and a peak corresponding to the contribution of protons. Evidently the photo-peak overlaps with the fast proton signal and thus information about the fastest particle contribution has to be recovered by fitting the proton signal with the following Boltzmann-like TOF distribution function, reported in literature [42]:

$$U(t) = \frac{AL}{Rt^5} \exp \left[-\frac{m_i}{2k_B T} \left(\frac{L}{t} - V \right)^2 \right] \quad (4.4)$$

where $U(t)$ is the measured voltage by an oscilloscope, R is the total resistivity of the detector circuit (including termination on the oscilloscope), A is the normalization constant, L is the distance between the target and the detector, m_i is the ion (proton in our case) mass, k_B is the Boltzmann constant, T is the ion temperature, t is the time measured by TOF signal and V is the ion shift velocity².

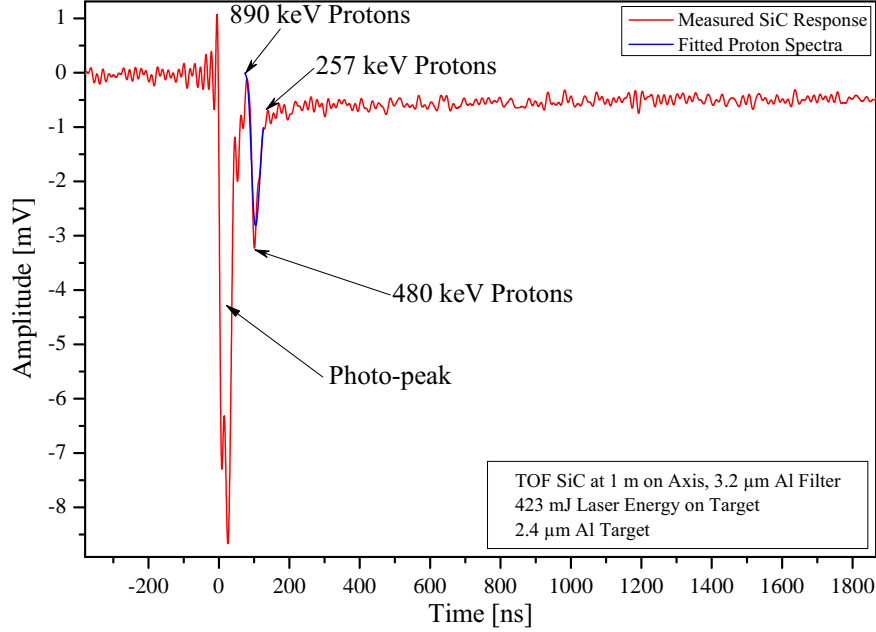


Figure 4.6: TOF spectra obtained with 423 mJ laser energy on target and measured by the SiC detector. The proton signal was fitted by the Boltzmann-like distribution reported in equation (4.4).

The TOF spectrum measured with the on-axis SiC detector at the laser energy of 423 mJ is reported in Figure 4.6. The fit of the experimental data pointed out a maximum proton energy of about 890 keV. Since the number of particles with the highest energy hitting the detector sensitive area was very low, the use of the SiC device was crucial in such a measurement. In order to know the exact number of protons impinging onto the SiC detector, it is necessary to know its response to the different proton energies. From a calibration of this detector performed by a standard X-ray source, the detected charge Q results in linear proportionality with the number of particles N and their kinetic energy \mathcal{E} as:

$$Q = \frac{eN\mathcal{E}}{\mathcal{E}_G} \quad (4.5)$$

where e is the elementary charge and \mathcal{E}_G is the minimal energy needed to create the electron-hole pair inside the semiconductor active zone (7.8 eV in case of SiC detector used during our measurement), and \mathcal{E} is the kinetic energy of the particle which is entirely

²This is an additional component due to the ion stream centre of mass velocity.

deposited in the detector sensitive layer. The energy distribution can be then obtained from the first derivative (see Appendix D) of equation (4.5) resulting in:

$$\frac{dN}{d\mathcal{E} [\text{eV}]} = \frac{\mathcal{E}_G [\text{eV}] U(t) [\text{V}]}{e [\text{C}] R [\Omega] \mathcal{E}^2 [\text{eV}]} \left(-\frac{1}{2}t [\text{s}] - \delta t [\text{s}] \right) \frac{\Omega_{\text{BEAM}} [\text{sr}]}{\Omega_{\text{DETECTOR}} [\text{sr}]} \quad (4.6)$$

where e is the elementary charge, $U(t)$ is the measured voltage (in our electrical configuration the SiC detector gives a negative voltage signal at the output) at a given time t determining also the kinetic energy of the particle given by equation (3.2) (where the velocity is given by equation (3.10)), R is the total resistivity of the detector circuit (including termination on the oscilloscope) and δt is the lowest time step of the oscilloscope which is usually much lower than TOF and thus can be neglected by using fast scopes (i.e. oscilloscope recording several giga-samples per second).

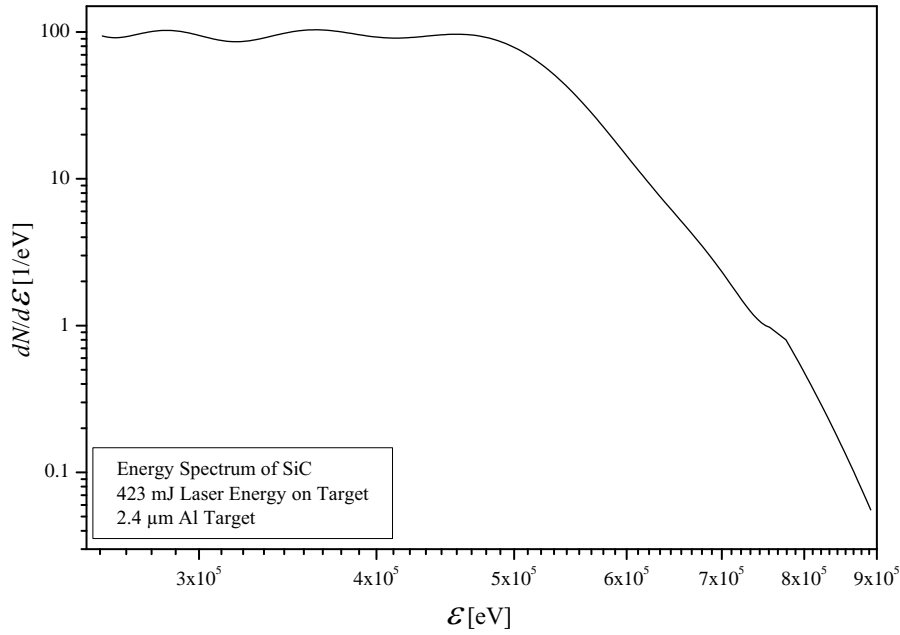


Figure 4.7: Energy spectrum of the particles impinging on the SiC detector recalculated by equation (4.6) corresponding to the TOF signal plotted in Figure 4.6.

Figure 4.7 reports the proton energy distribution recalculated from the measured TOF spectrum of Figure 4.6 by using equation (4.6).

The spectra obtained at progressively increasing laser energy have shown an increase in the maximum proton energy, as expected. Figure 4.8 reports the TOF distribution of the shot with the highest laser energy showing a measured proton peak energy of about 1.4 MeV and a maximum proton energy of 2.7 MeV. The same fit procedure has been performed also in this case, and the corresponding energy distribution is depicted in Figure 4.9.

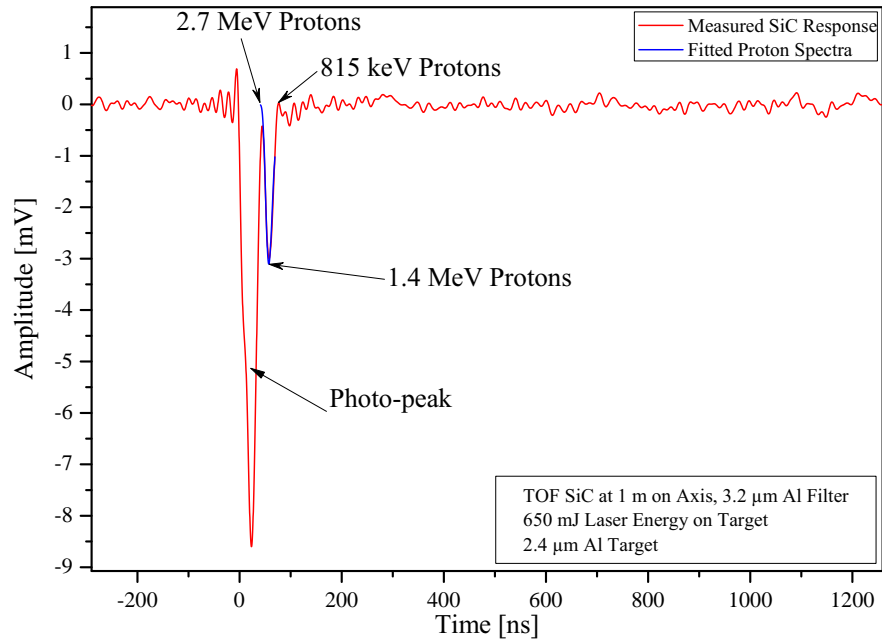


Figure 4.8: Measured TOF spectrum obtained with 650 mJ laser energy on target and measured by the SiC detector.

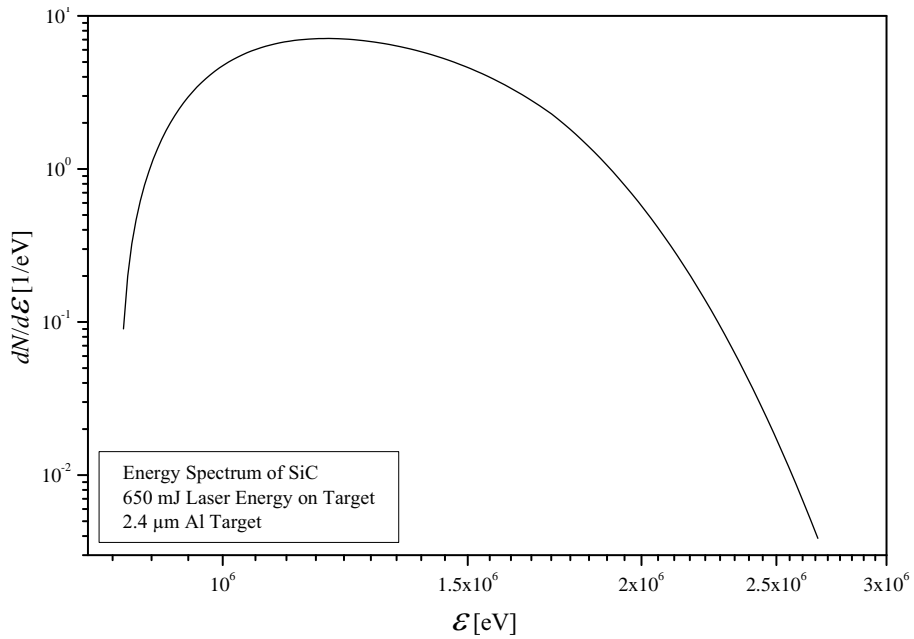


Figure 4.9: Energy spectrum of the particles impinging the SiC detector recalculated by equation (4.6) corresponding to the TOF signal plotted in Figure 4.8.

4.3 Results from 100 TW Ti:Sapphire Laser at APRI-GIST in Korea

A further experiment was performed at the Advanced Photonic Research Institute (APRI)-Ultrashort Quantum Beam Facility in Gwangju, Korean Republic. It was mainly focused on using the advanced (sub-micron structured) targets aimed to increase the laser absorption at the front side and, as a consequence, enhance the energy and total number of accelerated protons in a regime of genuine TNSA. Hence the ion detection system was crucial for the full characterization of the experimental results. It was composed of TOF and TP diagnostic systems. Properties of the laser system are reported in Table 2.3. This section is mainly focused on the evaluation of TP experimental data.

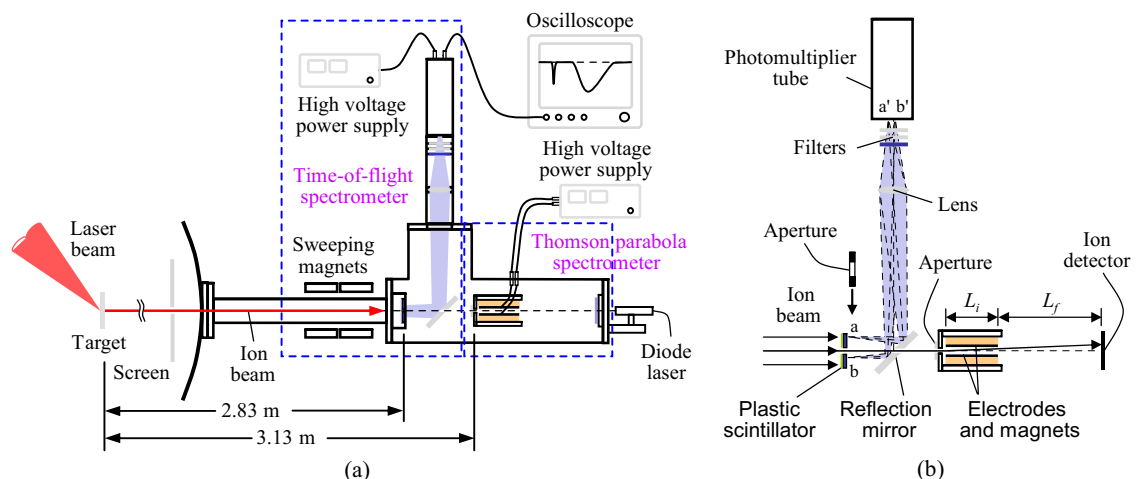


Figure 4.10: TOF and TP diagnostics employed for simultaneous measurement at APRI-GIST [31].

The TOF system at APRI-GIST is composed of a plastic scintillator (BC-408, BICRON, Saint-Gobain Ceramics & Plastics Inc.) which responds directly to the impinging energetic ions by the fluorescence light emitted with a fast rise time (0.9 ns) [31]. This scintillator is thick enough to stop all protons with energies below 11 MeV which was sufficient for our measurements. The plastic scintillator is also sensitive to the UV light and X-rays coming from plasma. In order to cut the visible light, the 210 nm aluminium foil is applied on its surface. The fluorescence light from the plastic scintillator is reflected by a flat mirror and then amplified inside a photomultiplier tube (with a fast rise time of 0.7 ns [31]) and its output voltage signal is measured by a fast oscilloscope. Double dipole magnets are placed in front of the TOF system to create a chicane to deflect low energy particles (especially co-moving electrons which could overlap with the fast ion signal) from the detector. In principle electrons with energies below 2 MeV are efficiently deflected away from the detection area of the plastic scintillator. Since the rise time of the plastic scintillator and photomultiplier tube is fast enough it is possible to assume that the distance of the TOF diagnostics is corresponding to the one of the plastic scintillator placed at 2.83 m from target.

The plastic scintillator has a hole in the middle to allow a part of the particle beam to pass through it and reach the TP. The spectrometer is placed in the distance of 3.13 m from target by a tungsten aperture of 0.3 mm diameter. The sector where the electric and magnetic field is present (as depicted in Figure 4.10) has the field length of $L_i = 0.1$ m,

the field free region starts by the end of the permanent magnets and capacitor plates and ends at MCP plane, this length is $L_f = 0.219$ m. The capacitors gap is set to 1 cm and the application of the voltage of 3.5 kV results in the electric field of 0.35 MV/m. The magnetic field of the used permanent magnet is about 0.2 T.

The typical MCP applied voltage is about -0.9 kV, this value is set to prevent the MCP working in a saturation regime and to amplify the signal coming mainly from positively charged ions. The phosphor screen placed behind the MCP is positively biased to attract electrons produced and amplified by the MCP. The visible signal is then collected by an ICCD³ camera (512×512 pixels) as depicted in Figure 3.4. The real dimension seen by one pixel of the ICCD is calibrated by a rule placed on the phosphor screen.

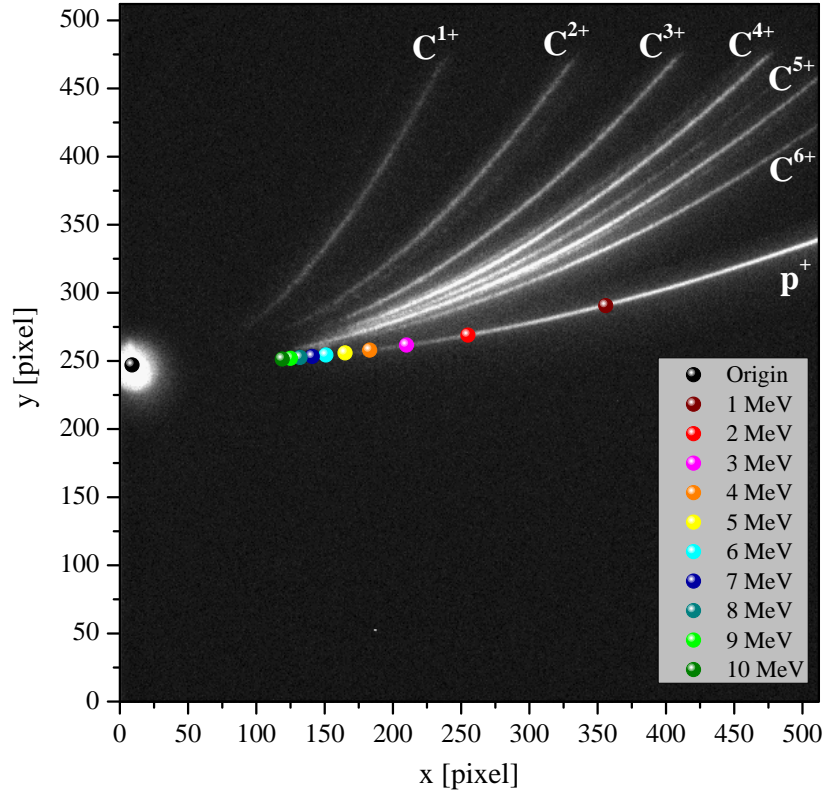


Figure 4.11: Measured TP spectra with depicted energies on the proton parabola.

³The intensified CCD camera is a high sensitivity device capable of the single photon detection. It is the charge-coupled device (CCD) which is optically connected to an image intensifier mounted in front of CCD. The image intensifier includes three functional elements: a photocathode, MCP and a phosphor screen. Once a photon reaches the photocathode, the photoelectron is generated. Photoelectrons are accelerated toward the MCP by a controlled electrical voltage and they are multiplied inside the MCP and further accelerated to the phosphor screen. The phosphor screen convert electrons back to the visible light which is registered by the CCD camera. If the voltage between photocathode and MCP is reversed, electrons are repulsed from MCP and no signal will be registered by CCD. This voltage reversion process is called gating and it helps to select incoming light intensity information between specific time intervals.

The vertex of all parabolas drawn on the MCP by the impinging particles is established by the plasma X-ray spot causing photoemission in the MCP and thus a visible signal. In fact, the plasma X-rays are not deviated by the applied electric and magnetic fields and thus it is possible to find the centre of the X-ray spot from each measurement. The parabola vertex is labelled as “origin” point in Figure 4.11.

To measure the particle energy is necessary to rewrite equation (3.5) in a form applicable to the real parameters including the dimension calibration of the ICCD. We know that x and y positions are connected through the new equations. Finally, it is necessary to calculate the intensity profile along the experimental parabolas where x and y position give us the velocity from the equation (3.6), and from the velocity it is possible to calculate the particles energy distribution (equation (3.2)) and the corresponding TOF spectra at any distance (from equation (3.10)). The noise level of the ICCD camera is taken every shot from the area where no particles or X-rays are present, e.g. below the proton parabola in Figure 4.11. Then it is necessary to perform an arithmetic mean of the intensity without particles along with its standard deviation. The maximum energy is taken from the parabola intensity profile as the first point lower than the average intensity plus its standard deviation.

A comparison between a TOF measurement recalculated at 1 m detection distance and the simultaneous TP measurement (converted to TOF at 1 m) is shown in Figure 4.12. The intensity profile of the TP is different from the measured TOF diagnostics because TP system (i.e. MCP, phosphor screen and ICCD response) had not an absolute calibration. Thus it is possible to perform only a temporal comparison of the two signals. It can be clearly seen that the beginning of the TOF and TP spectra are in good agreement and there is a little delay of about 4 ns between them. This can be mainly due to their different detection solid angles as the TP is perfectly aligned on axis and the TOF scintillator has a hole in its centre to allow part of the ion stream to pass through (ions with highest energies are supposed to be localised on axis).

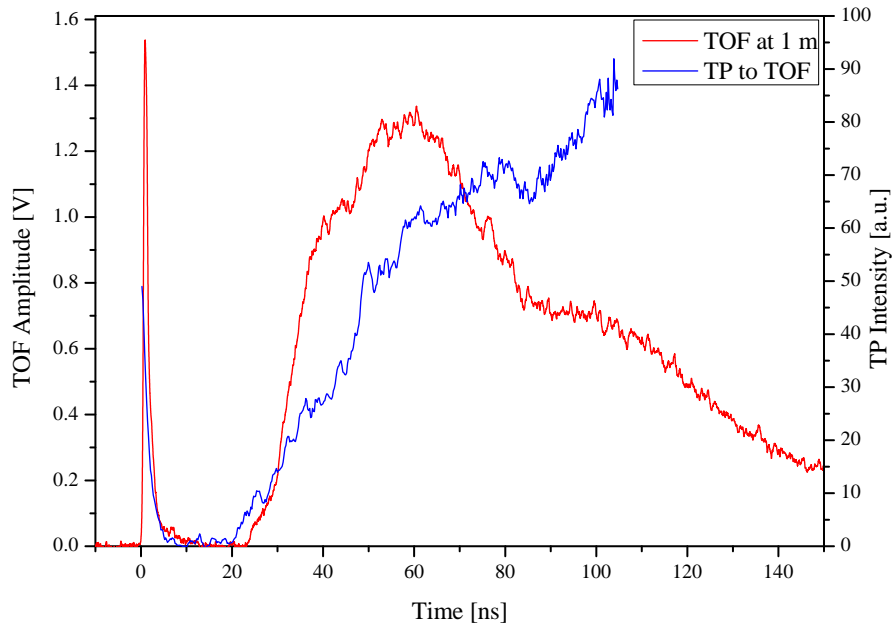


Figure 4.12: Comparison between the simultaneous measured TOF signal and TP signal both recalculated in TOF configuration at 1 m detection distance.

As was mentioned above the main aim our experimental campaign was to enhance the laser absorption by using structured targets on the front side. The general geometry of such targets was a regular grid made of nanospheres grown on the front side of the 900 nm Mylar foil (different sphere diameters for each target foil have been tested). The choice to use this type of targets was done according to particle-in-cell simulations performed by the theoretical group leaded by Prof. Limpouch at Czech Technical University [43].

The results were taken in two experimental configurations. The first one is denoted as “bad contrast” where the nanosecond pedestal of the laser beam was not well known and was not the optimal needed for the target constraints (mainly due to damaging effect on the nanospheres). The second one is denoted as “good contrast” where the laser pedestal was tuned to the best conditions reaching the value noted in Table 2.3.

The results from the “bad contrast” reported in Figure 4.13 do not show any significant changes in the proton energies and in the total energies for each sphere diameter. This means that when a non-negligible pre-pulse is present, it destroys the sphere structure on the target front side and thus the effect of nanospheres is negligible.

The results from the “good contrast” reported in Figure 4.14 show an energy dependence on the sphere diameter as the pre-pulse is negligible and does not destroy the sphere structure. The results show a significant increase of the total proton energy of about three times for 535 nm spheres in comparison with the pure flat foil without any structure. In comparison with other spheres diameters the 535 nm ones seems to be the most effective for the enhancement of the proton flux. Unfortunately due to the missing calibration of the TP system, it is not possible to give an absolute estimation of the total proton beam energy.

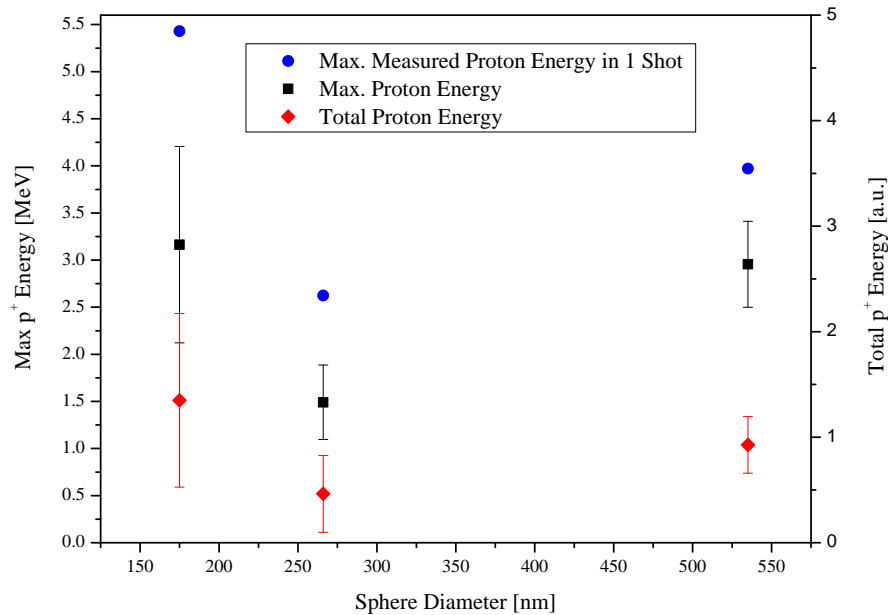


Figure 4.13: Maximum measured proton energy and total proton energy for different target geometries (175 nm, 266 nm and 535 nm sphere diameters) in the same experimental conditions in the “bad contrast” regime.

The data processing is still in progress and the full results including the TOF measurements will be published in the near future.

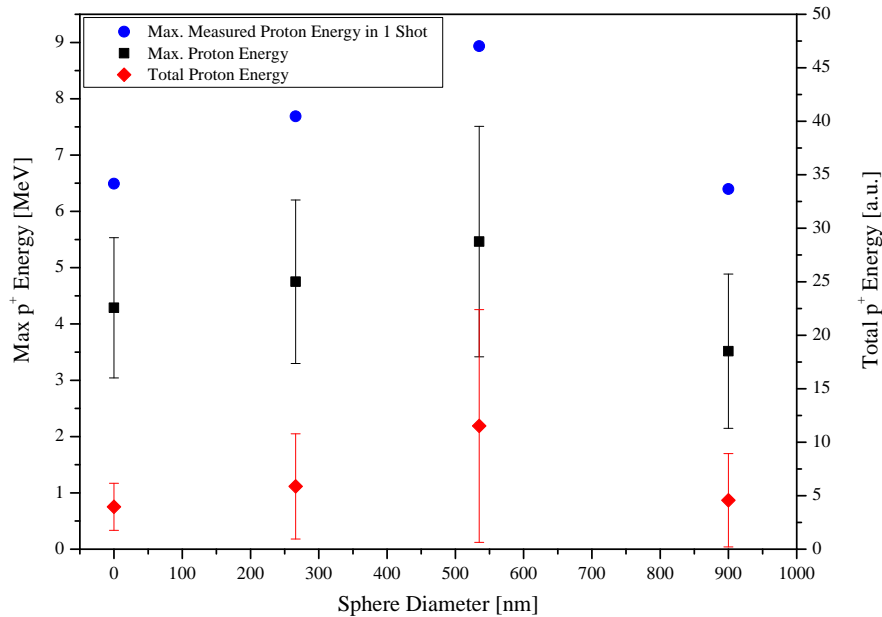


Figure 4.14: Maximum measured proton energy and total proton energy for different target geometries (175 nm, 266 nm and 535 nm sphere diameters and pure foil without any structure) in the same experimental conditions in the “good contrast” regime.

4.4 Results from PHELIX Laser in GSI Darmstadt

The experimental campaign held at PHELIX laser in GSI Darmstadt was aimed to explore the laser accelerated proton beams as an intense high gradient injectors for the conventional acceleration. The main goal was to determine if the plasma electrons propagate as an overlapping beam with the accelerated ions. This would also determine if plasma has a single temperature or separate longitudinal and transversal temperatures. Radiochromic films have been employed in order to determine the highest proton energies and a Faraday cup array has been used for measuring the plasma electron and ion beam charge. This diagnostic tool was shown in Section 3.5 and was developed to be used inside the vacuum chamber in a harsh environment due to a huge EMP. The way to measure the longitudinal temperature consisted in the application of filters with various thicknesses through which electrons with a kinetic energy below a certain value cannot pass.

There was a big issue to protect the signal cables and the Faraday cup circuit from the huge EMP associated with the electromagnetic fields of the ultrahigh intensity laser focused onto a solid target foil (the vacuum chamber is acting as an “antenna”) thus the EMP shielding assessment has been built (as shown in Figure 4.15). The collector circuit was put inside the metallic support structure and winded by the aluminium foil. Also the output signal cables coming to the oscilloscope were set inside bellows winded by an aluminium foil and oscilloscopes were placed inside a copper Faraday cage. The power supply for the collector circuit has been also kept out of EMP inside its Faraday cage.

The cups were placed first in a distance of 60 cm from the target and then close (about 20 cm) to the target at various angles as it can be seen right down in Figure 4.15. Collimators of 2 mm diameters were put inside the Faraday cage holes. The laser was focused on 10 μm gold target in TNSA scheme. The typical FC outputs signal is depicted in Figure 4.16.

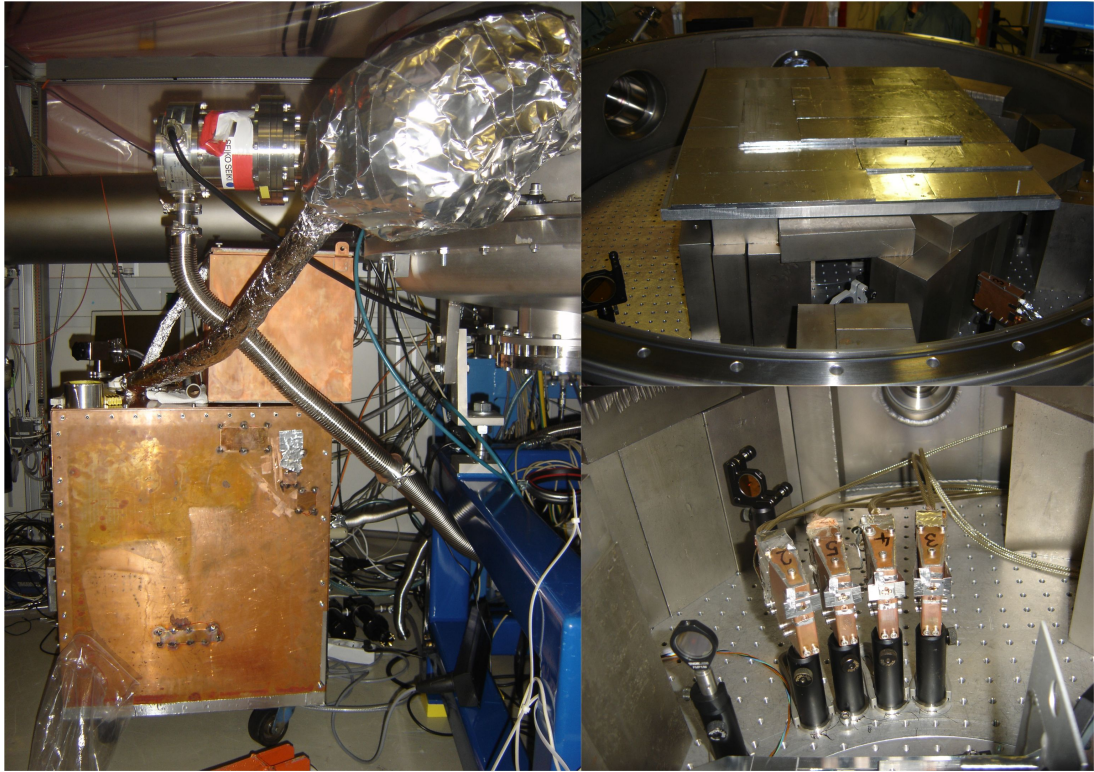


Figure 4.15: Experimental setup: right top is the collector placed behind the lead shielding, right down is the array of eight Faraday cups looking at the target, on the left is the outside where the circuit is attached to chamber coated by several layers of aluminium foil shielding also the cables inside the bellows coming into the Faraday cage with oscilloscopes inside.

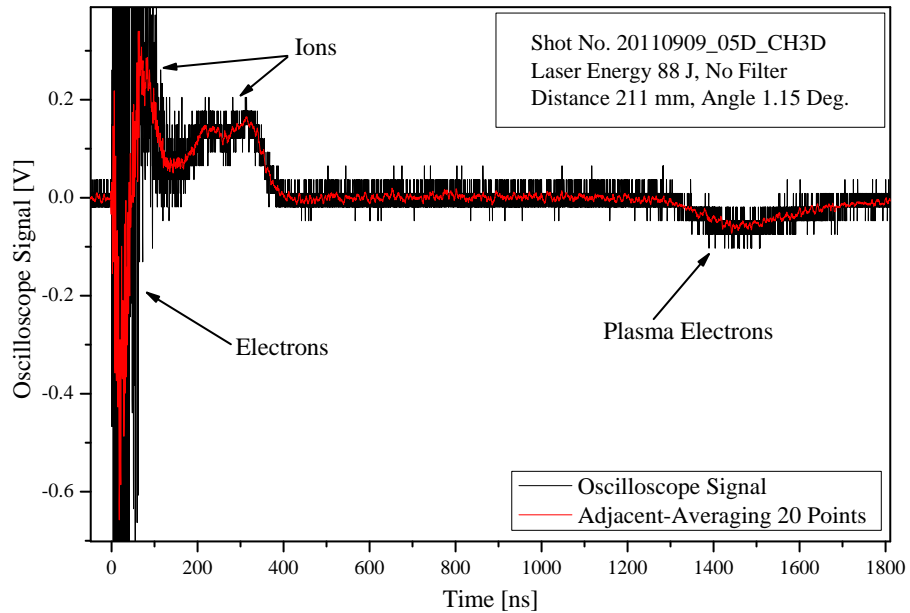


Figure 4.16: TOF spectrum measured by the developed Faraday cup.

The circuit of the Faraday cup was designed to be able to handle a signal of several hundred volts. The oscilloscope needed to be protected, thus attenuators were put in front of the oscilloscope termination. The real signal was attenuated 10 times in comparison with the original one. 1 M Ω termination was used in order to protect the oscilloscope. From the original recorded spectra reported in Figure 4.16, we can clearly distinguish a structured proton/ion signal (positive polarity) and also the contribution of the slow plasma electrons (negative polarity). The main problem was to recognize other particles contribution overlapping with the EMP noise.

Fortunately it is possible to perform a simple data processing procedure called adjacent-averaging over a certain number of a data points. We showed in our measurement that the EMP signal on the detector is bipolar and when this signal is averaged over several points it gives us a zero contribution to the collected charge. This was demonstrated with the Faraday cup placed behind the lead shielding, as shown in Figure 4.17. It is also important to know the EMP contribution on the collector circuit itself, on the signal cables, and also on the oscilloscope which is placed inside the Faraday cage. This was also measured and from the plot reported in Figure 4.17 it is evident that the measured signal (when no particles are supposed to be detected) comes only from the genuine EMP. Applying the adjacent-averaging we can see that the EMP has a bipolar response and thus in average it does not add any net signal to the measured particle charge.

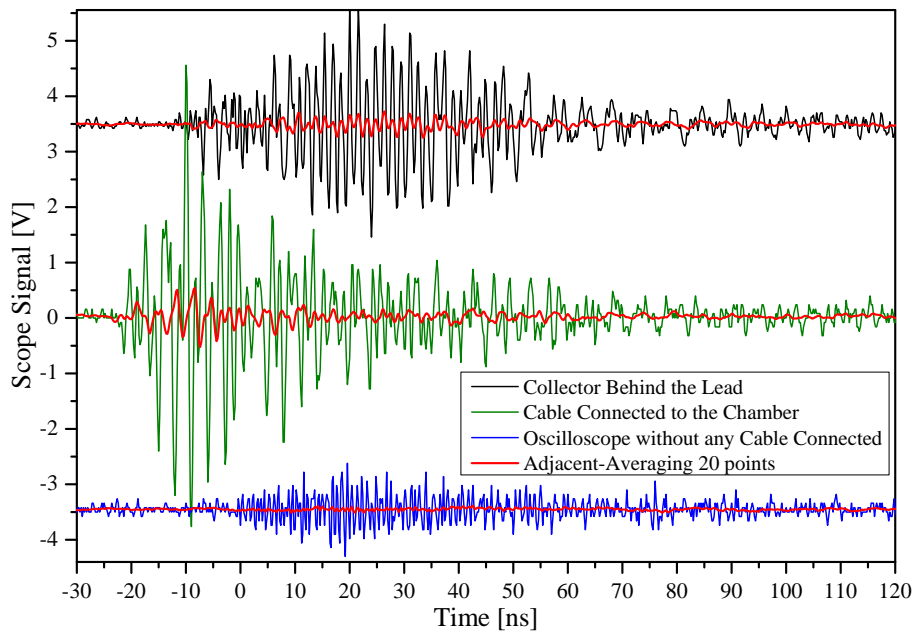


Figure 4.17: TOF spectrum from measurement of the collector placed behind the lead bricks inside the chamber, only the cable connected to the chamber’s flange and the oscilloscope placed inside a Faraday cage out of the chamber, and their averaged signals.

From the signals shown in Figure 4.17, the EMP in the oscilloscope channel (where no cable is plugged) looks very high. A very low signal is expected, since the oscilloscope is placed inside a closed Faraday cage. This might indicate that the EMP is transferred inside the Faraday cage, or the channels of the oscilloscope are influencing each other through ground. However, the results shown in Figure 4.17 demonstrate that the use of the averaging method is correct to get a “useful” signal from the EMP noise.

When the averaging method is vindicated we can closer have a look at plot in Fig-

ure 4.16. Using adjacent-averaging over 20 points we can clearly distinguish a contribution of electrons at the beginning of the signal. Those electrons causing negative signal are coming before the first group of fast protons followed by the group of heavier ions. Using an oscilloscope with a resolution of 5 Gigasamples/s and using averaging over 20 points, we know that sharp signals lower than 4 ns are very distorted and basically not detectable. This is, in principle, the limit over which we are not able to go at the moment. The other issue is the temporal dispersion of signal during the transmission from the Faraday cup electrode which according to Appendix C is about 2 ns. In principle, the temporal dispersion could not be caused only by the ion collector structure, but also by electronic circuit depicted in Figure 3.8, this issue should be also taken into account in future.

The Fourier transform of the signals reported in Figure 4.17 shows us the main contributions of the EMP in a frequency domain. The collector main frequency peaks are at 188 MHz, 260 MHz, 397 MHz, 640 MHz, 1 GHz and 1.1 GHz. The signal from cables which were connected to the chamber from the outside but without any detector or cable plugged from the inside of the vacuum chamber is shown as red in Figure 4.17. For this measurement, a low amount of data points was accidentally taken and thus we are not able to say that there are additional frequency spikes than for measurement with collector behind the lead shielding (collector has also cables connected to the chamber but on the vacuum side has other cable continuing into the Faraday cup) but basically the frequency peaks are matching with the collector ones. On the oscilloscope there is only one significant peak at a frequency of about 1.1 GHz.

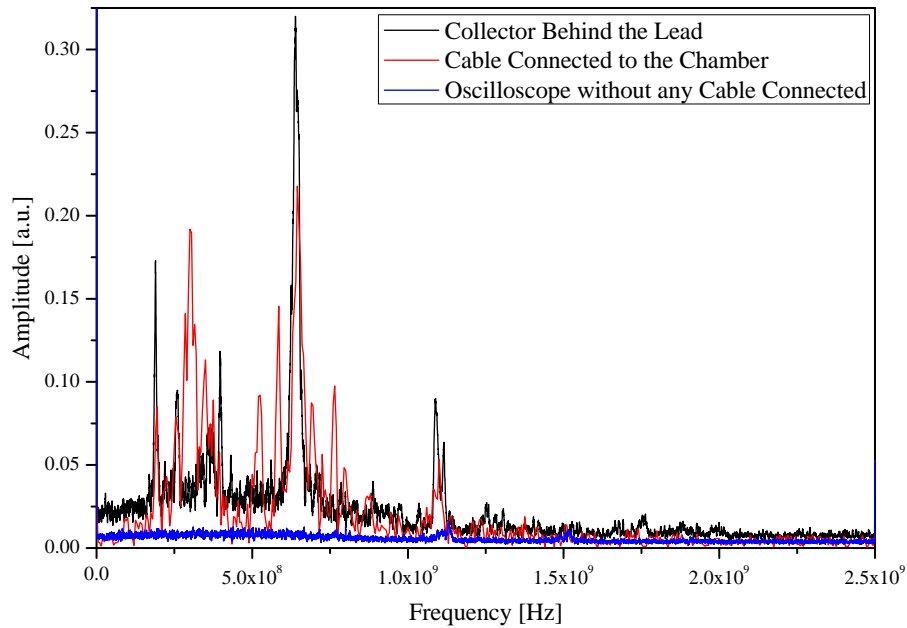


Figure 4.18: Fourier transform of the measured signal from Figure 4.17.

The experimental campaign at PHELIX laser was accompanied by some technical difficulties with cooling of the laser system resulting in only two successful shots at the end of the campaign. For this reason we did not rigorously tested the idea of applying filters in order to see if electrons longitudinal temperature is high enough to penetrate through various filter thicknesses. However, we have tested our new diagnostics system and found out that it is possible to work in real-time and TOF configuration at extreme conditions carried by the huge EMP noise. These Faraday cups can be also used to measure

the frequency domain of the EMP as demonstrated in Figure 4.18.

From the experiences yielded during this experimental campaign, we can approach to the further upgrade of the ion collectors used. First, the cables coming from the Faraday cup cathode into the BNC socket must be shorten. The longer wires the higher noise is generated on them. The best solution should be cutting the wires coming from electrodes to BNC as much as possible or even better to attach the electrodes directly onto the BNC socket. In connection with the shortening of cables, the mural support should be also optimized. Other challenge is to develop a better and faster alignment of the Faraday cups in order to not only make things faster, but also for blinding the holes for laser alignment when the target is aligned and can be moved during blinding procedure. We should also make a better closing of the Faraday cage around the detector, especially at the back where triaxial signal cables comes out from its cage. It is possible to play also with the dimension of the Faraday cup in order to reach the impedance of 50Ω . From equation (3.19) we can calculate the ratio 3.29 between outer and inner electrode diameter (using the Teflon insulator in order to reach the 50Ω impedance). If we fix the diameter of the inner electrode (3.5 mm), the outer electrode would have a diameter of 11.5 mm (this dimension change would also influence the cutoff frequency which would then be lower at 8.5 GHz, and thus the rise time of the detector would be changed as well).

Concerning the Faraday cages, we have to build a compact one for shielding the collector circuit which is placed outside the vacuum chamber. It is also necessary to solve the problem of the Faraday cage hiding collectors inside. As seen from the left part of Figure 4.15, the cage is closed by tens of screws and, before each shot, they have to be tightened and after each shot loosen in order to reach the oscilloscope and save the signal (if this is not possible to do remotely and thus no opening and closing of the cage would be needed). During the measurement we have also some triggering issues and we found out that the best was to trigger directly by the signal coming from plasma radiation impacting on the detector.

After a proper data analysis we found out that due to the averaging procedure of the measured signal by the ion collector we need higher sampling of the oscilloscope. Finally, we could measure the rise time of our Faraday cup e.g. by a laser accelerated quasi-monoenergetic electron bunch produced by laser-plasma wakefield acceleration. Such electron bunch duration should be the same as the laser pulse duration and thus we could be able to see a steep increase of the signal when they hit the Faraday cup.

Such an advanced diagnostic system might be employed in future at the Ti:Sapphire laser at PALS since we are interested in measuring the plasma electron-ion de-coupling (plasma quasi-neutrality), where much smaller EMP is expected and thus the observational conditions should be more convenient than in the case of the energetic laser pulses present at PHELIX system.

Conclusions and Perspectives

The goal of this thesis work was to test various proton/ion diagnostics (Faraday cup, SiC, ion collectors and Thomson parabola) for the characterization of laser accelerated ion beams in various experimental conditions. These experiments were performed both at local facility (PALS - kJ laser beamline and Ti:Sapphire fs laser beamline) and abroad (GIST laboratory in the Korean Republic and GSI facility in Germany).

The first experimental campaign on proton/ion acceleration was carried out at Ti:Sapphire fs-laser at PALS. The TOF diagnostics employed during the experiment consisted of a SiC detector and few ion collectors in a ring configuration placed far from the target, and an emission-less Faraday cup placed close to the target. This experiment showed a good agreement of the energy spectra obtained by different types of ion collectors placed at different angles and different distances.

The Thomson parabola diagnostic tool was tested during the experimental campaign at the kJ beamline of PALS and a routine procedure for handling a large amount of data from the Thomson parabola acquisition system was done for the experimental campaign held in APRI-GIST. This experiment was mainly focused on tests of advanced (sub-micron structured) targets aimed to increase the energy and total number of accelerated protons. The data from the Thomson parabola were analysed in this work and they showed the correspondence of the Thomson parabola measurement with the TOF diagnostics.

The experiments at the Ti:Sapphire laser at PALS suggested a further development of the ion collectors. In fact, an array of these detectors was tested at the PHELIX facility in GSI in presence of a strong electromagnetic pulse. It was demonstrated that the electromagnetic pulse background can be suppressed by a data averaging method in the measured spectra. Thus it enables to distinguish the contribution of the electrons at the beginning of the signal. This experimental campaign revealed the need of a further upgrade of the ion collectors. At first, the wires coming from the electrodes to the BNC socket have to be shortened as much as possible or the electrodes have to be bonded directly onto the BNC socket. Second, the dimensions of the Faraday cup have to be adjusted to reach the correct impedance matching of 50Ω . The other step should be to develop a more precise and faster alignment system for the ion collectors. The main challenge is to protect the signal from the electromagnetic pulse along its entire path to the measuring device. These upgraded diagnostic tools will be tested in the future experiments at kJ and fs beamline at PALS.

Appendix A

Scheme of the Ti:Sapphire Laser System at PALS

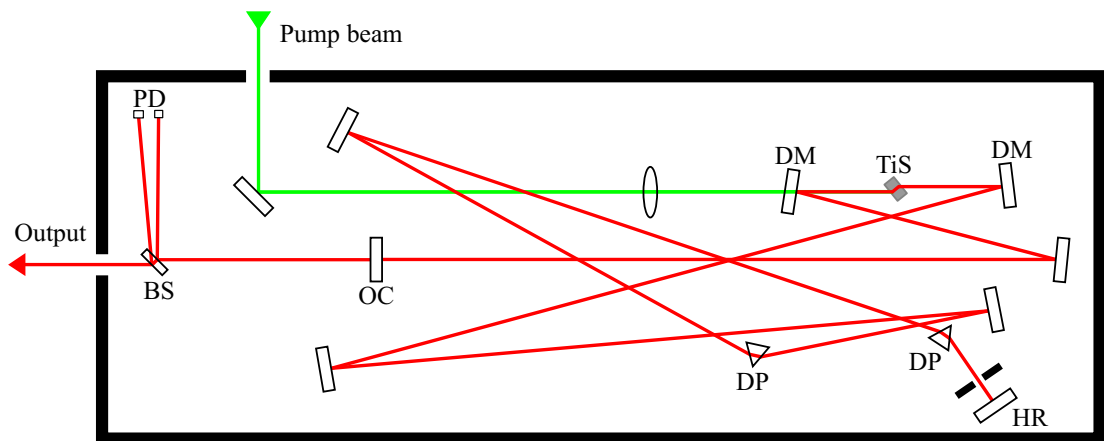


Figure A.1: Oscillator: DM - dichroic mirror; TiS - titanium sapphire laser crystal; DP - dispersive prism; HR - high reflective (100%) mirror; OC - output coupler; BS - beam splitter; PD - photo diode.

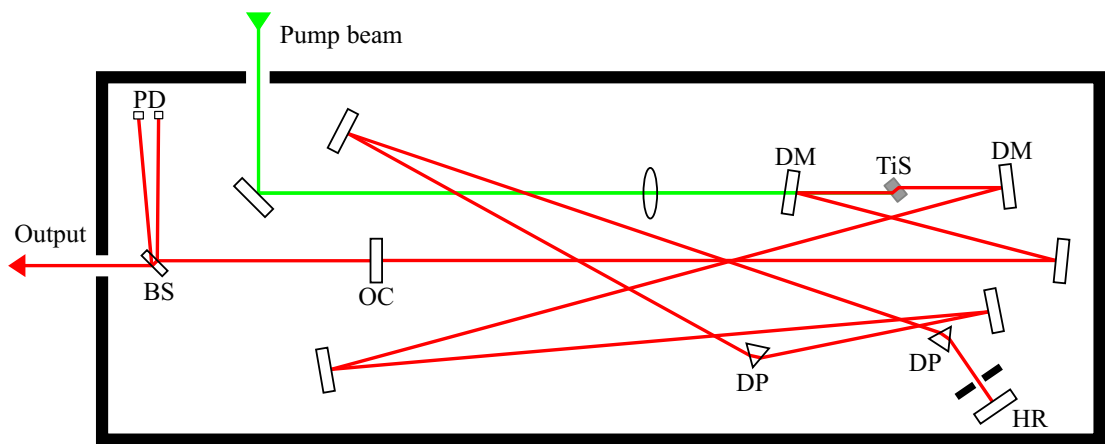


Figure A.2: Regenerative amplifier of the Ti:Sapphire laser: Pol. - Polarizer; DG - dispersive grid; PM - parabolic mirror; FM - flat mirror; Per. - periscope; TiS - titanium sapphire laser crystal; PC# - pockels cell; QWP - quarter-wave plate; CM - cavity mirror; PD - Photo diode; LD - laser diode.

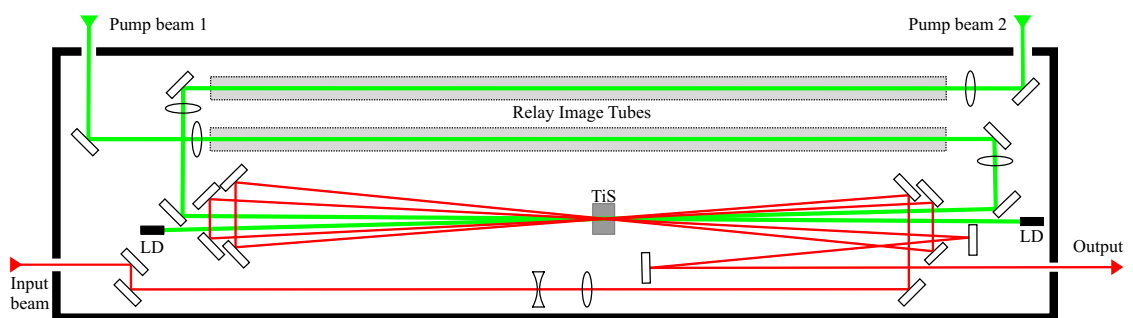


Figure A.3: Multipass power amplifier: TiS - titanium sapphire laser crystal; LD - laser diode.

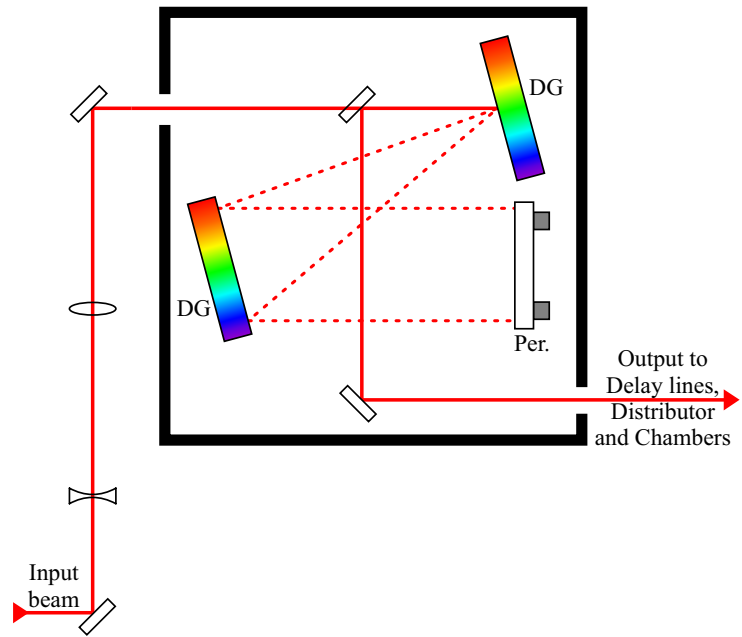


Figure A.4: Compressor: DG - dispersive grid; Per. - periscope.

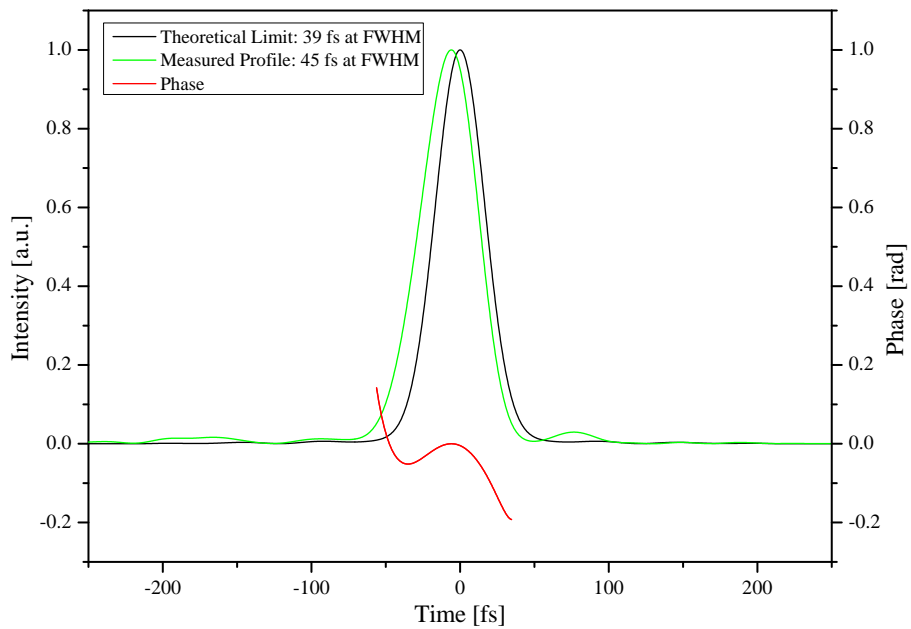


Figure A.5: Temporal profile of the laser beam pulse and comparison with the theoretical limit behind a small compressor measured by the SPIDER diagnostics.

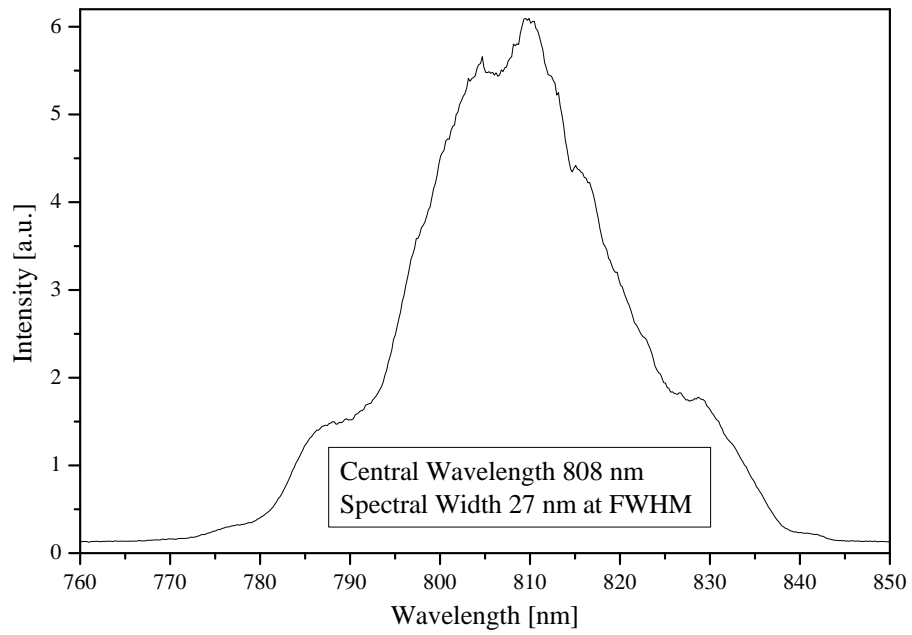


Figure A.6: Wavelength spectrum with a central wavelength at 808 nm and spectral width of 20 nm at FWHM.

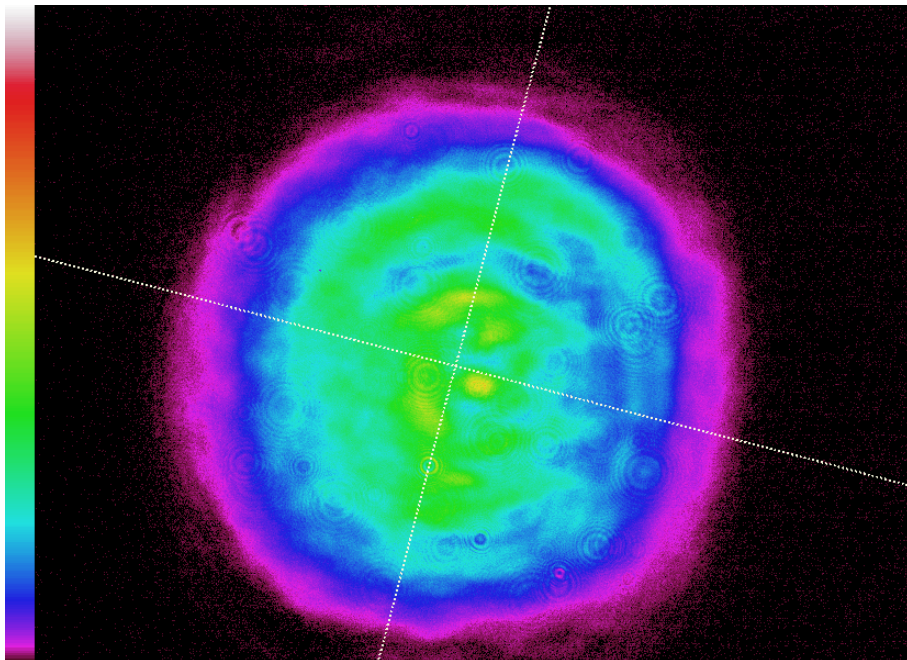


Figure A.7: Beam wavefront profile after the compressor.

Appendix B

Derivation of Parabola Equation for Thomson Parabola Spectrometer

For the derivation of the parabola equation we will refer to Figure 3.3 where the coordinate system (x, y, z) is depicted. The x coordinate presents the direction of the particle deflection due to the applied magnetic field. The y coordinate presents the direction of the particle deflection due to the applied electric field. The z coordinate represent the initial particle propagation direction through the very narrow pinhole placed out of influence range of any external field. The derivation itself has four main assumptions:

1. The particle's motion is non-relativistic.
2. The charged particle is affected by the electric and the magnetic fields only along the lengths of the devices creating those fields and its movement is caused by the Lorentz force:

$$\mathbf{F} = q(\mathbf{E} + \mathbf{v} \times \mathbf{B}) \quad (\text{B.1})$$

3. The initial conditions for initial velocity \mathbf{v} , electric field \mathbf{E} and magnetic field \mathbf{B} are:

$$\mathbf{v} = (0, 0, v); \mathbf{E} = (0, E, 0); \mathbf{B} = (0, B, 0) \quad (\text{B.2})$$

4. The Larmor radius r_L is much larger than magnet length ($r_L \gg L_{iB}$). Where the Larmor radius is given by the following equation:

$$r_L = \frac{mv}{qB} \quad (\text{B.3})$$

5. Particle does not emit any radiation when its trajectory is deviated or during acceleration in the presence of electric field.

The Lorentz force is additive with respect to the B field and E field. From Figure 3.3 it can be seen that the fields are parallel and due to the first assumption it is possible to split the Lorentz force into the electric and magnetic components. The separated field affects the particle motion only in one direction depending only on the field intensity (and particle's initial velocity), for this reason it is possible to solve it easily in 2D where one dimension is the particle initial movement (z axis) and the other dimension depends on the applied field.

Magnetic field

We will separate solving this problem into two regions shown in Figure B.1. One is the region with magnetic field generated by a magnet of length L_{iB} , where the charged particle is moving on circular trajectory with radius r_L . The consequence of the particle's circular motion is its shift of a length x_1 at the end of the magnetic field region, and continues in the field-free region deviated from its initial position by an angle α , thus the shift in this region is x_2 .

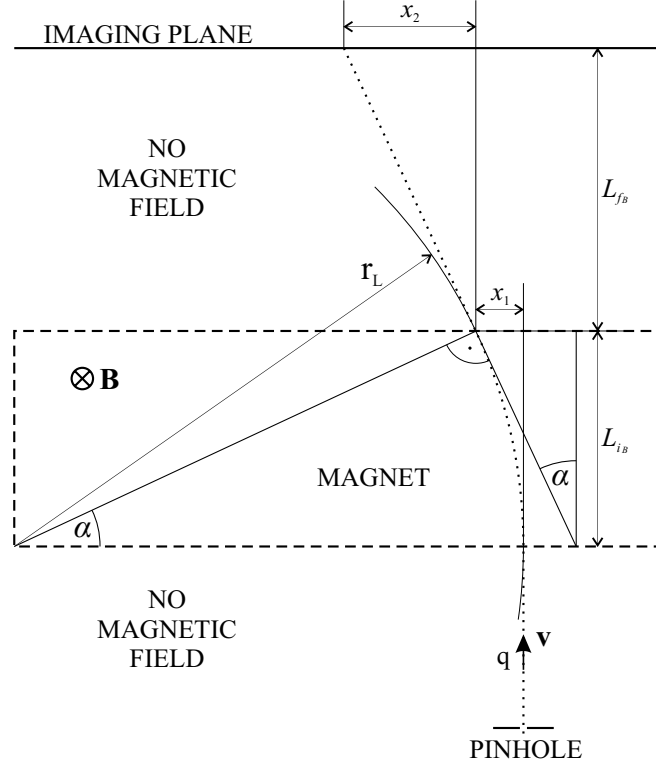


Figure B.1: Deviation of the charged particle in presence of the magnetic field and its further detection on imaging plane.

From the definition of the sin and cos function we can clearly see from the Figure B.1 that:

$$\sin \alpha = \frac{L_{iB}}{r_L} \quad (\text{B.4})$$

and therefore the lengths x_1 and x_2 are:

$$x_1 = r_L (1 - \cos \alpha); x_2 = L_{fB} \tan \alpha \quad (\text{B.5})$$

We can convert the cosine function into a known sine from equation (B.4):

$$\cos \alpha = \sqrt{1 - \sin^2 \alpha} \quad (\text{B.6})$$

For the final position on the imaging plane the lengths of the two regions have to be added resulting in:

$$x = x_1 + x_2 = r_L \left(1 - \sqrt{1 - \sin^2 \alpha} \right) + L_{fB} \tan \alpha \quad (\text{B.7})$$

In order to get rid of the square root we can perform the Taylor series and take the first nonzero component:

$$\sqrt{1 - s^2} = 1 - \frac{s^2}{2} + \mathcal{O}(s^3) \quad (\text{B.8})$$

where $s = \sin \alpha$. This step is valid because of the fourth assumption ($r_L \gg L_{i_B}$). For the same reason the angle α is so small that we can anticipate:

$$\tan \alpha \approx \sin \alpha \quad (\text{B.9})$$

Taking equation (B.7) and using equations (B.4), (B.8) and (B.9) we will obtain:

$$x = \frac{L_{i_B}}{r_L} \left(\frac{L_{i_B}}{2} + L_{f_B} \right) \quad (\text{B.10})$$

Expressing the Larmor radius from equation (B.3) the final length of the particle's transversal motion (and also the x coordinate on imaging plane):

$$x = \frac{qBL_{i_B}}{mv} \left(\frac{L_{i_B}}{2} + L_{f_B} \right) \quad (\text{B.11})$$

For the case of using the spectrometer with the magnetic field only we can approach to the relativistic formulation of the position x by just changing the fourth assumption into a relativistic form:

$$r_L = \frac{p}{qB} \quad (\text{B.12})$$

where p is the size of momentum of charged particle which is conserved in our system due to the fifth assumption (from which we can say that the velocity component perpendicular to the magnetic field is constant) and is equal to:

$$p = \gamma m_0 v \quad (\text{B.13})$$

where γ is the relativistic factor from equation (1.2). Now we are able to follow the formal procedure from the geometrical situation depicted in Figure B.1 arriving to equation:

$$x = \frac{qBL_{i_B}}{\gamma m_0 v} \left(\frac{L_{i_B}}{2} + L_{f_B} \right) \quad (\text{B.14})$$

From equation (B.14) and (1.2) we are able to derive the velocity as a function of coordinate x on imaging plane:

$$v = \frac{cqBL_{i_B} \left(\frac{L_{i_B}}{2} + L_{f_B} \right)}{m_0 x \sqrt{c^2 + \left[\frac{qBL_{i_B}}{m_0 x} \left(\frac{L_{i_B}}{2} + L_{f_B} \right) \right]^2}} \quad (\text{B.15})$$

Substituting velocity from equation (B.15) into the equation (3.11) we get the relativistic energy of detected particle at a coordinate x on imaging plane. Such a magnetic spectrometer is useful especially when measuring electrons, where we do not have to recognize the different charge states and masses of particles, this kind of spectrometer is used for detection laser-plasma accelerated electrons.

Electric field

As in case of magnetic field we will separate the solution of this problem into two regions as shown in Figure B.2. One is the region with the electric field on the capacitors length L_{iE} where the charged particle gets the shift of a length y_1 , and continues in the field-free region with an angle of β made by the present trajectory with the movement, thus the shift in this region is y_2 . Adding these two parts together we obtain:

$$y = y_1 + y_2 \quad (\text{B.16})$$

where y is the final position on an imaging plane.

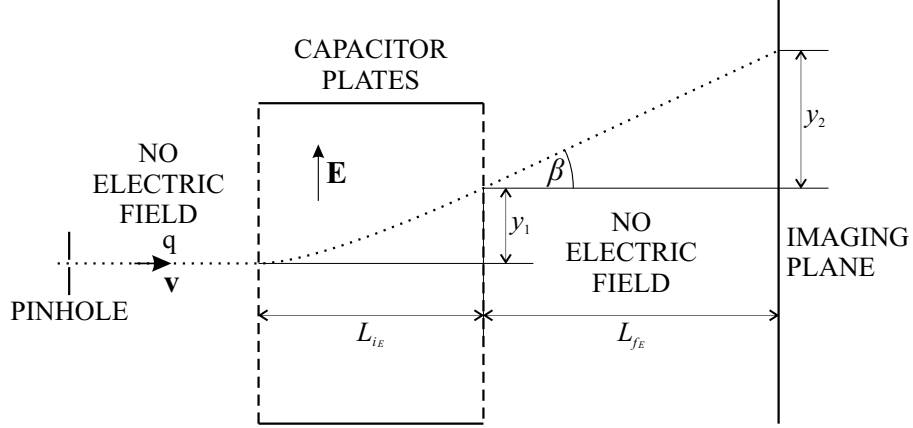


Figure B.2: Deviation of the charged particle by the electric field and its consequent detection on an imaging plane.

Assuming that the charged particle is entering in the electric field region with a velocity v perpendicular to each other, the positively charged particle feels a force in the direction of the electric field and starts to accelerate in this direction. We can assume the starting time t as zero. In this position the initial deflection position $y_1(0) = 0$ and the initial velocity in the y direction is $\dot{y}_1(0) = 0$. The part of the Lorentz equation for the electric field is:

$$m\ddot{y}_1 = qE \quad (\text{B.17})$$

where \ddot{y}_1 is an acceleration caused by the electric field, thus we obtain the momentum in the y direction as:

$$m\dot{y}_1 = qEt + C_1 \quad (\text{B.18})$$

The velocity \dot{y}_1 satisfies the initial condition at $t = 0$ and for this reason the constant $C_1 = 0$. Integrating once again the equation (B.18) we obtain:

$$my_1 = qEt^2 + C_2 \quad (\text{B.19})$$

Again from the initial condition for the y coordinate in time $t = 0$ the constant is $C_2 = 0$. The acceleration occurs only in the perpendicular to the particle's initial motion direction and does not influence the initial velocity v which we are interested in. The time spent in the electric field area is given only by the length l of the field and the particle's initial velocity:

$$t = \frac{l}{v} \quad (\text{B.20})$$

Thus the y_1 coordinate at the end of the region (i.e. $l = L_{i_E}$) will be:

$$y_1 = \frac{qE}{2m} \cdot \left(\frac{L_{i_E}}{v} \right)^2 \quad (\text{B.21})$$

The length of the field is changing from 0 up to L_{i_E} . In order to know the angle in which the particle is quitting the electric field we have to differentiate y with respect to l and from the geometry in Figure B.2 we will get:

$$\frac{dy_1}{dl} = \frac{qEl}{mv^2} \quad (\text{B.22})$$

Therefore the angle β of the quitting particle from the field region is given by:

$$\frac{dy_1}{dl} (L_{i_E}) = \tan \beta = \frac{qEL_{i_E}}{mv^2} \quad (\text{B.23})$$

In the field free region we can see from Figure B.2 that the y_2 coordinate is given by:

$$y_2 = L_{f_E} \tan \beta \quad (\text{B.24})$$

and from the equality of tangents in equation (B.23) and (B.24) we obtain:

$$y_2 = \frac{qEL_{i_E}L_{f_E}}{mv^2} \quad (\text{B.25})$$

We can put the results from equations (B.21) and (B.25) into equation (B.16), thus the length of the particle's transversal motion (and also the y coordinate on imaging plane) is:

$$y = \frac{qEL_{i_E}}{mv^2} \left(\frac{L_{i_E}}{2} + L_{f_E} \right) \quad (\text{B.26})$$

From the equality of the particle's velocity perpendicular to the present fields in equations (B.11) and (B.26) we will get the final parabola equation drawn on the imaging plane:

$$y = \frac{q}{m} \cdot \frac{EL_{i_E} \left(\frac{L_{i_E}}{2} + L_{f_E} \right)}{B^2 L_{i_B}^2 \left(\frac{L_{i_B}}{2} + L_{f_B} \right)^2} \cdot x^2 \quad (\text{B.27})$$

Appendix C

Physical Model of Developed Faraday Cup

The Faraday cup developed in Section 3.5 can be considered as a transmission line which is a distributed parameter network, where voltages and currents can vary in magnitude and phase over its length. Such a transmission line can be schematically represented as a two-wire line, since transmission lines (for TEM¹ wave propagation) always have at least two conductors. The short piece of line of length Δz can be modeled as a lumped-element circuit, as shown in Figure C.1, where R [Ω/m] is defined as a series resistance per unit length for both conductors, L [H/m] is a series inductance per unit length for both conductors, G [S/m] is a shunt conductance per unit length and C [F/m] is a shunt capacitance per unit length.

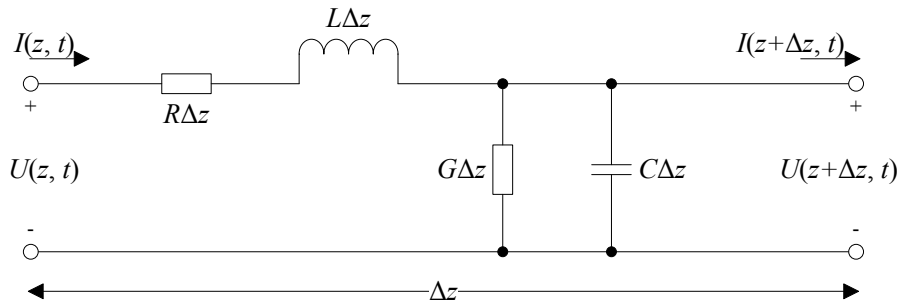


Figure C.1: Voltage and current definitions and lumped-element for an incremental length of transmission line [44, 45].

The series inductance L represents the total self-inductance of the two conductors, and the shunt capacitance C is due to the close proximity of the two conductors. The series resistance R represents the resistance due to the finite conductivity of the conductors, and the shunt conductance G is due to dielectric loss in the material between conductors. R and G , therefore, represent a loss. A finite length of transmission line can be viewed as a cascade of sections represented in Figure C.1. Kirchhoff's voltage and current law can be applied onto the circuit depicted in Figure C.1 which in a limit of $\Delta z \rightarrow 0$ leads to Telegrapher equations:

¹Transverse Electro-Magnetic mode in which neither electric nor magnetic field is present in the direction of propagation (i.e. electric and magnetic field is only perpendicular to the wave propagation direction).

$$-\frac{\partial U(z,t)}{\partial z} = RI(z,t) + L\frac{\partial I(z,t)}{\partial t} \quad (\text{C.1})$$

$$-\frac{\partial I(z,t)}{\partial z} = GU(z,t) + C\frac{\partial U(z,t)}{\partial t} \quad (\text{C.2})$$

Now we can do the derivative of equation (C.1) with respect to z and derivative of equation (C.2) with respect to t and put them together getting:

$$-\frac{\partial^2 U(z,t)}{\partial z^2} = -RGU(z,t) - (RC + LG)\frac{\partial U(z,t)}{\partial t} - LC\frac{\partial^2 U(z,t)}{\partial t^2} \quad (\text{C.3})$$

We can assume that our transmitting signal is in a form of $U(z) = A \exp(i\omega t)^2$. Solving fully the equation (C.3) the traveling wave is then in a form:

$$U(z,t) = U_0^+ e^{i(\omega t - kz)} + U_0^- e^{i(\omega t + kz)} \quad (\text{C.4})$$

Here U_0^+ represents the propagation in $+z$ direction, U_0^- represents the wave propagation in $-z$ direction, ω is defined as:

$$\omega = 2\pi f \quad (\text{C.5})$$

where f is a frequency of the signal (i.e. ω is a real value), and k is a complex propagation constant. Doing the same procedure also for current I instead of voltage U and putting equation (C.4) into equation (C.1) we get:

$$I(z,t) = I_0^+ e^{i(\omega t - kz)} + I_0^- e^{i(\omega t + kz)} = \frac{1}{\sqrt{\frac{R+i\omega L}{G+i\omega C}}} \left(U_0^+ e^{i(\omega t - kz)} - U_0^- e^{i(\omega t + kz)} \right) \quad (\text{C.6})$$

We can define the characteristic impedance as:

$$Z_0 = \frac{U_0^+}{I_0^+} = \frac{-U_0^-}{I_0^-} = \sqrt{\frac{R+i\omega L}{G+i\omega C}} \quad (\text{C.7})$$

For good conductors and high frequencies we can approximate the characteristics impedance as:

$$Z_0 \approx \sqrt{\frac{L}{C}} \quad (\text{C.8})$$

Putting the solution in equation (C.4) into an equation (C.3) we are able to derive a dispersion-like relation for the complex propagation constant:

$$k^2 = -RG - i\omega(RC + LG) + \omega^2 LC \implies k = -i\sqrt{G+i\omega C}\sqrt{R+i\omega L} \quad (\text{C.9})$$

The real part of the complex propagation constant then denotes the wave number and the imaginary part is the attenuation constant. We have chosen the negative solution of k in equation (C.9) for our further derivation of current³.

²We can assume our signal as a modulated wave consisting of a finite number of harmonic waves. This and other further approximations are valid in frequency domain greater than several 10 MHz.

³We have to note also that resistance R is in our case dependent on the field frequency and this has to be taken in to account in further derivations of other parameters.

From equation (C.9) we are able to calculate the wave number as a real part⁴ of the complex propagation constant:

$$k = \Re k + i\Im k \implies \Re k = \sqrt{\frac{\omega^2 LC - G\rho\sqrt{\omega} + \sqrt{\omega(G^2 + \omega^2 C^2)(\rho^2 + \omega L^2)}}{2}} \quad (\text{C.10})$$

Here the series resistance R is substituted by $\rho\sqrt{\omega}$ because in our case (coaxial Faraday cup and two wires coming from it into the BNC coaxial cable) the resistance is linearly dependent on the so-called surface resistivity R_S (see Table C) which depends on the skin depth δ ⁵ and thus the square root of ω [45]:

$$R_S = \frac{1}{\sigma\delta} = \sqrt{\frac{\omega\mu}{2\sigma}} \quad (\text{C.11})$$

The surface resistivity is the property of the material which is dependent only on its conductance, permeability and on the field frequency.

We can say that the Telegrapher equations give the solution of the electromagnetic wave propagating along the transmission line with its characteristic impedance. For such traveling wave we are able to calculate the phase velocity v_φ and group velocity v_g ⁶ of our system:

$$v_\varphi = \frac{\omega}{\Re k}, v_g = \frac{d\omega}{d(\Re k)} \quad (\text{C.12})$$

In our case the phase velocity can be (high frequencies) approximated according to equation (C.10) as $v_\varphi = 1/\sqrt{LC}$ ⁷.

The coaxial line can also support TE and TM waveguide modes in addition to a TEM mode. In practice, these modes are usually cutoff (evanescent), and so have only a reactive effect near discontinuities or sources, where they are excited. It is important in practice, however, to be aware of the cutoff frequency of the lowest order waveguide-type modes in order to avoid the propagation of these modes. Deleterious effects may otherwise occur due to the superposition of two or more propagating modes with different propagation constants. Avoiding the propagation of higher order modes sets an upper limit on the size of a coaxial cable: this ultimately limits the power handling capacity of a coaxial line. Thus the highest usable frequency, before higher order of TE and TM modes starts to propagate, is [45]:

$$f_c = \frac{1}{\pi\sqrt{\epsilon_r\mu_r}(a+b)} = \frac{c}{\pi\sqrt{\epsilon_r\mu_r}(a+b)} \quad (\text{C.13})$$

Where ϵ_r is relative permittivity and μ_r relative permeability of the dielectric placed between coaxial electrodes, c is the speed of light in vacuum, a is the inner and b the outer radius of the coaxial line. In practice, a 5% safety margin is usually recommended. Thus the highest frequency of our Faraday cup developed in section 3.5 is capable to

⁴Actually from equation (C.9) we will get four results for the real part of the wave number, here we have chosen the one which in our cases really gives the real positive value.

⁵Skin depth is a material constant telling us in which depth the original signal amplitude will decrease below $1/e$ of its original value.

⁶The group velocity needs to express ω as a function of k from equation (C.9). Here we must not forget the resistivity dependence on ω , this will give us six different expressions of ω from which we have to take the one, which is a real number and which has a derivative (with respect to k) giving a group velocity lower than the speed of light in vacuum.

⁷This is also the result for any kind of frequency in a lossless transmission line.

transmit frequencies up to 15.868 GHz (within 5% safety factor). Then it depends only on the coaxial guiding from the Faraday cup to oscilloscope and also it's sampling. The only problem of Teflon used as a dielectric material is that in the frequency range from 9.5 GHz to 10.2 GHz there is a non-negligible change in complex permittivity and permeability [41]. For other frequencies up to the cutoff one the permittivity and permeability remain constant or has negligible variations. In principle the rise time of our collector should not be higher than the period given as the inverse cutoff frequency. Theoretically, for such case, the rise time should not be greater than 60 ps, which allows our diagnostic system to detect very fast.

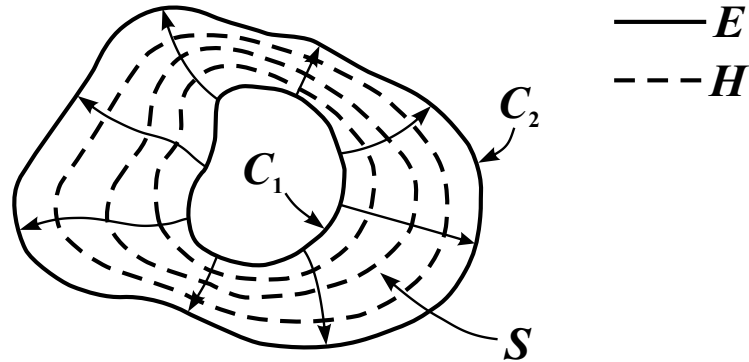


Figure C.2: Field lines on an arbitrary TEM transmission line [45].

When we consider a 1 m section of a uniform transmission line with fields E and H , as shown in Figure C.2, where S is the cross-sectional surface area of the line, the transmission line parameters (R, L, G, C) in terms of the electric and magnetic field can be derived from a time-averaged stored electric and magnetic energy with a boundary conditions C_1 and C_2 . The formulas of our ion collector system (a coaxial Faraday cup and two wires coming from them into the BNC cable) are reported in Table C.

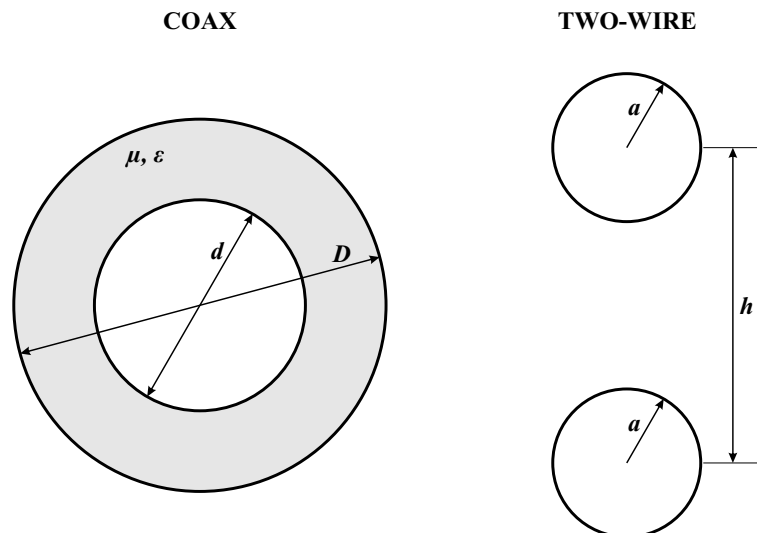


Figure C.3: Cross-section of a coaxial line and system of two-wires coming from the Faraday cup into a coaxial BNC cable.

The coaxial Faraday cup has a constant ratio of the inner and outer diameter. The detected signal is guided by a set of silver-coated⁸ copper wires. One wire comes from the inner electrode of the Faraday cup into the signal line of the BNC cable and the second wire comes from the outer electrode to the grounding line. The distance between wires is unfortunately not constant and the wires itself are slightly bent for flexibility reasons. In our further approach we will assume that the wires are perfect line segment with a constant distance between them⁹. The cross-section of the Faraday cup and wires situation is shown in Figure C.3. All these properties along with the material constants are reported in a Table C.

The charge collected by the ion collector is guided into a coaxial Faraday cup through the silver-coated copper wires and then by a BNC cable. All these three elements of the transmission line have different impedances. The impedance is defined by equation (C.7). When the transmission line changes at position $z = 0$ into a load impedance Z_L , we can write the equation (C.7) as:

$$Z_L = \frac{U(0)}{I(0)} = \frac{U_0^+ + U_0^-}{U_0^+ - U_0^-} Z_0 \quad (\text{C.14})$$

We can solve equation (C.14) for backward propagating solution and then rewrite this equation into the ratio between the wave propagating backward (U_0^- amplitude) and forward (U_0^+ amplitude) direction, the amplitude of the reflected voltage wave normalized to the amplitude of the incident wave is known as the voltage reflection coefficient R_U . The current ratio R_I is then derived from equation (C.6) and the result is:

$$\Gamma = R_U = \frac{U_0^-}{U_0^+} = \frac{Z_L - Z_0}{Z_L + Z_0} = -R_I \quad (\text{C.15})$$

The traveling wave solution from equation (C.4) and (C.6) can be written as:

$$U(z, t) = U_0^+ \left(e^{i(\omega t - kz)} + \Gamma e^{i(\omega t + kz)} \right), I(z, t) = \frac{U_0^+}{Z_0} \left(e^{i(\omega t - kz)} - \Gamma e^{i(\omega t + kz)} \right) \quad (\text{C.16})$$

From formulas in equation (C.17) we can see that the voltage and current on the line consist of a superposition of an incident and reflected wave, such waves are called standing waves. Only when $\Gamma = 0$ there is no reflected wave and Z_L must be equal to the characteristic impedance Z_0 , the total reflection occurs when $\Gamma = 1$, here is the voltage loop and current node, this is the free-ending with infinity load impedance. The signal transmission can be then considered from the time-averaged power flow along the line as [45]:

$$P_{ave} = \frac{1}{2} \Re \langle UI^* \rangle_t = \dots = \frac{|U_0^+|^2}{2Z_0} (1 - |\Gamma|^2) = \frac{|U_0^+|^2}{2Z_0} \cdot T \quad (\text{C.17})$$

Transmittance T of the averaged power is just equal to the original power flow minus the reflected power. For our case the detected charged particles cause the voltage and current signal, on one end the signal is coming further through two other different

⁸Here we assume that the main medium transferring current is silver but actually, in reality, it is just a very thin layer of silver coating and then the current is transferred through a specific skin depth of the copper wire inside the coating.

⁹This constant distance is assumed as the mean distance because the wires are attached to the Faraday cup with the same distance from each other and then they are attached to the BNC socket with a different distance.

impedances region and on the other end the signal wave is reflected completely. Finally, we would like to know the transmission of the particle signal from these three different regions. Here we will define the transmission and reflection coefficient from the Faraday cup to the two-wire system, and from the two-wire system into 50 Ω BNC cable:

$$\Gamma_{12} = \frac{Z_{TW} - Z_{FC}}{Z_{TW} + Z_{FC}}, T_{12} = 1 - |\Gamma_{12}|^2, \Gamma_{23} = \frac{Z_{50 \Omega} - Z_{TW}}{Z_{50 \Omega} + Z_{TW}}, T_{23} = 1 - |\Gamma_{23}|^2 \quad (\text{C.18})$$

Then we would like to calculate the time dispersion of our signal, thus we will calculate how many times the signal travels from the first reflection from the two-wire interface and from the full reflection from its free-ending. Once we will know how many times it travels the double distance of the Faraday cup's length (and the group velocity of the traveling signal) we will be able to calculate how long it lasts for the transmission of $1 - 1/e$ of the original collected power into the 50 Ω BNC cable and further to the oscilloscope (we will assume no reflections¹⁰ in the further system). Here we have to assume at least two reflections at the endings of the two-wire system (two reflections at both endings because after that the reflected power flow will decrease below $1/e$ of its original value). This means that, when the signal is transmitted from Faraday cup, every time it is then assumed to be partially transmitted into the BNC cable and partially reflected, back to the interface of the Faraday cup and to the two-wire system. Here we neglect the transmission as the reflection is high ($|\Gamma_{12}|^2 = 0.8955$, $|\Gamma_{23}|^2 = 0.5909$). The first several transmissions are reported in Table C.1.

Transmission from Faraday cup to two-wire system and further	Transmission from two-wire system after first reflection	Transmission from two-wire system after second reflection
$T_{12}T_{23}$		
$ \Gamma_{12} ^2 T_{12}T_{23}$	$T_{12} \Gamma_{23} ^2 \Gamma_{12} ^2 T_{23}$	
$ \Gamma_{12} ^4 T_{12}T_{23}$	$ \Gamma_{12} ^2 T_{12} \Gamma_{23} ^2 \Gamma_{12} ^2 T_{23}$	$T_{12} \Gamma_{23} ^4 \Gamma_{12} ^4 T_{23}$
$ \Gamma_{12} ^6 T_{12}T_{23}$	$ \Gamma_{12} ^4 T_{12} \Gamma_{23} ^2 \Gamma_{12} ^2 T_{23}$	$ \Gamma_{12} ^2 T_{12} \Gamma_{23} ^4 \Gamma_{12} ^4 T_{23}$
$ \Gamma_{12} ^8 T_{12}T_{23}$	$ \Gamma_{12} ^6 T_{12} \Gamma_{23} ^2 \Gamma_{12} ^2 T_{23}$	$ \Gamma_{12} ^4 T_{12} \Gamma_{23} ^4 \Gamma_{12} ^4 T_{23}$
\vdots	\vdots	\vdots

Table C.1: Table of the weighted transmission.

From Table C.1 we are able to derive the sums where we want to know the number of transmission inside the faraday cup where the transmitted power is greater than $1 - 1/e$:

$$T_{12}T_{23} \left(\sum_{i=0}^2 |\Gamma_{23}|^{2i} \sum_{j=0}^{n-i} |\Gamma_{12}|^{2(j+i)} \right) \geq 1 - \frac{1}{e} \quad (\text{C.19})$$

Now we are able to calculate the lowest n for which equation (C.19) will be valid and the result is $n = 12$. We can calculate the time dispersion τ from the known length of

¹⁰When the termination of 1 M Ω is applied on the oscilloscope, it then depends if the scope have the correct compensating series resistance to avoid any reflections of the signal. Most of the today's fast oscilloscopes should have it.

the Faraday cup ($d_{FC} = 14$ mm, n reflections) and two-wire system ($d_{TW} = 25$ mm, j reflections) as upper limit:

$$\tau = \frac{2 \cdot n \cdot d_{FC}}{v_{gFC}} + \frac{2 \cdot j \cdot d_{TW}}{v_{gTW}} \quad (\text{C.20})$$

According to equation (C.19) and results from Table C the time dispersion in which $1 - 1/e$ of the original power will come in the oscilloscope is $\tau = 1.95$ ns.

Summary of all assumptions used for theoretical description of our ion collector system

1. The developed Faraday cup is emission-less in terms of secondary emission effect due to the particle impact and also electro-magnetic emission due to current flow.
2. The Ion collector system is a transmission line for TEM waves.
3. Frequencies higher than the one for propagating of TE and TM waves defines the cut-off frequency for our Faraday cup.
4. The low frequency limit is 10 MHz in order to do the approximations for impedance characteristics.
5. We do not assume the frequency interval $< 9.5 \text{ GHz}, 10.2 \text{ GHz} >$ where Teflon's complex permittivity and permeability have a non-negligible behavior.
6. The detected signal is a modulated wave consisting of a finite number of harmonic waves.
7. The resistance R depends on the signal's frequency.
8. The real part of the complex propagation constant is real positive number.
9. Solution of equation (C.9) for the field frequency is a real positive number giving a group velocity lower than the speed of light.
10. The main medium transferring the current in silver-coated copper wires in the two-wire system is silver.
11. The wires of the two-wire system are assumed as perfect line segment with a constant (mean in reality) distance between them.
12. The imaginary parts of the Teflon permittivity and permeability are negligible.
13. The signal transmission can be then considered from the time-averaged power flow along the transmission line.
14. We assume the reflections of the signal only on the interfaces between the Faraday cup and the two-wire system, and the two-wire system and the 50Ω BNC cable, no further reflection is assumed. The total reflection occurs on the free-ending of the Faraday cup. We neglect the soldered junctions.
15. Two reflections are taken into account in the two-wire system itself, in such case the reflected power flow decreases below $1/e$, and neglect the transmission back into Faraday cup.
16. The time dispersion for the detected signal, which is propagating with group velocity, is calculated for the case where the transmitted power flow is higher than $1 - 1/e$.

	Physical Property (Constant)	Formula	Numerical expression
Physical and Material Constants	Speed of Light	c	299792458 m/s
	Vacuum Permeability	μ_0	$4\pi \times 10^{-7}$ H/m
	Vacuum Permittivity	$\epsilon_0 = \frac{1}{\mu_0 c^2}$	8.854×10^{-12} F/m
	Teflon's Relative Permeability	$\mu_r = \mu_r' - i\mu_r''$	$1.0 - i0.0$
	Teflon's Relative Permittivity	$\epsilon_r = \epsilon_r' - i\epsilon_r''$	$2.04 - i0.00$
	Copper Conductivity	σ_{Cu}	5.813×10^7 S/m
	Copper Skin Depth	$\delta_{Cu} = \sqrt{\frac{2}{\omega\mu\sigma_{Cu}}}$	$165.4 \times 10^{-3}/\sqrt{\omega}$ m
	Copper Surface Resistivity	$R_{SCu} = \frac{1}{\sigma_{Cu}\delta_{Cu}}$	$1.04 \times 10^{-7}\sqrt{\omega}$ Ω
	Silver Conductivity	σ_{Ag}	6.173×10^7 S/m
	Silver Skin Depth	$\delta_{Ag} = \sqrt{\frac{2}{\omega\mu\sigma_{Ag}}}$	$160.6 \times 10^{-3}/\sqrt{\omega}$ m
Silver Surface Resistivity	$R_{SAg} = \frac{1}{\sigma_{Ag}\delta_{Ag}}$	$1.01 \times 10^{-8}\sqrt{\omega}$ Ω	
Coaxial Faraday Cup	Inner Electrode Diameter	d	3.50 mm
	Outer Electrode Diameter	D	4.50 mm
	95% Cutoff Frequency	$f_c = \frac{2c}{\pi\sqrt{\epsilon_r\mu_r}(D+d)}$	15.87 GHz
	Inductance	$L_{FC} = \frac{\mu}{2\pi} \ln\left(\frac{D}{d}\right)$	5.03×10^{-8} H/m
	Capacitance	$\frac{2\pi\epsilon_0\epsilon_r'}{\ln\left(\frac{D}{d}\right)}$	4.52×10^{-10} F/m
	Resistance	$R_{FC} = \frac{R_{SCu}}{\pi} \left(\frac{1}{d} + \frac{1}{D}\right)$	$1.68 \times 10^{-5}\sqrt{\omega}$ Ω /m
	Conductance	$\frac{2\pi\omega\epsilon_0\epsilon_r''}{\ln\left(\frac{D}{d}\right)}$	0 S/m
	Impedance	$Z_{FC} \approx \sqrt{\frac{L_{FC}}{C_{FC}}}$	10.55
	Phase velocity	$v_{\varphi_{FC}} = 1/\sqrt{L_{FC}C_{FC}}$	209896704 m/s
Group velocity	$v_{g_{FC}}$	208591500 m/s	
Two-Wire	Wire Radius	a	0.161 mm
	Wires Distance	h_{TW}	3.9 mm
	Inductance	$L_{TW} = \frac{\mu}{\pi} \cosh^{-1}\left(\frac{h_{TW}}{2a}\right)$	1.28×10^{-6} H/m
	Capacitance	$C_{TW} = \frac{\pi\epsilon_0\epsilon_r'}{\cosh^{-1}\left(\frac{h_{TW}}{2a}\right)}$	8.72×10^{-12} F/m
	Resistance	$R_{TW} = \frac{R_{SAg}}{\pi a}$	$2.00 \times 10^{-4}\sqrt{\omega}$ Ω /m
	Conductance	$G_{TW} = \frac{\pi\omega\epsilon_0\epsilon_r''}{\cosh^{-1}\left(\frac{h_{TW}}{2a}\right)}$	0 S/m
	Impedance	$Z_{FC} \approx \sqrt{\frac{L_{FC}}{C_{FC}}}$	382.38 Ω
	Phase velocity	$v_{\varphi_{FC}} = 1/\sqrt{L_{FC}C_{FC}}$	299792458 m/s
	Group velocity	$v_{g_{TW}}$	298565000 m/s

Table C.2: Table of physical constants, Faraday cup and Two-wire properties and their numerical expressions (dependent on the signal frequency valid from 10 MHz up to the cutoff frequency except the interval < 9.5 GHz, 10.2 GHz $>$ where a non-negligible behavior of Teflon's relative permittivity and permeability is present, and in which these values are not constant [41]) for the Telegrapher equations [45]. The group velocity formula is very complicated to be presented here, it was processed and calculated by mathematical software and its general expression covers full 23 pages of A4 format.

Appendix D

Derivation of Energy Distribution Measured by Faraday Cup and SiC Diagnostics

In order to know the number of particles or the total charge detected by the detector. In case of an ion collector we neglect any secondary emission effects. We can assume that any collected charge becomes from particles impinging the detector and the deionization occurs only in the detector.

Ion collector

When a grid is applied in front of collector we should not neglect the transmission of such grid.

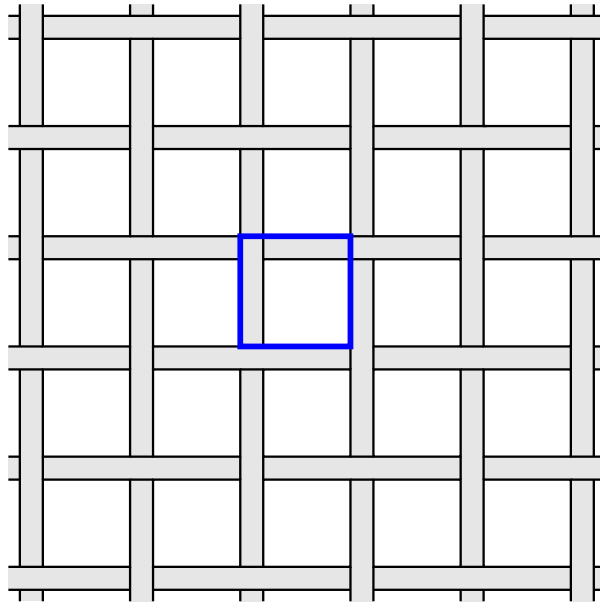


Figure D.1: Scheme of grid in front of the ion collector.

We assume that each hole of the grid has a square shape with an area of a^2 and the wire diameter is b (grid is not deformed). The grid transmission can be then calculated from the ratio of the hole area and area of the hole and wire on the left side and top (this

situation is depicted by blue square in Figure D.1, by this we can cover the whole 2D plane) as:

$$T = \left(\frac{a}{a+b} \right)^2 \quad (\text{D.1})$$

In this configuration we are able to cover the whole detecting area. We also assume that the grid is perfectly conductive and not transparent for particles with any energies. The real charge Q coming on the detector in a given time t is then recalculated from the detected charge \tilde{Q} as:

$$\tilde{Q} = TQ \quad (\text{D.2})$$

For such case we can write equation (4.1) from which can be seen that electrons will have a negative and ions positive contribution to the detected charge. In case of quasi-neutral plasma we would detect a zero signal. The current I then corresponds to the detected charge ΔQ over time Δt as:

$$I = \frac{\Delta \tilde{Q}}{\Delta t} = T \frac{\Delta Q}{\Delta t} \quad (\text{D.3})$$

where the measured current corresponds to the voltage on the oscilloscope from equation (4.2). Equation (D.3) can be then divided by a relation $\Delta \mathcal{E}/\Delta t$ resulting in:

$$\frac{\frac{\Delta Q}{\Delta t}}{\frac{\Delta \mathcal{E}}{\Delta t}} = \frac{1}{T} \frac{U}{R \frac{\Delta \mathcal{E}}{\Delta t}} \quad (\text{D.4})$$

where $\Delta \mathcal{E}$ denotes the increment of kinetic energy per time unit Δt . On the left side of equation (D.4) we can cut Δt as it is the finite time over which the charge flows through. Δt will then remain only on the right hand side of equation (D.4) which in the limit of $\Delta t \rightarrow 0$ (\mathcal{E} depends explicitly on time as shown in equation (3.2) and so the energy increment also depends on time) gives us the wanted distribution:

$$\frac{dQ}{d\mathcal{E}} = \frac{1}{T} \frac{U}{R \frac{d\mathcal{E}}{dt}} \quad (\text{D.5})$$

Using equation (3.2) and (3.10) we can then derive an equation:

$$\frac{dQ}{d\mathcal{E}} = -\frac{1}{T} \frac{U(t)t^3}{RmL^2} \quad (\text{D.6})$$

in SI units. Next assumption is that whole distribution is present in the whole ion beam and thus we can recalculate this spectrum from the detector solid angle Ω_{DETECTOR} to the whole ion beam solid angle Ω_{BEAM} just multiplying the equation (D.6) by the factor:

$$\frac{\Omega_{\text{BEAM}}}{\Omega_{\text{DETECTOR}}} = \frac{S_{\text{BEAM}}}{S_{\text{DETECTOR}}} = \frac{\tilde{S}_{\text{BEAM}} \left(\frac{L_{\text{DETECTOR}}}{L_{\text{BEAM}}} \right)^2}{S_{\text{DETECTOR}}} \quad (\text{D.7})$$

where S_{DETECTOR} is the detector's detecting area (in case of applied collimator the area defined by the collimator's hole if smaller than detector) placed in distance L_{DETECTOR} , S_{BEAM} is the ion beam area at the detector plane and \tilde{S}_{BEAM} is the ion beam area measured in distance of L_{BEAM} .

From the measured parameters on the oscilloscope (voltage and time) we can write the energy distribution of the charge as:

$$\frac{dQ [\text{C}]}{d\mathcal{E} [\text{eV}]} = -\frac{1}{T} \frac{U(t) [\text{V}] t^3 [\text{s}] |e|}{R [\Omega] m [\text{kg}] L^2 [\text{m}]} \frac{\Omega_{\text{BEAM}} [\text{sr}]}{\Omega_{\text{DETECTOR}} [\text{sr}]} \quad (\text{D.8})$$

where $|e|$ is the value of the elementary charge and according to various types of particles arriving to the detector, m is the atomic mass unit, U is measured voltage, R is the total resistivity of the detector circuits (including termination on the oscilloscope), t corresponds to TOF from equation (3.9) and L is the detector distance. Energy spectrum in Figure 4.5 is recalculated from equation (D.8) taken in absolute value. Integrating the area below curves gives us a total charge of particles in plotted energy ranges in the whole ion beam under the assumption mentioned above (measured distribution by the detector is uniform in the whole solid angle of the ion beam).

SiC detector

For the case of the SiC detector the situation is different. The SiC response is not dependent on the collected charge of the particles but on the particles' energy when coming through an active volume. The measured charge by the detector was measured through calibration and the result is reported in equation (4.5):

$$Q = \frac{eN\mathcal{E}}{\mathcal{E}_G} \quad (\text{D.9})$$

where \mathcal{E} denotes here the kinetic energy. We can do the same procedure that current response (measured voltage on the scope, respectively) is given by equation (D.3) and no opaque grid is applied. The detected current response I in a given time t (this time corresponds to TOF) is proportional to a number of particles N hitting the detector with a kinetic energy \mathcal{E} . The kinetic energy depends on time (from TOF), the number of accelerated particles does not depend on time generally but the number of particles hitting the detector at some distance from the target varies because of their different energy (through different TOF), that's why the number of particles detected at a given time t depends on the time. We can define that $\Delta N = N_2 - N_1$, $\Delta \mathcal{E} = \mathcal{E}_2 - \mathcal{E}_1$ and calculate:

$$\frac{\Delta(N\mathcal{E})}{\Delta t} = \frac{N_2\mathcal{E}_2 - N_1\mathcal{E}_1}{t_2 - t_1} = \frac{\mathcal{E}_1\Delta N + N_2\Delta\mathcal{E}}{\Delta t} \quad (\text{D.10})$$

where $N_1 = N(t_1)$, $N_2 = N(t_2)$, $\mathcal{E}_1 = \mathcal{E}(t_1)$, $\mathcal{E}_2 = \mathcal{E}(t_2)$, and t_1 and t_2 are close to each other. It is then possible to write:

$$I(t) = \frac{\Delta Q}{\Delta t} = \frac{e}{\mathcal{E}_G} \left(N_2 \frac{\Delta \mathcal{E}}{\Delta t} + \mathcal{E}_1 \frac{\Delta N}{\Delta t} \right) \quad (\text{D.11})$$

We will divide equation (D.11) by $\mathcal{E}_1\Delta\mathcal{E}/\Delta t$, along with equation (4.2) it will result in:

$$\frac{U(t)}{R\mathcal{E}_1 \frac{\Delta \mathcal{E}}{\Delta t}} = \frac{e}{\mathcal{E}_G} \left(\frac{N_2}{\mathcal{E}_1} + \frac{\frac{\Delta N}{\Delta t}}{\frac{\Delta \mathcal{E}}{\Delta t}} \right) \quad (\text{D.12})$$

We are able to cut Δt on the right side of equation (D.12) and then do the limit of equation (D.12) where $t_1 \rightarrow t_2$ and we can label t_2 as $t_2 = t$ (getting also $N_2 = N(t)$ and $\lim_{t_1 \rightarrow t} \mathcal{E}_1 = \mathcal{E}(t)$) and we get:

$$\frac{U(t)}{R\mathcal{E} \frac{d\mathcal{E}}{dt}} = \frac{e}{\mathcal{E}_G} \left(\frac{N}{\mathcal{E}} + \frac{dN}{d\mathcal{E}} \right) \quad (\text{D.13})$$

From equation (D.9) we determine what is N at given time t as:

$$N(t) = \frac{\mathcal{E}_G}{e\mathcal{E}}Q(t) = \frac{\mathcal{E}_G}{e\mathcal{E}} \int I(t)dt = \frac{\mathcal{E}_G}{e\mathcal{E}} \int \frac{U(t)}{R}dt \approx \frac{\mathcal{E}_GU(t)}{eR\mathcal{E}}\delta t \quad (\text{D.14})$$

Where here $Q(t)$ is the charge detected by the oscilloscope which is equal to current coming through the measuring device by a time interval δt . This time interval is given by the analog-to-digital converter's properties inside the oscilloscope and here we approximate this time interval as the smallest time step of the oscilloscope. From equation (D.13) and (D.14) we get energy distribution as:

$$\frac{dN}{d\mathcal{E}} = \frac{\mathcal{E}_GU(t)}{eR\mathcal{E}} \left(\frac{1}{\frac{d\mathcal{E}}{dt}} - \frac{\delta t}{\mathcal{E}} \right) \quad (\text{D.15})$$

Then using equation (3.2) and (3.10) we get the energy distribution on detector in SI units:

$$\frac{dN}{d\mathcal{E}} = \frac{\mathcal{E}_GU(t)t^4}{eRm^2L^4} (-2t - 4\delta t) \quad (\text{D.16})$$

We can then recalculate energy distribution from equation (D.16) (again assuming that measured distribution by the detector is uniform in the whole solid angle of the ion beam) to the solid angle of the ion beam for the measured parameters on the oscilloscope (voltage and time) as:

$$\frac{dN}{d\mathcal{E} [\text{eV}]} = \frac{\mathcal{E}_G [\text{eV}] |e|}{1 [\text{C}] R [\Omega] m^2 [\text{kg}] L^4 [\text{m}]} U(t) [\text{V}] t^4 [\text{s}] \left(-\frac{1}{2}t [\text{s}] - \delta t [\text{s}] \right) \quad (\text{D.17})$$

where \mathcal{E}_G is the minimal energy needed to create the electron-hole pair inside the detector active zone, $|e|$ is the value of the elementary charge, and since we expect to measure only protons, m is the proton mass, U is measured voltage, R is the total resistivity of the detector circuits (including termination on the oscilloscope), t corresponds to TOF from equation (3.9), δt is the time interval of the oscilloscope and L is the detector distance. Using equation (3.2) and (3.10) again we get:

$$\frac{dN}{d\mathcal{E} [\text{eV}]} = \frac{\mathcal{E}_G [\text{eV}] U(t) [\text{V}]}{e [\text{C}] R [\Omega] \mathcal{E}^2 [\text{eV}]} \left(-\frac{1}{2}t [\text{s}] - \delta t [\text{s}] \right) \frac{\Omega_{\text{BEAM}} [\text{sr}]}{\Omega_{\text{DETECTOR}} [\text{sr}]} \quad (\text{D.18})$$

which is exactly the equation (4.6). The energy spectrum was obtained from plots in Figures 4.6 and 4.8 by recalculated for the proton signal only by equation (D.17) resulting in spectra in Figures 4.7 and 4.9. Integrating the area below curves gives us a total number of particles in plotted energy ranges in the whole ion beam.

Bibliography

- [1] T. Tajima & J. M. Dawson, *Laser electron accelerator*, Physical Review Letters **43**, pp. 267–270 (1979).
- [2] Michael D. Perry & Gerard A. Mourou, *Terawatt to Petawatt Subpicosecond Lasers*, Science **264**, pp. 917–924 (May 1994).
- [3] Gerard A. Mourou, *Optics in the relativistic regime*, Reviews of Modern Physics **78**, No. 2, pp. 309–371 (April-June 2006).
- [4] T. V Liseykina, M. Borghesi, A. Macchi, S. Tuveri, *Radiation pressure acceleration by ultraintense laser pulses*, Plasma Physics and Controlled Fusion **50**, No. 12, 124033 (December 2008).
- [5] G. Z. Sun, E. Ott, Y. C. Lee, P. Guzdar, *Self-focusing of short intense pulses in plasmas*, Physics of Fluids **30**, No. 2, pp. 526–532 (February 1987).
- [6] P. Kulhnek, *Teorie Plazmatu*, available on-line at: <http://www.aldebaran.cz/studium/fpla.pdf>
- [7] Y. Sentoku, T. E. Cowan, A. Kemp, and H. Ruhl, *High energy proton acceleration in interaction of short laser pulse with dense plasma target*, Physics of Plasmas **10**, No. 5, pp. 2009–2015 (May 2003).
- [8] G. V. Stupakov, *Ponderomotive Laser Acceleration and Focusing in Vacuum for Generation of Attosecond Electron Bunches*, Physical Review Letters **86**, No. 23, pp. 5274–5277 (June 2001).
- [9] S. C. Wilks, W. L. Kruer, M. Tabak, A. B. Langdon, *Absorption of Ultra-Intense Laser Pulses*, Physical Review Letters **69**, No. 9, pp. 1383–1386 (August 1992).
- [10] M. C. Kaluza, *Characterisation of Laser-Accelerated Proton Beams*, Dissertation, Max-Planck-Institut für Quantenoptik, Technischen Universität München, München (2004), available on-line at: ftp://ftp.mpe.mpg.de/pub/publication/kaluza_mpq-report_v02.pdf
- [11] S. Atzeni, J. Meyer-Ter-Vehn, *The physics of inertial fusion*, Clarendon Press, Oxford, pp. 371–389 (2004).
- [12] P. Mulser, *Resonance absorption and ponderomotive action*, Handbook of Plasma Physics 3: Physics of Laser Plasma, North-Holland, Amsterdam, pp. 435–482 (1991).
- [13] H. J. Kull, *Linear-mode conversion in laser plasmas*, Physics of Fluids **26**, pp. 1881–1887 (July 1983).

- [14] S. C. Wilks, A. B. Langdon, T. E. Cowan, M. Roth, M. Singh, S. Hatchett, M. H. Key, D. Pennington, A. Mackinnon, and R. A. Snavely, *Energetic proton generation in ultra-intense laser-solid interactions*, *Physics of Plasmas* **8**, p. 542 (2001).
- [15] R. A. Snavely, M. H. Key, S. P. Hatchett, T. E. Cowan, M. Roth, T. W. Phillips, M. A. Stoyer, E. A. Henry, T. C. Sangster, M. S. Singh, S. C. Wilks, A. J. Mackinnon, A. Offenberger, D. M. Penning, K. Yasuike, A. B. Langdon, B. F. Lasinski, J. Johnson, M. D. Perry, and E. M. Campbell, *Intense High-Energy Proton Beams from Petawatt-Laser Irradiation of Solids*, *Physical Review Letters* **85**, p. 2945 (2000).
- [16] B. M. Hegelich, *Acceleration of heavy Ions to MeV/nucleon Energies by Ultrahigh-Intensity Lasers*, Dissertation, Ludwig-Maximilians Universität, München (2002), available on-line at: http://www.ha.physik.uni-muenchen.de/publications/diss/hegelich_manuel.pdf
- [17] P. Mora, *Plasma Expansion into a Vacuum*, *Physical Review Letters* **90**, No. 18, 185002 (May 2003).
- [18] M. Kaluza, J. Schreiber, M. I. K. Santala, G. D. Tsakiris, K. Eidmann, J. Meyer-ter-Vehn, K. J. Witte, *Influence of the Laser Prepulse on Proton Acceleration in Thin-Foil Experiments*, *Physical Review Letters* **93**, No. 4, 045003 (July 2004).
- [19] A. J. Mackinnon, M. Borghesi, S. Hatchett, M. H. Key, P. K. Patel, H. Campbell, A. Schiavi, R. Snavely, S. C. Wilks, O. Willi, *Effect of Plasma Scale Length on Multi-MeV Proton Production by Intense Laser Pulses*, *Physical Review Letters* **86**, No. 9, pp. 1769–1772 (February 2011).
- [20] http://www.rp-photonics.com/optical_intensity.html
- [21] K. Jungwirth, A. Cejnarova, L. Juha, B. Kralikova, J. Krasa, E. Krousky, P. Krupickova, L. Laska, K. Masek, T. Mocek, M. Pfeifer, A. Präg, O. Renner, K. Rohlena, B. Rus, J. Skala, P. Straka, and J. Ullschmied, *The Prague Asterix Laser System*, *Physics of Plasmas* **8**, No. 5, pp. 2495-2501 (May 2001).
- [22] <http://www.pals.cas.cz/laser/output-parameters/>
- [23] W. Koechner, *Solid-State Laser Engineering*, Springer, pp. 88–91 (2006).
- [24] http://www.rp-photonics.com/pockels_cells.html
- [25] http://www.rp-photonics.com/spectral_interferometry.html
- [26] T. M. Jeong, Il W. Choi, N. Hafz, J. H. Sung, S. Ku Lee, Do-Kyeong Ko, and J. Lee, *Wavefront Correction and Customization of Focal Spot of 100 TW Ti:Sapphire Laser System*, *Japanese Journal of Applied Physics* **46**, No. 12, pp. 7724-7730 (2007).
- [27] V. P. Yanovsky, M. D. Perry, C. G. Brown, M. D. Feit, A. Rubenchik, *Plasma Mirrors for Short Pulse Lasers*, *Ultrafast Optics*, preprint (June 1997).
- [28] I. J. Kim, I. W. Choi, S. K. Lee, K. A. Janulewicz, J. H. Sung, T. J. Yu, H. T. Kim, H. Yun, T. M. Jeong, J. Lee, *Spatio-temporal characterization of double plasma mirror for ultrahigh contrast and stable laser pulse*, *Applied Physics B Lasers and Optics* **104**, No. 1, pp. 81–86 (2011).
- [29] <http://www.gsi.de/forschung/pp/phelix/index.html>

- [30] E. Woryna, P. Parys, J. Wołowski, W. Mróz, *Corpuscular diagnostics and processing methods applied in investigations of laser-produced plasma as a source of highly ionized ions*, Laser and Particle Beams **14**, No. 3, pp. 293–321 (1996).
- [31] I. W. Choi, C. M. Kim, J. H. Sung, T. J. Yu, S. K. Lee *et al.*, *Ion spectrometer composed of time-of-flight and Thomson parabola spectrometers for simultaneous characterization of laser-driven ions*, Review of Scientific Instruments **80**, 053302 (2009).
- [32] M. J. Rhee, *Compact Thomson spectrometer*, Review of Scientific Instruments **55**, No. 8, pp. 1229–1234 (August 1984).
- [33] A. Szydłowski, J. Badziak, P. Parys, J. Wołowski, E. Woryna, K. Jungwirth, B. Kralikova, J. Krasa, L. Laska, M. Pfeifer, K. Rohlena, J. Skala, J. Ullschmied, F. D. Boody, S. Gammino, L. Torrisci, *Measurements of energetic ions emitted from laser produced plasma by means of solid state nuclear track detectors of the PM-355 type*, Plasma Physics and Controlled Fusion **45**, pp. 1417–1422 (2003)
- [34] <http://www.bo.infn.it/slim/NTD.htm>
- [35] G. Bertuccio, *Silicon Carbide Radiation Micro-Detectors for Harsh Environments*, SPIE Defence, Security and Sensing Symposium, Conference on Micro- and Nanotechnology Sensors, Systems, and Applications II, Orlando World Center Marriott Resort and Convention Center, Orlando, FL United States (5–9 April 2010).
- [36] D. Margarone, J. Krasa, L. Giuffrida, A. Picciotto, L. Torrisci, T. Nowak, P. Musumeci, A. Velyhan, J. Prokupek, L. Laska, T. Mocek, J. Ullschmied, and B. Rus, *Full characterization of laser-accelerated ion beams using Faraday cup, silicon carbide, and single-crystal diamond detectors*, Journal of Applied Physics **109**, 103302 (2011).
- [37] D. Kucerovsky, Z. Kucerovsky, *Analysis of the dynamic Faraday cup*, Journal of Physics D: Applied Physics **36**, pp. 2407–2416 (2003).
- [38] <http://www.bergoz.com/products/ICT/ICT.html>
- [39] M. S. Zucker, J. W. Bittner, *A Faraday Cup with High Frequency Response for a 200 MeV LINAC Proton Beam*, Conference: 1991 Institute of Electrical and Electronics Engineers (IEEE) particle accelerator conference (PAC), San Francisco, CA USA (6–9 May 1991).
- [40] Khoo, Teng Jian, *Photocathodes and a Faraday Cup for the AWA*, August 7 (2008), available online at: http://www.illinoisacceleratorinstitute.org/2008%20Program/student_papers/khoo_teng_jian.pdf.pdf
- [41] A. L. de Paula, M. C. Rezende, J. J. Barroso, *Experimental measurements and numerical simulation of permittivity and permeability of Teflon in X band*, Journal of Aerospace Technology and Management **3**, No. 1, pp. 59–64 (January–April 2011).
- [42] D. Margarone, J. Krasa, L. Giuffrida, A. Picciotto, L. Torrisci, T. Nowak, P. Musumeci, A. Velyhan, J. Prokupek, L. Laska, T. Mocek, J. Ullschmied, B. Rus, *Full characterization of laser-accelerated ion beams using Faraday cup, silicon carbide, and single-crystal diamond detectors*, Journal of Applied Physics **109**, 103302 (2011).

- [43] O. Klimo, J. Psikal, J. Limpouch, J. Proška, F. Novotny, T. Ceccotti, V. Floquet, S. Kawata, *Short pulse laser interaction with micro-structured targets: simulations of laser absorption and ion acceleration*, New Journal of Physics **13**, 053028 (May 2011).
- [44] J. Tolar, *Vlnění, optika a atomová fyzika*, pp. 56–60, available online at: <http://www.fjfi.cvut.cz/files/k402/files/skripta/voaf/VOAF2008.pdf>
- [45] David M. Pozar, *Microwave Engineering*, Second Edition, University of Massachusetts at Amherst (1998).

Published Papers

Peer reviewed journals

1. D. Margarone, J. Krasa, L. Laska, A. Velyhan, T. Mocek, L. Torrissi, L. Andò, S. Gammino, J. Prokupek, E. Krousky, M. Pfeifer, J. Ullshmiel, B. Rus, *Preliminary studies on fast particles' diagnostics for the future fs-laser facility at PALS*, Radiation Effects and Defects in Solids: Incorporating Plasma Sci. & Plasma Tech. **165**, pp. 419–428 (2010).
2. D. Margarone, J. Krasa, L. Laska, A. Velyhan, T. Mocek, J. Prokupek, E. Krousky, M. Pfeifer, S. Gammino, L. Torrissi, J. Ullschmiel, B. Rus, *Measurements of the Highest Acceleration Gradient for Ions Produced with a Long Laser Pulse*, Review of Scientific Instruments **81**, No. 2, 02A506 (2010).
3. D. Margarone, J. Krasa, A. Picciotto, J. Prokupek, *Real-time diagnostics of fast light ion beams accelerated by a sub-nanosecond laser*, Nukleonika **56**, pp. 137–141 (2011).
4. D. Margarone, J. Krása, L. Giuffrida, A. Picciotto, L. Torrissi, T. Nowak, P. Musumeci, A. Velyhan, J. Prokupek, L. Láska, T. Mocek, J. Ullschmiel, B. Rus, *Full Characterization of Laser-accelerated Ion Beams using Faraday Cup, Silicon Carbide and Single-crystal Diamond Detectors*, Journal of Applied Physics **109**, No. 2, 103302 (2011).
5. D. Margarone, J. Krasa, A. Picciotto, L. Torrissi, L. Laska, A. Velyhan, J. Prokupek, L. Ryc, P. Parys, J. Ullschmiel, B. Rus, *High current, high energy proton beams accelerated by a sub-nanosecond laser*, Nuclear Instruments and Methods in Physics Research A **653**, No. 1, pp. 159–163 (2011).
6. D. Margarone, J. Krasa, J. Prokupek, A. Velyhan, L. Torrissi, A. Picciotto, L. Giuffrida, S. Gammino, P. Cirrone, M. Cutroneo, F. Romano, E. Serra, A. Mangione, M. Rosinski, P. Parys, L. Ryc, J. Limpouch, L. Laska, K. Jungwirth, J. Ullschmiel, T. Mocek, G. Korn, B. Rus, *New methods for high current fast ion beam production by laser-driven acceleration*, Review of Scientific Instruments (accepted).

Conference proceedings

1. J. Nejd, M. Kozlova, M. Sawicka, D. Margarone, M. Krus, J. Prokupek, B. Rus, D. Batani, L. Antonelli, A. Patria, O. Ciricosta, C. Cecchetti, P. Koester, L. Labate, A. Giulietti, L. A. Gizzi, A. Moretti, M. Richetta, G. Schurtz, X. Ribeyre, M. Lafon, C. Spindloe, T. O'Dell, *Investigation of laser plasmas relevant to shock ignition at PALS*, Proceedings of SPIE Volume: **8080**, Article Number: 80802B, doi: 10.1117/12.892321, 2011
2. B. Rus, F. Batysta, J. Cap, M. Divoky, M. Fibrich, M. Griffiths, R. Haley, T. Havlicek, M. Hlavac, J. Hrebicek, P. Homer, P. Hribek, J. Jand'ourek, L. Juha, G. Korn, P. Korous, M. Koselja, M. Kozlova, D. Kramer, M. Krus, J.C. Lagron, J. Limpouch, L. MacFarlane, M. Maly, D. Margarone, P. Matlas, L. Mindl, J. Moravec, T. Mocek, J. Nejd, J. Novak, V. Olsovcova, M. Palatka, J.P. Perin, M. Peslo, J. Polan, J. Prokupek, J. Ridky, K. Rohlena, V. Ruzicka, M. Sawicka, L. Scholzova, D. Snopek, P. Strkula, L. Sveda, *Outline of the ELI-Beamlines facility*, Proceedings of SPIE Volume: **8080**, Article Number: 808010 doi: 10.1117/12.890392, 2011